Automatic segmentation of the cortical surface in neonatal brain MRI

Carlos Tor Díez

UNIVERSITE BRETAGNE LOIRE / MATHSTIC

IMT Atlantique
Bretagne-Pays de la Loire
École Mines-Télécom

THESE DE DOCTORAT DE

L'ÉCOLE NATIONALE SUPERIEURE MINES-TELECOM ATLANTIQUE
BRETAGNE PAYS DE LA LOIRE - IMT ATLANTIQUE
COMUE UNIVERSITE BRETAGNE LOIRE

ECOLE DOCTORALE N° 601
Mathématiques et Sciences et Technologies de l'Information et de la Communication
Spécialité : *Signal, Image, Vision*

Par
Carlos TOR DÍEZ

Segmentation automatique de la surface corticale dans des IRM cérébrales de nouveau-nés

Thèse présentée et soutenue à Brest, le 23/09/2019
Unité de recherche : LaTIM INSERM U1101
Thèse N° : 2019IMTA0152

Rapporteurs avant soutenance :

Miguel Angel GONZÁLEZ BALLESTER	Professeur, Universitat Pompeu Fabra
Grégoire MALANDAIN	Directeur de recherche, INRIA

Composition du Jury :

Présidente :

Isabelle BLOCH	Professeure, Télécom ParisTech

Examinateurs :

Miguel Angel GONZÁLEZ BALLESTER	Professeur, Universitat Pompeu Fabra
Grégoire MALANDAIN	Directeur de recherche, INRIA
Meritxell BACH CUADRA	Maître d'enseignement et recherche, Université de Lausanne
Elodie PUYBAREAU	Maître de conférence, EPITA

Directeur de thèse :

François ROUSSEAU	Professeur, IMT-Atlantique

Co-directeur de thèse :

Nicolas PASSAT	Professeur, Université de Reims Champagne-Ardenne

Acknowledgements

This work was supported by the ANR MAIA project, grant ANR-15-CE23-0009 of the French National Research Agency (project MAIA, "Multiphysics image-based analysis for premature brain development understanding", recherche.imt-atlantique.fr/maia), INSERM and Institut Mines Télécom Atlantique (Chaire "Imagerie médicale en thérapie interventionnelle"), Fondation pour la Recherche Médicale (FRM grant DIC20161236453) and the American Memorial Hospital Foundation.

I am especially grateful to Prof. Miguel Angel González Ballester and Prof. Grégoire Malandain for reviewing this manuscript. I appreciate their interest in my work as all of their insightful comments and suggestions. It was an honor and a privilege to have in my PhD jury Prof. Isabelle Bloch, Prof. Meritxell Bach Cuadra and Dr. Elodie Puybareau. I want to make a special mention to Isabelle who was always there since my first experience in the research area. "Merci beaucoup Isabelle, tu m'as donné envie de continuer dans la recherche".

In particular, I would like to express my special thanks to my supervisors Prof. François Rousseau and Prof. Nicolas Passat. They were very patient with me and they offered their help and support when I most needed it. For both: "merci beaucoup pour votre temps et vos leçons de recherche, vous êtes les meilleurs encadrants de thèse qu'un doctorant comme moi pouvait avoir". In particular François who was more in the first line of the supervision. His effort not only in commanding my scientific vision but also in taking care of the formation of his students, doing courses adapted to the current demand, organizing reading groups between students and teachers for giving a better criteria and facilitate the scientific discussion, being near his PhD students in their code and an endless number of other activities. "Trugarez dit Fañch !".

Naturally, my travel to the research world did not start with my PhD, but 5 years ago in Paris with an internship in Télécom ParisTech. I want to say thank you to my friends and colleagues that I met in this beautiful city. On the one hand the PhD students (now, almost all are doctors) at Télécom ParisTech: Cristian (my Colombian brother), Sylvain (we did our first marathon together), Alessio (the best Italian man), Sonia (the sweetest person in the world), Hélène (crazy and the best fan of "Friday beer"), Yifan (excellent person as well as football soccer player) ... On the other hand, my Hispanic group the "Cuisiniers" mainly composed of Moni, Luis, Carmen (now doctor and mother), Laura and Cristian (again). Thank you to all of them, you make me proud of taking the decision to have an experience in Paris. And also thank you for my friends in Barcelona: Antonio, Jorge, Holmes ...

In Brest, I met a lot of people who became important for me too: Oscar, Mathieu, Julien, Mathilde, Lucas, Nathalie, Reda, Paul, Pierre, Nicolas, Ibtissem, and all the PhD students and Postdoc in the ITI department. Specially to "rugby touché" group, "les 6 de toujours" and "nounours" team. And special mention to Blanca and Amadeo, our little Spanish group in Brest. "Gracias amigos, sin vosotros Brest no hubiese sido lo mismo, sois un amor de personas y me alegro de haberos conocido".

Now I want to say thank you to my family. To my parents, who provided me a great education and encouraged me to take my own decisions, helping me in all they could. To my brother, the person that most admired in the world and who inspired me in every important moment of my life (specially to become an engineer and go abroad in order to have another experience and meet new people, so far the best decision I took). And last but not least, to Sonia, my best friend, my girlfriend and, now, my wife. The person who most deserves to be mentioned in this work. You were always near me, giving me a life out from work, avoiding to going crazy. "Sin duda, eres la persona que más merece ser mencionada en este documento: te sacrificaste mudándote a vivir conmigo en Brest. Al lado tuyo no solo he acabado siendo doctor sino que además soy más tolerante y mejor persona. Eres la mejor, t'estimo!".

Contents

List of Figures

List of Tables

Résumé étendu

L'analyse et la modélisation d'images sont devenues des domaines prépondérants pour le développement de méthodes et d'outils impliqués dans de nombreux domaines tels que la géographie, l'astronomie ou la médecine. Au demeurant, l'imagerie médicale a permis, au cours des dernières décennies, d'accroître considérablement la compréhension fonctionnelle et anatomique du corps humain *in-vivo*. Dans ce contexte, l'usage de méthodes d'analyse d'images a participé à l'obtention de résultats que n'auraient pas permis la seule imagerie médicale.

Un exemple permettant de mettre en contexte les problématiques cliniques liées à l'imagerie médicale est le cas des enfants prématurés. En France, ils constituent 6% des naissances. Parmi eux, 55.000 par an sont de grands prématurés nés après moins de 36 semaines d'aménorrhée. Différentes études attestent que la moitié des grands prématurés présenteront des troubles cognitifs, moteurs et comportementaux. Il existe donc un besoin réel d'améliorer la prise en charge des enfants prématurés, en améliorant l'étude du développement cérébral humain.

Cette thèse se focalise sur une solution basée sur l'Imagerie par Résonance Magnétique (IRM), capable de produire des données morphologiques 3D. Ses propriétés non-invasives et non-ionisantes sont notamment bien adaptées à l'acquisition d'images du cerveau néonatal. Parmi les différentes techniques de traitement d'image, la segmentation permet d'extraire des informations quantitatives et/ou qualitatives sur différentes structures anatomiques, par exemple leur volume ou leur forme. La segmentation est une opération quasi-impossible à mener manuellement, dans le cas du traitement de plusieurs sujets ou de cohortes d'images, du fait du coût extrêmement élevé en temps nécessaire à un opérateur humain. Sous ces hypothèses, automatiser la segmentation s'avère crucial. Néanmoins, une telle automatisation fiable de la segmentation constitue un défi en traitement d'images.

En effet, la segmentation automatique des IRM cérébrales n'est pas un sujet nouveau. Depuis plusieurs décennies, de nombreux algorithmes performants ont été développés pour la segmentation cérébrale, principalement chez l'adulte. Cependant, ces succès chez les sujets et patients adultes ne se transposent pas directement dans le cas des nouveau-nés. À des problématiques liées à la difficulté d'acquérir des images 3D dans de bonnes conditions (temps d'acquisition réduits, risques de mouvements), s'ajoutent :

- des difficultés d'interprétations liées à l'immaturité de certaines structures cérébrales ; par exemple, myélinisation partielle de la substance blanche menant à des inversions de contrastes ;
- la grande variabilité inter-sujet, à cause des différents temps de gestation au moment de la naissance ou les déformations physique dues, par exemple, au caractère non-rigide du crâne des nouveau-nés ;
- la taille réduite des structures d'intérêt, comme celle de la substance grise au niveau du cortex.

Ces facteurs (Fig. 1) vont, par exemple, se traduire dans les effets de volume partiel, liés à la résolution des images, où certains points (principalement localisés aux frontières entre différentes structures) vont présenter une intensité moyennée par les structures présentes dans les voxels.

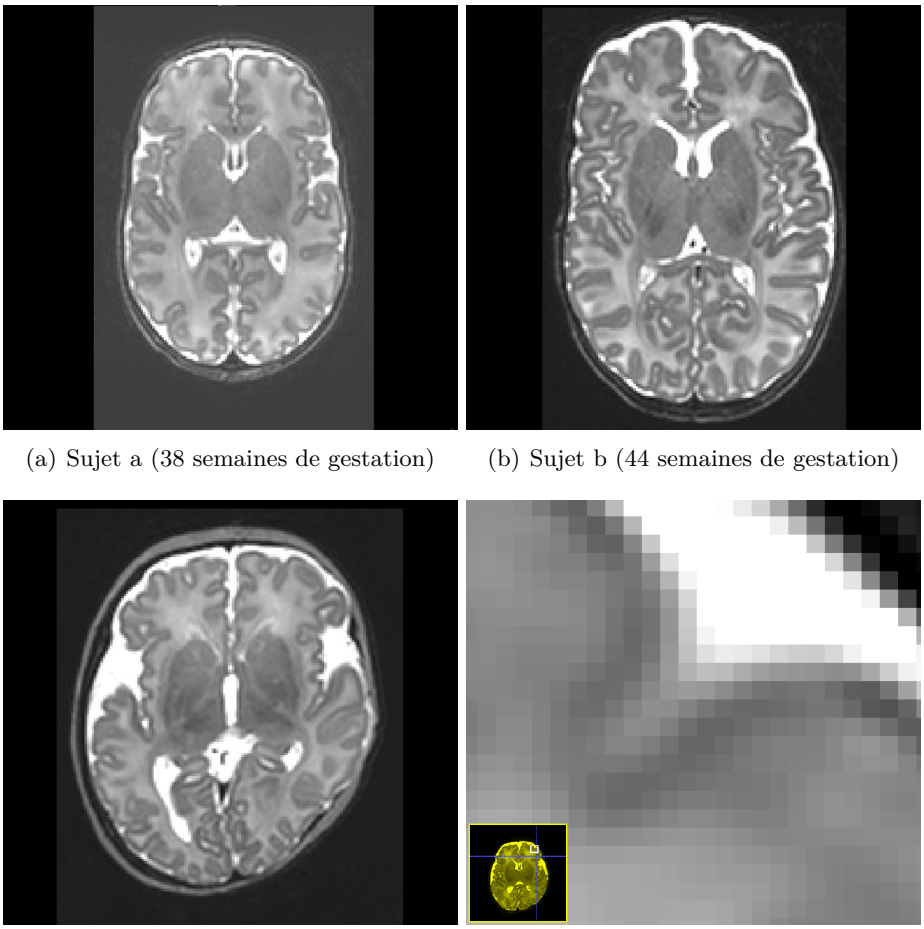

(a) Sujet a (38 semaines de gestation) (b) Sujet b (44 semaines de gestation)

(c) Sujet c (44 semaines de gestation) (d) Zoom de la zone corticale

FIGURE 1 – IRM cérébrales de nouveau-nés pondérées en T2 présentant la problématique particulière de la segmentation automatique chez le nouveau-né. Les images de (a)-(c) présentent la variabilité entre sujets où les différences entre âges de gestation sont visibles entre (a) et (b) et les différences morphologiques entre (b) et (c), qui ont tous les deux le même âge de gestation. L'image (d) présente le problème de volume partiel au niveau de la surface corticale.

L'analyse des structures cérébrales chez le nouveau-né peut s'avérer déterminante. En effet, les résultats d'une telle analyse peuvent être utilisés comme biomarqueurs de lésions quantitatives (un défaut de croissance est susceptible d'être mis en lien avec des troubles cognitifs), pour l'évaluation des effets neuroprotecteurs des essais thérapeutiques utilisés en néonatalogie (par exemple, neuroprotection par mélatonine), ou encore pour mettre en place une prise en charge rééducative personnalisée pour stimuler la plasticité cérébrale. Parmi ces structures, le cortex, qui se caractérise par une faible épaisseur, demeure difficile à segmenter dans les images IRM de nouveau-nés, mais fait néanmoins partie des structures d'intérêt crucial [Kim et al., 2016].

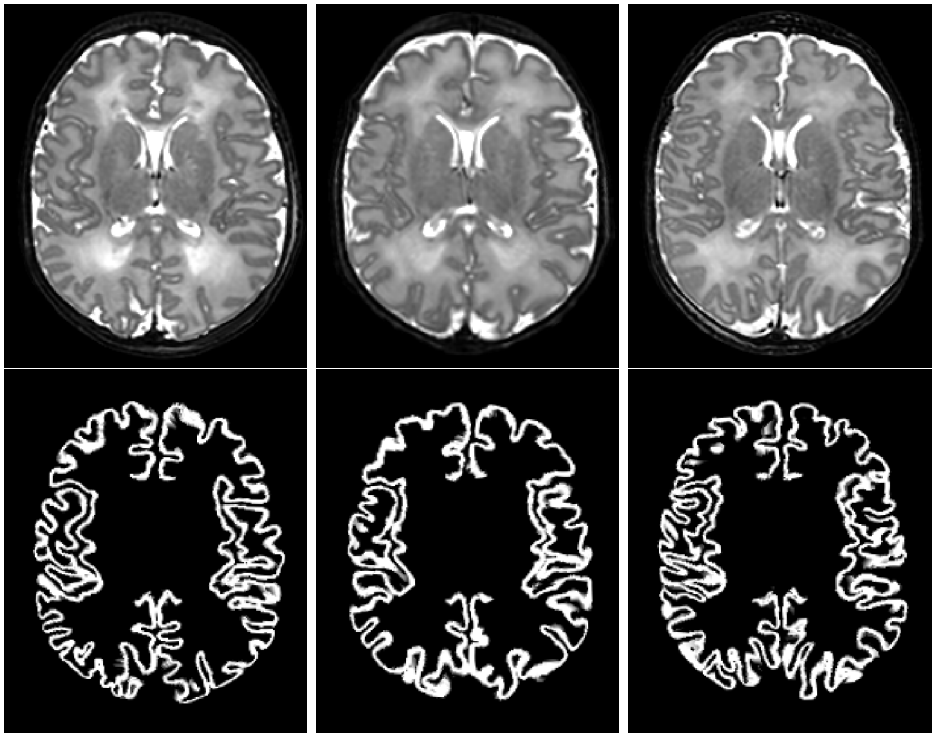

FIGURE 2 – Images de différents sujets recalés à une même image qui mettent en évidence les erreurs de recalage. En haut, les IRM pondérées en T2 recalées et, en bas, leurs segmentations par recalage.

L'objectif de cette thèse est de proposer une méthode de segmentation automatique pour la surface corticale dans des IRM de nouveau-nés. De plus, les résultats de segmentation devront atteindre un niveau de qualité suffisant pour pouvoir être traités de manière subséquente par une autre technique d'analyse d'image et de modélisation (par exemple la génération de maillage surfacique).

Plusieurs méthodologies ont été explorées dans l'état de l'art (morphologie mathématique [Gui et al., 2012, Morel et al., 2016], modèles déformables [Leroy et al., 2011, Schuh et al., 2017], classification [Beare et al., 2016, Moeskops et al., 2015]). Au-delà des techniques de traitement d'images mises en jeu, l'utilisation d'approches dites multi-atlas [Makropoulos et al., 2014, Cardoso et al., 2013, Weisenfeld and Warfield, 2009, Iglesias and Sabuncu, 2015] a démontré une bonne capacité à tirer parti du maximum d'information disponible à partir de bases de cas, dans un contexte où les connaissances a priori permettent de compenser la faible qualité et la complexité des données acquises.

Suivant le schéma de l'article d'état de l'art [Iglesias and Sabuncu, 2015], les méthodes multi-atlas comportent trois étapes principales : (1) recalage, (2) propagation des segmentations et (3) fusion des segmentations. Cette thèse se focalise sur la troisième étape, la fusion de labels, en utilisant les atlas suivant un paradigme non-local. Ce paradigme utilise la notion de patch (petit fragment d'image, généralement sous forme de carré ou de cube) pour déterminer la similarité des atlas avec l'image à segmenter. Pour être robuste aux erreurs de recalage (Fig. 2), une extraction de tous les patchs, limitée par une fenêtre de recherche, est utilisée dans chaque atlas pour évaluer la similarité entre les structures observées [Rousseau et al., 2011, Coupé et al., 2011].

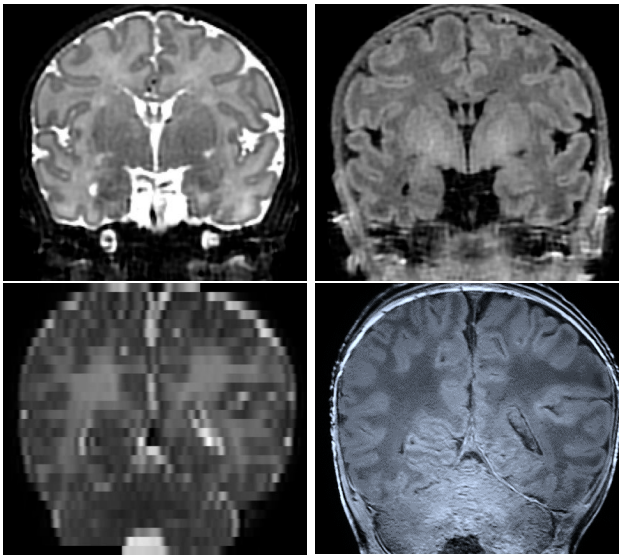

FIGURE 3 – Visualisation d'images utilisées à des fins différentes. En haut, un exemple d'acquisition IRM orientée recherche et, en bas, une acquisition clinique. Les images de gauche correspondent à la pondération T2 et, à droite, à la T1.

En général, la problématique de la segmentation cérébrale du nouveau-né dans l'état de l'art, est traitée à partir de données garantissant une certaine qualité d'image (résolution quasi-isotrope, bon rapport signal sur bruit, etc.) pour simplifier la problématique. Par contre, ces données, loin d'être nombreuses, ont des spécificités bien différentes de celles utilisées dans le milieu hospitalier (Fig. 3). Cette thèse évalue l'impact de l'état de l'art en segmentation automatique d'IRM cérébrale néonatale dans le contexte clinique.

La plupart des méthodes développées pour la segmentation des structures anatomiques, et notamment celles dédiées au cortex cérébral, commettent des erreurs liées à la topologie des objets observés : régions isolées, connexions ou déconnexions erronées... Une manière de résoudre ce problème consiste à corriger la topologie des structures extraites. Pour cela, il existe principalement deux types de stratégies : une correction locale et une correction globale de la topologie. La première localise les zones conflictuelles où se situent probablement les erreurs topologiques, puis classifient ces erreurs pour appliquer une correction adaptée [Shattuck and Leahy, 2001, Han et al., 2002, Sun et al., 2019]. Pour leur part, les méthodes globales visent à contrôler la topologie de l'objet binaire et être sûr de sa topologie tout au long du processus [Mangin et al., 1995, Fischl et al., 2001, Ségonne et al., 2007]. Cette thèse s'est focalisée sur les méthodes de déformations homotopiques basées sur la modification des points simples [Malandain et al., 1993, Bazin and Pham, 2007a, Mazo et al., 2012b]. Ce type de déformations permet de préserver une topologie initiale du début à la fin de l'application de la méthode. L'idée est d'utiliser cet outil pour faire évoluer une structure topologiquement correcte et géométriquement simple (ex. une sphère creuse) vers un objet final plus complexe (tel que le cortex) tout en préservant sa topologie (Fig. 4).

Cette thèse est organisée de la façon suivante.

Le chapitre 2 propose un nouvel algorithme de segmentation itératif automatique basé sur les multi-atlas et les patchs. L'état de l'art en matière de segmentation cérébrale néonatale est présenté, avec un accent particulier sur les méthodes multi-atlas. Une analyse des hypothèses couramment utilisées dans la littérature est discutée, en présentant des expériences. Cette discussion justifie le choix de notre première contribution.

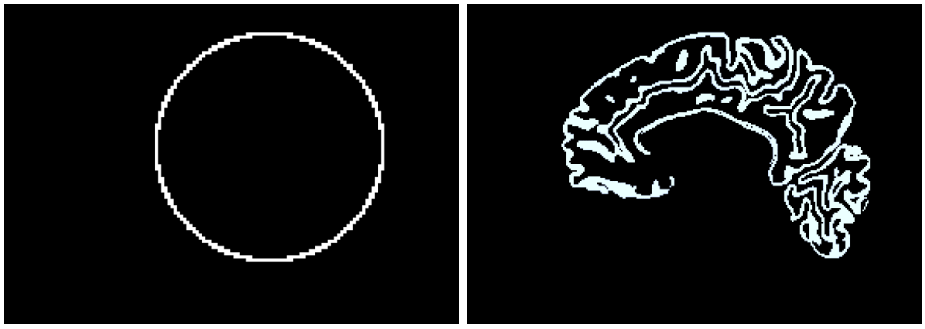

FIGURE 4 – Visualisation de deux coupes d'images 3D dans le plan sagittal : à gauche, une sphère creuse ; à droite, la même image après une déformation homotopique qui s'adapte à la forme d'un cortex.

Le chapitre 3 présente la problématique du traitement d'une véritable IRM clinique au lieu d'acquisitions spécifiquement conçues à des fins de recherche. Un pipeline entièrement automatique est proposé, principalement basé sur une combinaison de méthodes de super-résolution (SR) et d'approches multi-atlas. Différentes combinaisons de méthodes existantes sont évaluées en termes de robustesse et de performance.

Le chapitre 4 présente la nécessité de fixer une topologie spécifique aux structures anatomiques segmentées afin d'éviter des erreurs dans la segmentation. Les algorithmes de pointe utilisant la préCette thèse s'est focalisée sur les méthodes de déformations homotopiques basées sur la modification des points simples [Malandain et al., 1993, Bazin and Pham, 2007a, Mazo et al., 2012b].

servation topologique à des fins de segmentation sont discutés. Un algorithme de post-traitement est proposé pour ajouter une cohérence topologique à la surface corticale.

Le chapitre 5 conclut cette thèse et présente les perspectives de travaux futurs tels que la généralisation de différentes structures ou l'application à différents domaines du traitement d'images, des alternatives au pipeline de segmentation pour des IRM cliniques néonatales et des améliorations pour l'algorithme de segmentation topologique.

Acronyms

2D	two-dimensional
3D	three-dimensional
T1w	T1-weighted
T2w	T2-weighted
MRI	Magnetic Resonance Imaging
MR	Magnetic Resonance
CT	X-ray Computed Tomography
US	Ultrasounds
WM	white matter
GM	grey matter
CSF	cerebrospinal fluid
GA	gestational age
PVE	partial volume effect
SNR	signal-to-noise ratio
INU	intensity inhomogeneity
CNR	contrast-to-noise ratio
SR	Super-Resolution
LR	low-resolution
HR	high-resolution
dof	degree of freedom
GMM	gaussian mixture model
EM	Expectation Maximisation
NLM	non-local means
N3	nonparametric nonuniform normalisation
CNN	convolutional neural networks

BET	brain extraction tool
KNN	k-nearest neighbours
SVM	support vector machine
MAS	multi-atlas segmentation
MRF	Markov random field
SAP	shape-adaptive patches
JLF	Joint Label Fusion
LLE	Locally Linear Embedding
GAN	generative adversarial network
SPM	statistical parametric mapping
FWHM	with the full-width-at-half-maximum

Image datasets

This thesis presents some methods and experiments concerning the neonatal brain segmentation that were tested and validated using different datasets. All these datasets have T2 weighted MR images, which, to the best of our knowledge, is the best modality for segmenting brain tissues in neonatal MRI. These images were endowed with a set of reference segmentation maps, which is required for performing the evaluation of image analysis algorithms.

Dataset information

In the following paragraphs, we have collected the main information of each dataset used.

- **dHCP**

  The Developing Human Connectome Project (dHCP)[1] is provides an extensive 4-dimensional dataset focused on the connectome of early life, made available by [Hughes et al., 2017]. This has the goal to enhance the understanding of the brain development discovering new patterns in anatomical and functional modes. Infants were recruited and imaged at the Evelina Neonatal Imaging Centre, London. Informed parental consent was obtained for imaging and data release, and the study was approved by the UK Health Research Authority. This large dataset was used in [Makropoulos et al., 2018] and it collects 465 subjects between 28 and 45 weeks of gestational age (GA) in several MRI-based modalities.

  In this context, a part of the whole dataset is used for testing and validating our methods. This subset consists of T2-weighted and T1-weighted MRI data with the main brain tissue segmentation map (cortex, white matter, cerebrospinal fluid, ventricles, brainstem and cerebellum). All infants were born and imaged at term age (37–44 weeks of age). Imaging was carried out on 3T Philips Achieva using a dedicated neonatal imaging system which included a neonatal 32 channel phased array head coil. The infants were imaged in natural sleep. T2w and T1w images were acquired in sagittal and axial slice stacks with in-plane resolution 0.8×0.8 mm^2 and 1.6 mm slices overlapped by 0.8 mm. Other parameters were: $12,000/156$ ms TR/TE, SENSE factor 2.11 (axial) and 2.58 (sagittal) for T2w, and $4,795/1,740/8.7$ ms TR/TI/TE, SENSE factor 2.27 (axial) and 2.66 (sagittal) for T1w. In this thesis, a set of 40 images with a voxel size of $0.5 \times 0.5 \times 0.5$ mm^3 is considered.

- **MAIA**

  The Multiphysics image-based AnalysIs for premature brAin development understanding (MAIA) is a project funded by the French National Research Agency

[1] `http://www.developingconnectome.org`

(ANR) that aims to provide algorithms and methods for multi-image / multi-signal analysis to enhance the neurodevelopement understanding. This project collaborates with Epirmex, which is focused on researching the brain abnormalities in brain MRI at term age and executive and linguistic functions of very preterm infant (less than 32 weeks after amenorrhea). This thesis has been provided with a large dataset of preterm MRI scans (110 subjects) acquired at term-equivalent age.

The dataset provided consists of 110 subjects with T2w and T1w images; two of them are manually segmented by an expert. Both modalities were acquired following different configurations. T2w images were acquired in sagittal and coronal slice with in-plane resolution of 3.0 mm. They have a anisotropic resolution $0.7 \times 0.7 \times 3.0$ mm^3 with 3000/200 ms for TR/TE respectively. However, T1w images were acquired in sagittal and axial slice with in-plane resolution of 3.0 mm. They have a anisotropic resolution $0.8 \times 0.8 \times 1.2$ mm^3 with 2200/3.2 ms for TR/TE respectively. Manual segmentation were created using the T1w images, which have the highest resolution of both. In this thesis, the final resolution used was a $0.45 \times 0.45 \times 3.0$ mm^3 for T2w images and $0.27 \times 0.27 \times 1.2$ mm^3 for T1w images.

- **NeoBrainS12**

  NeoBrainS12 was a challenge proposed in MICCAI 2012 conference in Nice. The challenge consisted of segmenting different tissues of neonatal brain using three different datasets:

  - Axial 40 weeks: 7 T1w and T2w images with a resolution $0.94 \times 0.94 \times 2.0$ mm^3 and $0.54 \times 0.61 \times 2.0$ mm^3 respectively. Final resolution was $0.35 \times 0.35 \times 2.0$ mm^3 for both.
  - Coronal 30 weeks: 7 T1w and T2w images with a resolution $0.93 \times 0.93 \times 2.0$ mm^3 and $0.64 \times 0.53 \times 2.0$ mm^3 respectively. Final resolution was $0.34 \times 0.34 \times 2.0$ mm^3 for both.
  - Coronal 40 weeks: 5 T1w and T2w images with a resolution $0.91 \times 0.78 \times 1.2$ mm^3 and $0.89 \times 0.78 \times 1.2$ mm^3 respectively. Final resolution was $0.78 \times 0.78 \times 1.2$ mm^3 and $0.35 \times 0.35 \times 1.2$ mm^3 for T1w and T2w respectively.

  The challenge provided comparative results for each algorithm involved in the challenge. In this thesis, we used only the Axial 40w dataset, which has the highest quality in terms of segmentation maps. The available manual segmentation maps are two of them.

Dataset index

In order to find easily the datasets in this document, we provide a list of sections where they appear.

- **dHCP**:
  - Chapter 2: data for training (atlas set with 30 subjects) and testing (with 10 subjects) automatic segmentation algorithms;

  - Chapter 3: data for training (atlas set with 40 subjects) most of the methods of super resolution and segmentation;
  - Chapter 4: data for testing the topological correction algorithm proposed;
  - Chapter 5: data used to illustrate the perspective;
  - Appendix B: data used to segment the CSF and WM structures with IMAPA.

- **MAIA**:
  - Chapter 3: data for testing the pipeline segmentation (with 2 subjects);
  - Appendix A: data corrected from the intensity irregularities.

- **NeoBrainS12**:
  - Chapter 3: data for testing the segmentation pipeline (with 2 subjects);

Chapter 1

Introduction

Motivation

During the last centuries, humanity has been trying to understand experimentally and theoretically the human brain mechanism. This research motivated the specialisation of science in different subfields such as the modern medicine, psychology or biochemistry. Nowadays, thanks to the improvements in research and technology (e.g. medical imaging), we are able to answer many questions and understand most of the human brain functionalities. However, much about the brain is still a mystery, in particular in the understanding of the brain development. Many studies have proved that brain formation starts at the earliest embryonic stages, migrating neurons to the cortical surface, and creating new neurons and connections mainly before the birth [Purves and Lichtman, 1985]. Therefore, the need to explore the brain of fetus and neonatal infants is essential.

In addition, there is also a crucial interest in analysing the neonatal brain to detect or prevent possible pathologies or lesions early presented. In particular, the premature newborn has a special interest for its non-well developed brain. For instance, a french study named EPIPAGE 2 [Ancel et al., 2014] argues that each year in France 55,000 infants are born prematurely (before 37 weeks of amenorrhoea). Among them, 10,000 will be extremely premature (less than 32 weeks). Current studies [Whitfield et al., 1997, Lorenz et al., 1998, Markestad et al., 2005] predict that most of them may have motor, cognitive or behavioural diseases.

The brain morphometry provides measurements and detection changes on the different subparts of the brain in order to extract relevant information that could extrapolate to an endless number of applications. This can be translated to extract relevant biomarkers [Filipek et al., 1994] or significant differences around spatiotemporal data [Verma et al., 2005]. In clinical routine, it may provide methodologies in order to perform an aid of diagnosis, prediction of diseases or therapy. In general, studies are performed focusing on a specific region or structure [Makris et al., 1997, Csernansky et al., 1998, Fearing et al., 2008] Among the brain subparts, many recent works were focused on the cortex as a region of interest for cortical connectivity [Ball et al., 2013a], cortical develop-

ment [Ball et al., 2013b, Yu et al., 2016] and brain folding [Dubois et al., 2008, Lefèvre et al., 2016, Orasanu et al., 2016].

In order to study the brain morphology *in-vivo*, many existing modalities in medical imaging can provide a 3D visualisation and quantification such as X-ray computed tomography (CT), ultrasounds (US) or magnetic resonance imaging (MRI). Among those modalities, MRI and US are particularly adapted to the neonatal infant, due to their non-ionizing and non-invasive properties. However, only the MRI provides enough spatial resolution and a low noise level in order to achieve a study properly.

Segmentation of brain MR images is one of the most prominent tasks in order to attempt a brain morphology analysis. The information of a segmented structure combined with some meta-data of the MRI can provide a satisfactory approximation of its volume, depending mostly on the resolution and other properties of the MRI. However, a proper manual segmentation is a tedious and time consuming task that requires an anatomical expert, typically a radiologist. Thus, making the segmentation automatically is a major research need and, eventually, clinical purpose.

Segmentation in Neonatal MRI: an image processing challenge

During the last decades, MRI brain segmentation has received considerable advancement leading to the creation of several methods, pipelines and softwares that attempt the segmentation and parcellation of the brain and its subparts with satisfactory accuracy. However, these efficient tools cannot be applied to the newborn, whom MRI properties and acquisition context modify the issue, generating a new open question in research. In order to explain this gap, we can list the following reasons:

- The inversion of the image contrast is one of the main differences between adult and neonatal MRI. This effect is produced by the maturation process of the structures such as the myelination of the white matter (WM), which generates an acceleration of the neuron connections. The maturation myelination changes the contrast week-by-week, reaching around the 9 months that the intensity levels of the cortical grey matter (GM) and the WM are practically equal [Barkovich, 2005]. The tissue continues maturating until the first two years of the infant when it reaches the intensity level profile of an adult brain.

- Neonatal brain is clearly smaller than the adult one; thus the structures of interest are thinner too. The MRI resolution is often limited around 1mm^3, which is insufficient margin between the thinnest subparts of the brain in order to be able to distinguish them. This issue is known as the partial volume effect (PVE) and it is mainly located inside the borders between structures. In those locations, some points will belong to multiple structures, leading to a weighted average of the corresponding intensity levels, which hampers the label assignation. This effect is particularly intense in the cortical surface, where the cerebrospinal fluid (CSF), the subcortical GM and the WM are in conflict [González Ballester et al., 2002].

- The neonatal brain grows and varies with a huge speed (Figure 1.1). The variability of the gestational age (GA) in infant birth, measured in weeks after the amenorrhoea, determines a specific size and shape. A study done with 78 babies [Hüppi et al., 1998] states that each week the brain grows 22 cm^3. Therefore, the morphology of the brain is extremely sensitive to the age.

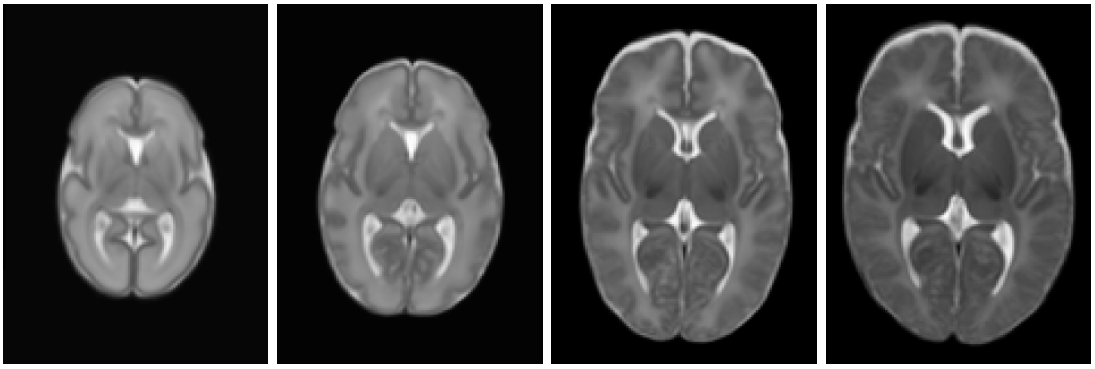

Figure 1.1 – Representation of differences in terms of shape and size in neonatal T2 weighted MRI depending on the gestational age. Images are constructed from 204 premature infants [Serag et al., 2012]. From left to right: extremely preterm age (28w), preterm age (33w), term age (39w) and post term age (44w).

- The smoothness of the neonatal brain or possible diseases may introduce stronger deformations on the neonatal cerebral morphology average than in adult. This significant inter-subject variability is independent to the age-specific changes. In addition, some studies show that a preterm infant with the age of a term infant present significant differences (Figure 1.2) making the shape difficult to predict even if the age of the subject is known.

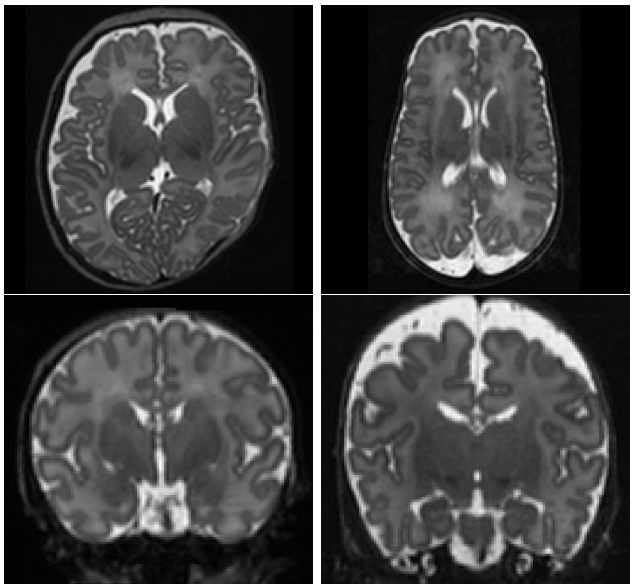

Figure 1.2 – Representation of inter-subject variability in neonatal T2 weighted MRI. Images are term and preterm subjects extracted from the ALBERT dataset [Gousias et al., 2012]. First row, a term newborn (left) and a 28w born preterm acquired at the same age (right). Second row, two premature subjects at the same age (39w).

- Motion artefacts are more common in neonatal MRI than in the adult images since the newborn baby cannot follow oral instructions coming from the MRI technician in order to provide appropriate conditions for the exam. Typically, the acquisition is done after having fed the baby, during the nap, thus time acquisition has to

be shorter. This fact causes a reduction in the contrast-to-noise ratio (CNR), increasing the complexity to differentiate tissues inner the brain.

- The trade-off between CNR and time acquisition of the MRI exam is also compensated by obtaining less slices in a specific axis. As a result, a proper resolution in one 2D plane, orthogonal to the chosen axis, is obtained for a clinical purpose. However, the anisotropic resolution of a 3D image makes difficult the segmentation task due to the loss in details in the other two planes (Figure 1.3).

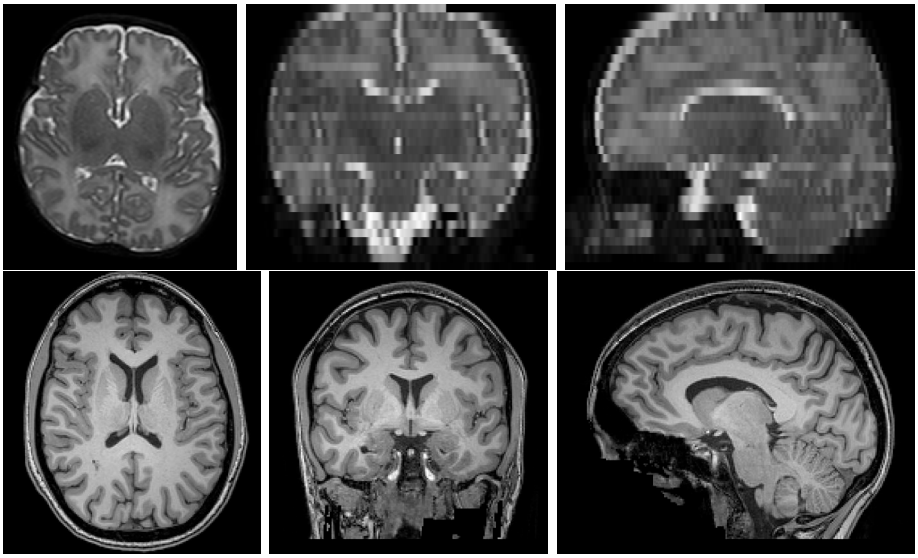

Figure 1.3 – First row, a clinical T2 weighted MRI from the MAIA dataset (subject S00059). It presents a strong anisotropic resolution across the coronal and sagittal planes ($0.45 \times 0.45 \times 3$ mm). Second row, an adult T1 weighted MRI from the dataset NKI-RSS-22 (subject 1). It presents an isotropic resolution ($1 \times 1 \times 1$ mm).

In addition, the common issues in adult MR images still remain in the newborn images, such as the intensity inhomogeneity / non-uniformity (INU) or noise. The INU is produced as a consequence of the radiofrequency pulse emitted to interfere the magnetic alignment of the hydrogen spins, which is not completely homogeneous inside the body. Noise in MRI can be caused by the electromagnetic noise of the body and coils receptors.

Segmentation of cortical surface: application to surface meshing

Globally, the segmentation procedure is a step followed by one or more tasks. In clinical context, these tasks are related on modeling anatomical structures that allow us to enhance our knowledge in order to propose better treatments, aid the clinician decision or predict diseases. Therefore, the success of many applications depends on the accuracy of the segmentation step.

As explained in section 1.1.1, neonatal brain MRI is challenging for automatically extracting cerebral subparts; in particular the cortex has specific factors that deserve additional emphasis. The main factors that hinder the effectiveness of the conventional image processing methods are determined by:

- The variability of the shape and width of the cortex, e.g. due to the cortical folding. This factor hampers the use of example based methods without any preprocessing step. These approaches are commonly preceded by a registration process that likely introduces errors such as those arising from the interpolation. Another method with issues is the feature extraction approach based on a specific pattern such as Hough transform or scale-invariant feature transform (SIFT), which will be difficult to find a generic feature set in order to determine the cortex.

- The thin thickness of the cortex, where the PVE is the main liable for misclassification. The application of algorithms based on intensity such as histogram profile (e.g. Gaussian mixture model), mathematical morphology (e.g. watershed) or active contours will introduce several misclassified points where the PVE is located.

- Deformation of the whole brain as a consequence of the brain softness or a pathology. This means that there are significant differences between the appearance of each subject. As presented above, a common preprocessing step is to register one subject to another. Registration algorithm will have difficulty finding the proper deformation in order to, for example, introduce spatial priors such as in a multi-atlas method.

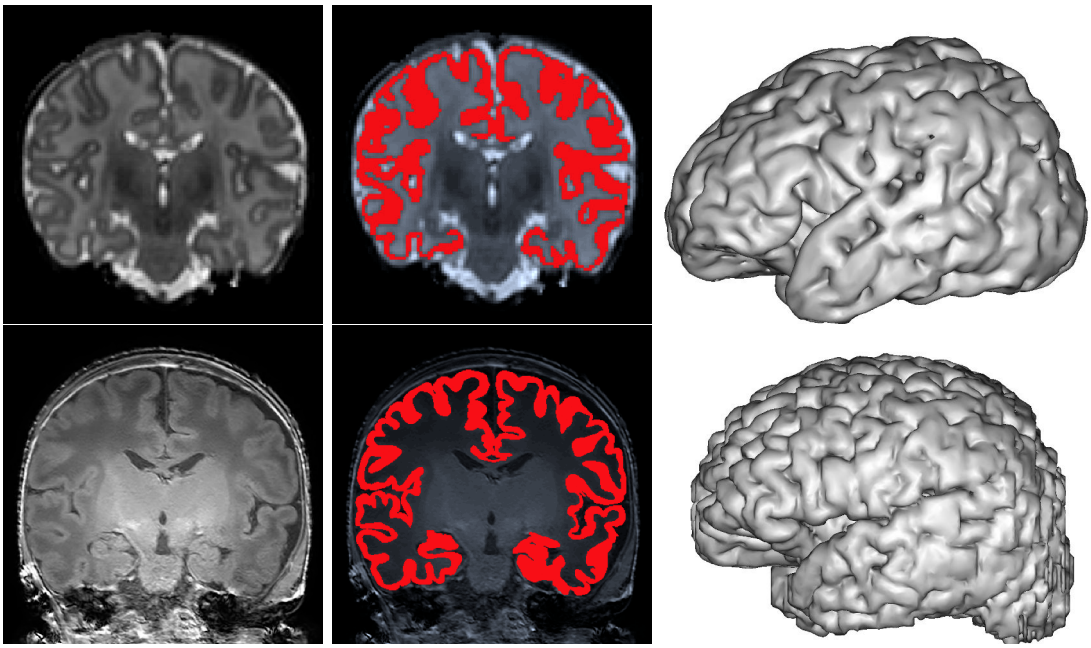

Figure 1.4 – Two examples of cortex segmentation from two different datasets: on top, a T2w image from ALBERT dataset and on bottom, a T1w image from MAIA dataset. From left to right: MR image, a manual segmentation of the cortex overlapping MR image and a mesh generation obtained from BrainVISA software[1].

In this challenging context, one of the applications of the binary segmentation is to generate a mesh of the target brain structures, i.e. usually a 3D surface representation obtained typically with a triangular surface or tetrahedral volumes. This technique of

[1] `http://brainvisa.info`

computer vision provides to the clinicians a tool in order to better understand structural morphology of a particular subject, locate lesions or tumours for brain surgery, or facilitate population studies.

Mostly, the mesh generation algorithms require a segmentation image with specific conditions in order to obtain a fine quality mesh. For instance, it usually helps to have the input segmentation as a closed surface. This makes challenging the mesh generation in neonatal cortical surface due to its extremely thinness which is sometimes around 2 voxels of thickness depending on the image resolution. The typical errors are the discontinuities in the segmentation or the coarse cortical foldings. This leads to undesired "holes" or "tunnels" in the mesh generation, unrealistic connections or attached cortical folding, losing details in the visualization.

Thesis overview

The aim of this thesis is to develop an efficient and robust algorithm for cortical surface adapted to the neonatal brain MRI issue. The main contributions are:

- An automatic method for cortex segmentation of a neonatal brain MRI. The algorithm is part of the multi-atlas segmentation family whom aim is to weight the atlas information using similarities between the target image and the atlas set. The notion of patch is used as comparison unit for computing these similarities [Rousseau et al., 2011, Coupé et al., 2011], which is defined as a distance. The major novelty lies in using the estimated segmentation to compute this distance as a regularisation which is introduced iteratively.

- An evaluation of the robustness of the multi-atlas methods for segmenting the cortex in clinical MRI. Clinical data used for this evaluation have different properties than the conventional data used for research, in particular the strong anisotropic resolution that decreases the effectiveness of 3D segmentation algorithms.

- A pipeline using a combination of a super-resolution (SR) and multi-atlas segmentation methods applied to the clinical neonatal brain MRI. Different existing methods of both techniques are tested in order to evaluate the performance and robustness of the proposed tool.

- A topological correction in post-processing for brain MRI segmentations. This algorithm works in multilabel taking several segmentations in binary or probabilistic map form as a reference segmentation. It starts with an image of labels with a desired topology. A cost function links the image of labels and the reference segmentations. This cost function is iteratively optimized using a multiscale strategy. In particular for this thesis it has been studied for 3 labels: WM, cortex and CSF+background.

Thesis organisation

This thesis is organised as follows:

Chapter 2 proposes new automatic iterative segmentation algorithm based on multi-atlas and patches. The state-of-the-art regarding the neonatal brain segmentation is presented, with special emphasis on the multi-atlas family methods. An analysis of the

assumptions commonly used in the literature is discussed, including experiments. This discussion leads to the creation of our first contribution.

Chapter 3 introduces the problematic of processing real clinical MRI instead of research-oriented acquisitions. A fully-automatic pipeline is proposed mainly based on a combination of super-resolution (SR) methods and multi-atlas approaches. Different combinations are evaluated in terms of robustness and performance.

Chapter 4 presents the need for fixing a specific topology to anatomical segmented structures in order to avoid errors in the segmentation. The state-of-the-art algorithms using topological preservation for segmentation purpose is discussed. A post-processing algorithm is proposed to add a topological coherence to the cortical surface.

Chapter 5 concludes this thesis and introduces perspectives for future works such as the generalisation of different structures or the application to different image processing domains such as image synthesis or high-resolution (HR) reconstruction.

Chapter 2

Multi-Atlas Segmentation Approach for Neonatal MRI

Introduction

In computer vision, the segmentation is usually mistaken with the classification. Indeed, the classification is a process that grants a class to an image. The segmentation is a task that extracts an object or a region of interest form the image, providing the exact number of points (pixels for a 2D image and voxels for a 3D image) concerned. In other words, the segmentation is like classifying each point of the image, providing its membership to a class. For instance, let us suppose a picture containing a table, the classification will link the image to a class called "table" and the segmentation will provide the cloud of point belonging to the table.

The output of a segmentation process can expressed as a binary or fuzzy image. The binary output is an image that puts the high value, e.g. 1, to the target object or

region of interest and the rest to the low value, e.g. 0. However, this type of output, also called hard segmentation, does not take into account problem areas where the class membership of a point is difficult to determined. As we presented in the previous chapter, these areas can be produced by several factors that make difficult the automatic segmentation. In contrast, the fuzzy segmentation has a range of continuous values (commonly between zero and one) that provides a certain degree of class membership for each point. This kind of segmentation can be interpreted as a probabilistic map that adapts the ambiguous areas with a degree of membership.

Overview of neonatal segmentation methods

Nowadays, the wave of algorithms based on deep learning is covering every research field. Popularized by the convolutional neural networks (CNN) [LeCun et al., 1998], the emergence of big data and the outperformed score of ImageNet [Krizhevsky et al., 2012] consolidated the use of this type of methodology to computer vision and image processing. In medical imaging this tendency also took place, with an incredible amount of research papers published every year [Shen et al., 2017], creating, for instance, new specific architectures for segmentation purpose [Ronneberger et al., 2015]. Concerning the segmentation of brain MRI [Akkus et al., 2017], there are many advances in neonatal challenges, such as cortical segmentation in isointense MRI [Dolz et al., 2018, Zhang et al., 2015] or versatile algorithms robust to the subject age variability [Xu et al., 2018, Moeskops et al., 2016]. However, these techniques usually need huge datasets in order to be trained, tested and validated. In neonatal MRI, there is not a extensive data since the practice of a MRI acquisition in newborn infant is uncommon; thus MRI manually annotated by an expert are limited.

With these conditions, many other types of method were recently proposed for neonatal brain MRI segmentation. From a technical point of view, different approaches have been explored: mathematical morphology [Gui et al., 2012, Morel et al., 2016], deformable models [Leroy et al., 2011, Schuh et al., 2017], classification [Beare et al., 2016, Moeskops et al., 2015, Anbeek et al., 2013], patch-driven level set approaches [Wang et al., 2014], probabilistic modeling [Cardoso et al., 2013] or atlas-based approaches [Weisenfeld and Warfield, 2009, Wang et al., 2013a].

In addition to the type of segmentation (i.e. hard or fuzzy), brain segmentation can be classified in terms of the number of regions of interest provided (when it is more than one, it is usually called multilabel). Traditionally, algorithms classify the intracranial tissues in GM, WM and CSF [Xue et al., 2007, Leroy et al., 2011, Wang et al., 2013b]. Alternatively, some methods split the GM into cortical and subcortical, or the WM into myelinated and unmyelinated, or identify the ventricles, brainstem and cerebellum, extending the result to 7 or 8 classes [Gui et al., 2012, Anbeek et al., 2013]. Finally, some approaches are interested in segmenting 50 anatomical structures [Gousias et al., 2013, Makropoulos et al., 2014, Makropoulos et al., 2018].

Usually, segmentation methods need a preprocessing step in order to enhance the properties of the target image, facilitating the processing task. In the literature, the main preprocessing steps are brain extraction and intensity correction. There are several methods for brain extraction that were applied to the neonatal MRI [Serag et al., 2016, Doshi et al., 2013, Shi et al., 2012, Dai et al., 2013, Kleesiek et al., 2016, Eskildsen et al., 2012, Smith, 2002]. The brain extraction is commonly applied before tissue segmentation in order to avoid possible errors introduced by the methodology, e.g. in registration task. In contrast, the correction of MRI bias field is computed by an efficient approach

called nonparametric nonuniform normalisation (N3) [Sled et al., 1998], which maximizes intensity distribution in a frequency space. Later, it was updated to N4 [Tustison et al., 2010], which has a later version of B-spline and a hierarchical optimization. N3 and N4 algorithms are both implemented and available in ANTs software[1] [Avants et al., 2008]. An alternative to them was introduced in [Mangin, 2000], which is focused on the minimisation of the entropy.

Multi-atlas segmentation

Among the cited techniques, the so-called atlas or multi-atlas framework [Cabezas et al., 2011, Iglesias and Sabuncu, 2015] has a relevant impact due to its performance and robustness for brain segmentation purpose. This leads to a strong trend during the last years, relying on the atlas-guided segmentation for medical imaging, in particular in neonatal brain MRI [Devi et al., 2015, Makropoulos et al., 2017]. These techniques are usually performed by registering an anatomy textbook [Miller et al., 1993] onto the image to be segmented. The main advantage of the atlas-based approaches is to provide a spatial prior (typically registered to the target image) for each region of interest that restricts the result to a more realistic anatomy.

The difference between atlas or multi-atlas varies according to the number of atlas used. Atlas-based techniques became popular in the nineties [Christensen et al., 1997, Collins et al., 1995, Lancaster et al., 1997]; they were focused on finding an efficient registration, leading to use a single atlas to simplify the registration task. More recently, the use of multiple atlas for segmentation purpose, so-called multi-atlas segmentation (MAS), is standardized due to the improvement in registration algorithms [Klein et al., 2010] and the increase in computational resources. The increase in the number of atlas enhances the robustness to strong variability in shape and size of desired structures [Doan et al., 2010].

As presented in [Iglesias and Sabuncu, 2015], there are three main steps in MAS. First, the intensity images from the atlas set are registered to the target image. This produces a transformation that maps the atlas space to the target image space. Second, the segmentation images are propagated to the target image space using the mapping obtained in the previous step. Third, the propagated segmentations are combined to obtain the target segmentation. This step is called the label fusion.

There are two types of atlases [Makropoulos et al., 2017]: the probabilistic atlas and the single-subject atlas. Probabilistic atlas is a dataset with a unique pair of images, i.e. an intensity image and a segmentation image. This pair is often the result of a pre-processing step that fuses a stack of example images with their manual segmentation. The averaged intensity image and the probabilistic segmentation map (i.e. fuzzy segmentation) is the result of the probabilistic atlas. Beyond the benefits of reducing atlas warping to one, the combination of these pairs was recently used [Makropoulos et al., 2014, Makropoulos et al., 2016, Schuh et al., 2015] in order to summarise a relevant feature, e.g. age, disease, specific population, etc. On the other hand, the single-subject atlas is a simple pair of intensity and segmentation images from a subject. In general, the segmentation image is a hard segmentation, manually segmented by an expert, which maps each point of the intensity image to a specific class or structure.

Distinctively, MAS starts with a registration step that warps each atlas for being close in appearance to the target image, providing a mapping for each transformation. Each deformation process is made by maximizing the similarity between both images. There

[1] `http://stnava.github.io/ANTs`

are different kinds of deformation: linear, i.e. rigid or affine, or nonlinear depending on the strategy defined as global or local, respectively. Rigid registration uses 6 degrees of freedom (*dofs*), i.e. 3 for translation and 3 for rotation, being a simple method in computational terms. This approach is typically used for warp images that both input and reference come from the same subjects, e.g. for intermodality registration (i.e. T1w to T2w, etc). Affine registration has more *dofs* than rigid and provides finer results in order to register different subjects. As a linear transformation, whether an image has two parallel lines, after the affine warping, both lines still remain without contact. Finally, the non-rigid registration, often combined with a previous affine transformation, provides the best deformations in terms of similarity between intensity images. However, time complexity of non-rigid algorithm execution raises exponentially, creating a bottleneck issue in the MAS procedure.

Apart from the probabilistic atlas, there exit other methods that reduce the registration time consuming in the MAS methods: the atlas selection. It consists of pre-selecting a sub-set of examples from the atlas dataset that are more similar to the target image. This similarity can be inherent to the image, e.g. intensity levels or histogram, or through metadata, such as age at acquisition, pathology or equivalent age. This reduces time consumption and regularizes the parameter learning, reducing the possibility of overfitting. Alternatively to this strategy, Roy et al. [Roy et al., 2015] avoid nonlinear registration by combining affine registration with sparse non-local approach, leading to a gain in time efficiency.

Current methods in MAS are mostly focused on the label fusion [Rousseau et al., 2011, Coupé et al., 2011, Sabuncu et al., 2010, Warfield et al., 2004, Weisenfeld and Warfield, 2009, Wang et al., 2013b, Liu et al., 2016, Benkarim et al., 2017a, Sanroma et al., 2018]. Sabuncu et al. [Sabuncu et al., 2010] introduce a generative probabilistic model that generalises label fusion methods such as local, semi-local and global weighted fusion algorithms. In [Warfield et al., 2004], Warfield et al. present their approach called simultaneous truth and performance level estimation (STAPLE). Conceived for correcting the manual segmentations carried out by experts, STAPLE provides an estimation of the true segmentation and a parameter of agreement between an expert segmentation and the true segmentation. This method is based on an iterative probabilistic framework, applying the Expectation Maximisation (EM) algorithm maximising its posterior probability. Weisenfeld et al. [Weisenfeld and Warfield, 2009] combine aligned atlases using STAPLE [Warfield et al., 2004].

Moreover, some works are focused on using the atlas set as prior in order to initialise an EM algorithm that aims to find a statistical modelling of intensity tissues, given by the GMM [Xue et al., 2007, Beare et al., 2016, Liu et al., 2016, Cardoso et al., 2013]. Among them, there are several extension such as the inclusion of a Markov Random Field (MRF) step in the EM process in order to be robust to PVE [Xue et al., 2007, Cardoso et al., 2013]. In [Cardoso et al., 2013], Cardoso et al. introduce a regularisation step in EM-MRF scheme that adapts priors. Makropoulos et al. [Makropoulos et al., 2014] add more classes to their modelling in order to separate classes with and without PVE. For those classes with PVE, knowledge-based priors are used for splitting them into the corresponding tissues.

Patch-Based approaches

In [Buades et al., 2005], Buades et al. popularised non-local approaches, publishing an efficient algorithm for image denoising. The idea of the methodology is to restore

each point of an image finding similar points in the whole image and averaging them, contrary to the local denoising method. In order to find the relevant points for each evaluated point, the similarities are computed using a point and its neighborhood, so-called a patch. This adds contextual information that improve the robustness to the noise. Similar patches are weighted according to their degree of similarity, defined by a distance robust to a Gaussian noise. Since then, these strategies have been used to solve other cases of inverse problems. In medical image processing, they have been applied to several domains such as registration [Heinrich et al., 2012], interpolation [Manjón et al., 2010], classification [Tong et al., 2014] or segmentation [Coupé et al., 2010].

Commonly, atlas-based methods use voxel-wise strategies in order to find similarities between atlas and target image. These similarities lead to compute global or local weights in order to estimate linearly the segmentation. However, the accuracy of the estimated segmentation is sensitive to the registration process, which may introduce errors due to the inter-subject variability. In addition, this strategy is vulnerable to image noise, leading to misclassified points. Typically, those effects require a post-processing step in order to reduce the error in segmentation. Introducing non-local approaches to MAS provides a flexibility to registration errors thanks to the local search window and a noise robustness due to the use of patch.

However, the patches usually used have a square shape due to the computational simplicity. Alternatively, there are some other techniques that try to replace this default shape. Supervoxel-based approaches [Achanta et al., 2012, Huo et al., 2018] rely on splitting the image into regions with a criterion of shape and homogeneity, leading to transform the original image into small regions with different shapes. Moreover, in [Deledalle et al., 2012, Faisan et al., 2012] they vary the shape of patch according to their performance in the target image.

Concerning the MRI segmentation, the non-local approaches have been extended to the brain extraction [Dai et al., 2013], tissues segmentation [Rousseau et al., 2011] or segmentation of particular regions of interest [Coupé et al., 2010, Coupé et al., 2011]. Rousseau et al. [Rousseau et al., 2011] perform a non-local approach for brain segmentation. In their algorithm, they find the most similar patches from the atlas set to a given patch from the target image. These similar patches propagate their labels to the target patch and they are averaged. Asman et al. [Asman and Landman, 2012] extend STAPLE to a non-local version. Instead of assigning a global performance parameter per atlas, parameters are estimated for every patch belonging to a neighborhood for every voxel in each atlas.

There are several patch-based approaches widely applied to MAS for the brain MRI in newborn [Liu et al., 2016, Wang et al., 2013a, Wang et al., 2018] and fetus [Benkarim et al., 2019, Benkarim et al., 2017a, Sanroma et al., 2018]. For instance, Liu et al. [Liu et al., 2016] mix conventional MAS that initialise the EM with the patch-based approach, by finding the locations where the registration process is likely wrong. Wang et al. [Wang et al., 2013a] compute weights by optimizing a function that depends on the correlation between a pair of segmentation error probabilities from atlas set. Benkarim et al. [Benkarim et al., 2019] try to avoid registration errors by creating an intermediate template without any label propagation. This leads to avoid unrealistic shapes in atlas segmentations and to gain in terms of computational memory and time consuming.

A label fusion strategy combined with non-local technique may be interpret as a linear regression, as mentioned in [Awate and Whitaker, 2014], where the intensity images are the training set and the segmentation images are testing set. This explains why MAS with patch-based approaches can be inspired by other techniques, such as the

sparse coding [Timofte et al., 2013,Zhang et al., 2019], leading to mixed algorithms [Roy et al., 2015, Liao et al., 2013, Tong et al., 2015]. In this context, other methods in machine learning have been used in order to enhance the linear regression [Hao et al., 2014,Benkarim et al., 2017a,Sanroma et al., 2018]. In [Benkarim et al., 2017a], Benkarim et al. classify each patch from the target image using SVM algorithm. Sanroma et al. [Sanroma et al., 2018] initialize with Joint Label Fusion (JLF) [Wang et al., 2013a] a random forest using a mix of patches from different MRI modalities.

Analysis of label fusion

As mentioned above, the current state-of-the-art of MAS is focused on its third part, i.e. the label fusion. Moreover, some works try to limit or avoid the registration process in order to reduce time consumption and memory resources (i.e. each registration of an example from the atlas set generates three new files). The registration errors propagated to segmentations due to the effect of warping or interpolation are also questioned.

In the sequel, we provide an analysis of the common assumptions in this kind of methods in order to obtain the desired segmentation. We start formalizing the issue and methodology; then we continue giving some examples of existing methods. An analysis concludes this section focusing on an optimization framework that motivated us to implement a new multi-atlas segmentation method based on the notion of patch and the use of an atlas set. This motivation relies on finding an optimal criterion for combining the registered atlas segmentations.

Common hypotheses

Mutli-atlas sets introduce a space prior of structures to be segmented. After the registration of intensity images and propagation to segmentations, all these information have to be combined in order to estimate the target segmentation. This combination requires to assume some hypotheses that are commonly used in MAS methods.

In order to formalize the issue, let $\mathcal{E}$ be the dataset of examples (i.e. the multi-atlas set) defined as:

$$\mathcal{E} = \{E_i = (I_i, S_i), i = 1 \dots n\} \tag{2.1}$$

where it is formed by n examples where each one, E_i, is defined as the subset of one intensity image I_i and its segmentation S_i. Let I be the target image and S its segmentation, which is unknown. The segmentation S can be generally expressed as:

$$S = f(I, E_1, \dots, E_n) \tag{2.2}$$

where f is a function that maps the segmentation S using the input image I and the example dataset $\mathcal{E}$.

At that point, a first approach is to consider the assumption that f can be modelled as a linear operator. This means that the segmentation of the input S is estimated using a linear combination of the n segmentation images from the example set $\mathcal{E}$.

$$S = \sum_{i=1}^{n} w_i S_i \tag{2.3}$$

where w_i is the weight assigned to the example E_i. Intuitively, weights are going to depend on the similarity between the input image and the examples. Since segmentation

of the target image S is unknown, a second assumption is considered: if the target image and intensity example images are similar, their segmentations are likely similar too. This leads to assume that weights used for estimating the segmentation S (Equation (2.3)) can be computed with a distance between each intensity example image and the target image:

$$w_i = g(\|I - I_i\|) \tag{2.4}$$

where g is the distance function between I and I_i predefined by the method.

This general framework considers a global multi-atlas strategy for linear estimation, i.e. every example E_i has a single weight w_i. In practice, this global strategy is not sufficient for obtaining an accurate segmentation because the registration step have errors, making the atlases and the target image not identical. Alternatively, we can consider that some examples will match better than others depending on a local criterion. Given a voxel x belonging to the target space and a voxel y in the example set space, both the weights $w_i(x, y)$ and the estimation of $S(x)$ are expressed as:

$$w_i(x, y) = g\left(\|I(x) - I_i(y))\|\right) \tag{2.5}$$

$$S(x) = \sum_{i=1}^{n} \sum_{y \in \Omega_i} w_i(x, y) S_i(y) \tag{2.6}$$

where Ω_i is the support of the images I_i and S_i.

This strategy considers a local distance that is sensible to registration errors and noise. In order to be robust to them, instead of considering the voxel as comparison unit, some multi-atlas segmentation methods rely on the notion of image patch [Liu et al., 2016, Wang et al., 2013a, Wang et al., 2018, Benkarim et al., 2019, Benkarim et al., 2017a, Sanroma et al., 2018], that is a region within the neighborhood of each point of interest x. The similarity related to x in the images I_i can then be considered with respect to a richer context.

For multi-atlas segmentation purposes, using patches as comparison unit requires to define a distance between x in I and y in I_i. This distance depends on $I(x)$ and $I_i(y)$, but also on the set of values of I and I_i in the neighborhoods $P(x)$ and $P(y)$, respectively. Patches are often defined as isotropic volumes $P(.)$ (squares or cubes of size $2k + 1$) centered on the points of interest.

In the multi-atlas patch-based framework, the weights $w_i(x, y)$ (Equation (2.5)) depend on the information carried by the sub-images restricted to the supports of patches:

$$w_i(x, y) = g\left(\|P_I(x) - P_{I_i}(y))\|\right) \tag{2.7}$$

In other words, the distance considered for the computation of $w_i(x, y)$ involves the set of point-wise distances on the two patches $P_I(x)$ in $P_{I_i}(y)$ in I_i.

This calculus may be costly, depending on the size and number of patches $P(.)$. In order to reduce this computational cost, it is generally chosen to restrict the space of patch research for a given point x of I. We only consider the points y located in the neighborhood $\mathcal{N}(x)$ of x in I_i (of course, a spatial mapping has to be carried out beforehand between I and the images I_i of $\mathcal{E}$; this can be done for instance via a registration step). Then, the segmentation S of I rewrites as:

$$S(x) = \sum_{i=1}^{n} \sum_{y \in \mathcal{N}(x)} w_i(x, y) S_i(y) \tag{2.8}$$

At this point, we will focus on the computation of these weights $w_i(x, y)$.

Existing label fusion methods

As a reminder, multi-atlas methods are composed of three main steps: (1) registration of the learning dataset $\mathcal{E}$ on the input image I, (2) segmentation propagation, and (3) segmentation fusion. In the sequel, we focus on the fusion step (3). In particular, by assuming that segmentation fusion is performed based on Equation (2.10) (with a normalization coefficient used for making the sum of all weights equal to 1, in each x), the discussion mainly deals with the way of computing the weights $w_i(x, y)$. In the next paragraphs, we expose some relevant existing methods in order to compare with our method in the following section.

Non-local means

In the pioneering article [Buades et al., 2005] on Non-Local Means (NLM), the weights considered are calculated according to a Gaussian noise hypothesis. This kind of weights, denoted by w_{NLM}, corresponds to a similarity function inversely proportional to the point-wise intensity distance between the patches, following a normal distribution:

$$w_{NLMi}(x, y) = \exp - \frac{\|P_I(x) - P_{I_i}(y))\|^2}{h^2} \tag{2.9}$$

where h is a regularization constant that can be automatically tuned as $h^2 = 2\sigma^2\beta p$ (p, the size of patches), with usually $\beta = 1$, whereas σ corresponds to the standard deviation of the Gaussian noise in images [Coupé et al., 2008]. By construction, we have $w_{NLMi}(x, y) \in (0, 1]$. Such weighting functions have been used for multi-atlas segmentation purpose [Rousseau et al., 2011, Coupé et al., 2011], where σ is estimated on the input image to segment.

Joint label fusion

The Joint Label Fusion (JLF) method [Wang et al., 2013a] (which was applied in MICCAI 2012 Grand Challenge on Multi-Atlas Labeling and finished at the first place) also relies on image patches. In contrast to NLM, only one patch is selected within the search area $\mathcal{N}(x)$, in order to determine the contribution of an image I_i to the segmentation of I at x. In other words, Equation (2.6) rewrites as:

$$S(x) = \sum_{i=1}^{n} \hat{w}_i(x) S_i(\hat{y}_i) \tag{2.10}$$

where, for each image I_i, $\hat{y}_i$ is the unique point chosen in $\mathcal{N}(x)$ with respect to the similarity between patches $P_I(x)$ and $P_{I_i}(\hat{y}_i)$. Then, we have:

$$\hat{y}_i = \arg \min_{y \in \mathcal{N}(x)} \|P_I(x) - P_{I_i}(y)\| \tag{2.11}$$

Only one weight w_i is then to be computed for each image I_i. Nevertheless, it is defined as spatially variant. In particular, at x, the set $\hat{\mathbf{w}}(x) = \{\hat{w}_i(x), i = 1 \dots n\}$ is defined as the following minimizer:

$$\hat{\mathbf{w}}(x) = \arg \min_{\mathbf{w}(x) \in W} \mathbf{w}(x)^t M_x \mathbf{w}(x) \tag{2.12}$$

where W is the set of vectors $(w_i)_{i=1}^n \in [0,1]^n$ such that $\sum_{i=1}^n w_i = 1$ and M_x is the correlation matrix between the segmentation error probabilities induced by the n images I_i of $\mathcal{E}$ (see [Wang et al., 2013a, Equations (6–12)] for more details).

STAPLE

Considering a collection of segmentation maps, the segmentation fusion step aims at computing a probabilistic estimate of the true segmentation. It appears then that the STAPLE method proposed in [Warfield et al., 2004] can be used for multi-atlas segmentation. The goal of STAPLE is to estimate both the segmentation S, and performance parameters θ describing the agreement over the whole image between the experts (i.e. the set of registered images of $\mathcal{E}$) and S. An iterative optimization approach (i.e. the EM algorithm) is used to estimate S and θ in a probabilistic framework. S is obtained by maximising its posterior probability:

$$\begin{aligned} P(S=s|D,\theta^{(k)}) &= \prod_{x\in\Omega} P(S(x)=s|D,\theta^{(k)}) \\ &= \prod_{x\in\Omega} \frac{P(S(x)=s)\prod_{i=1}^n \theta^{(k)}_{id_{xi}s}}{\sum'_s P(S(x)=s')\prod_{i=1}^n \theta^{(k)}_{id_{xi}s'}} \end{aligned} \tag{2.13}$$

where d_{xi} is the segmentation decision of expert i for the voxel x ($x \in \Omega$, where Ω is the support of the image I to segment) and $\theta^{(k)}_{id_{xi}s}$ is the probability that expert i gives the label s' to a voxel x when the reference standard label is s ($\theta_{id_{xi}s=P(d_{xi}=s'|S=s)}$) at the iteration k. The variable θ corresponds then to the weights w used for the segmentation fusion. In [Asman and Landman, 2012], a non-local version of STAPLE is proposed to add search and patch neighborhoods to compute the weights for segmentation fusion.

MANTIS

By contrast, the Morphologically Adaptive Neonatal Tissue Segmentation (MANTIS) algorithm [Beare et al., 2016] is not relying on multi-atlas set; it is based on classification techniques. Indeed, this latter method relies on an adaptation of the unified segmentation algorithm [Ashburner and Friston, 2005], enriched with morphological processing and topological filtering steps. It was applied to the NeoBrainS12 challenge, an event proposed in MICCAI 2012.

Optimization of patch-weights computation

In summary, MAS methods [Rousseau et al., 2011, Coupé et al., 2011, Wang et al., 2013a] implicitly rely on a linear model and the assumption of isometry, i.e. the weight set of the current voxel x with respect to its neighbors in the learning dataset $\mathcal{E}$ is the same in the intensity space and in the segmentation space. Thanks to these assumptions, the segmentation S of I at x is defined as a (normalized) linear combination of the segmentations, the weights being estimated from the intensity images (Equations (2.6), (2.10)).

Bearing in mind these assumptions, the computation of weights $w_i(x,y)$ can also be seen as an optimization problem. In this section, we focus on this optimization framework.

Optimization based on intensity similarities

Since the intensity images are used to compute the weights that predict the linear segmentation, one can observe that these weights are indeed the parameters for an

estimation of the target image. Given the notion of patch, these parameters are adapted to estimate the original patch.

With this idea in mind, the LLE (Locally Linear Embedding) algorithm [Roweis and Saul, 2000] proposes an optimization framework for dimension reduction purposes. This method relies on the assumption that every point can be represented by a local linear combination of its neighborhood. This combination is learnt and applied *a posteriori* in order to estimate the reduced data, in the same way as our computed weights for obtaining the segmentation estimation.

Inspired by the first part of the LLE algorithm, we can define the energy function for weights computation as:

$$\phi_I(x) = \left\| P_I(x) - \sum_{i=1}^{n} \sum_{y \in \mathcal{N}(x)} w_i(x,y) P_{I_i}(y) \right\| \tag{2.14}$$

that defines the distance between the patch $P_I(x)$ and the linear combination of the patches $P_{I_i}(y)$ in I_i for all the y of $\mathcal{N}(x)$. The weights $\hat{\mathbf{w}}(x) = \{w_i(x,y) \mid y \in \mathcal{N}(x), i = 1 \dots n\}$ can then be computed by minimizing $\phi_I(x)$ as follows:

$$\hat{\mathbf{w}}(x) = \arg\min_{\mathbf{w} \in W} \phi_I(x) \tag{2.15}$$

where W is the set of normalized vectors taking their values in $[0, 1]$. The weights are then estimated such that the reconstruction error of the current image patch P_I using a linear model is minimized.

Following the optimization framework of LLE algorithm, Equation (2.15) can be minimized using Lagrange multipliers. The use of Lagrange multipliers allows the expression to be constrained during the optimization process, in our case $\sum_{i=1}^{n} \sum_{y \in \mathcal{N}(x)} w_i(x,y) = 1$. First, we need the covariance matrix, defined as:

$$C_{y_i y_i'} = (P_I(x) - P_{I_i}(y)) \cdot (P_I(x) - P_{I_i}(y')) \tag{2.16}$$

The analytical expression of Lagrange multiplier is defined as:

$$\mathcal{L}_{P_I(x)} = \frac{1}{2} \sum_{y_i'} (C_{y_i y_i'})^{-1} - \lambda [\sum_{i=1}^{n} \sum_{y \in \mathcal{N}(x)} w_i(x,y) = 1] \tag{2.17}$$

At this point, the optimal weight $\tilde{w}_i(x,y)$ is found by deriving $\mathcal{L}_{P_I(x)}$ and equalizing to zero. Therefore, optimal weight $\tilde{w}_i(x,y)$ becomes:

$$\tilde{w}_i(x,y) = \frac{\sum_{y_i'} (C_{y_i y_i'})^{-1}}{\sum_{y_i} \sum_{y_i'} (C_{y_i y_i'})^{-1}} \tag{2.18}$$

In a practical point of view, the optimization can be done by solving:

$$\frac{1}{Z(x)} \sum_{i=1}^{n} \sum_{y \in \mathcal{N}(x)} (C_{y_i y_i'})^2 w_i(x,y) = 1 \tag{2.19}$$

where $Z(x)$ is the normalization constant for a point x, summing all weights $w_i(x,y)$ for all $y \in \mathcal{N}(x)$ and $i = 1, \dots, n$.

In order to avoid singularity in the covariance matrix, we add an identity matrix multiplied by a small term of regularisation called δ_{reg}. This regularisation parameter is manually assigned.

$$C_y = C_y + \delta_{reg} I \tag{2.20}$$

Optimization based on segmentation similarities

Since the computed weights are then used for segmentation purpose based on Equations (2.6) or (2.10), the previous strategy relies also on an assumption of isometry. Intuitively, the optimal strategy for linearly estimating the segmentation S is to obtain $w_i(x, y)$ directly in the segmentation space. In other words, the best computation for $w_i(x, y)$ using this framework is to introduce S itself as an input with the segmentation images S_i, then avoiding the assumption of isometry. Using the same optimization framework, the new energy function is defined as:

$$\phi_S(x) = \left\| P_S(x) - \sum_{i=1}^{n} \sum_{y \in \mathcal{N}(x)} w_i(x, y) P_{S_i}(y) \right\| \tag{2.21}$$

where $P_S(x)$ is the patch segmentation of S at voxel x. This expression is minimized according to Equation (2.15) as the previous strategy.

This method requires the knowledge of segmentation S of the input image I, which is the goal of the system. Thus this method cannot be compared to the rest of method. Nevertheless, it can be use as a test in order to verify the common hypotheses applied by MAS approaches in the literature. Results in Section 2.4 show that this strategy has the highest DICE score (i.e. close to 1). This ensures the linear modeling as a suitable tool for combining segmentation examples and obtaining a reliable segmentation. However, the assumption of isometry is more disputable, which is discussed in Section 2.5.

Iterative Multi-Atlas Patch-based approach

Introduction to the methodology

The isometry assumption can be relaxed by keeping the way the segmentation is performed from the weights (Equations (2.6) and (2.10)). The principle is to directly compute the weights in the space of segmentations. To this end, it is then necessary to replace, in the definition of $\phi_I(x)$ (Equation (2.14)), the patches P_I and P_{I_i} on images I and I_i by the patches P_S and P_{S_i} on the segmentations S and S_i associated to these images.

The same optimization scheme (Equation (2.15)) can then be used for determining the weights $\hat{\mathbf{w}}(x) = \{w_i(x, y) \mid y \in \mathcal{N}(x), i = 1 \dots n\}$. However, this formulation requires to know beforehand the segmentation S of the target image I. Since S is the segmentation to estimate, we propose to derive an iterative scheme to relax the isometry assumption.

Mixed patches

To this end, we propose to define mixed patches $P_{E_\star}$ from image–segmentation couples $E_\star = (I_\star, S_\star)$. All the considered images $I_\star$ (namely, I and the I_i) are defined on a same support Ω (indeed, the image registration step is performed beforehand), and they take their values within an interval $V \subset \mathbb{R}$. The associated segmentations $S_\star$ are defined on the same support Ω, but they take their values in $[0, 1]$. Without loss of generality, we consider that V has been normalized. Under these assumptions, both the $I_\star$ and the $S_\star$ can be expressed as functions $\Omega \to [0, 1]$ (with, however, distinct semantics). This normalization is crucial for defining a non-biased inter-patch distance.

Practically, for an image–segmentation couple $E_\star = (I_\star, S_\star)$, the space of associated patches $E_\star$ is a function:

$$\left| \begin{array}{rccl} P_{E_\star} & : & \Omega & \to & [0,1]^p \times [0,1]^p \\ & & x & \mapsto & (P_{I_\star}(x), P_{S_\star}(x)) \end{array} \right. \tag{2.22}$$

where $P_{I_\star}(x)$ and $P_{S_\star}(x)$ are the usual patches of image and segmentation, respectively, that are vectors of $[0,1]^p$, that indicate the values of $I_\star$ and $S_\star$ inside a window $\mathcal{N}(x)$ of Ω of size p, locally centred on x. (For the sake of concision, we will equivalently consider $P_{E_\star}(x)$ as a vector $(p^k_{E_\star}(x))_{k=1}^{2p}$ of $[0,1]^{2p}$ instead of a couple of vectors of size p.)

Inter-patch distance and energy function

In order to define the inter-patch distance, the L_k norms (and especially L_1 and L_2) can be considered:

$$\|P_{E_\alpha}(x) - P_{E_\beta}(x)\|_1 = \sum_{k=1}^{2p} |p^k_{E_\alpha}(x) - p^k_{E_\beta}(x)| \tag{2.23}$$

$$\|P_{E_\alpha}(x) - P_{E_\beta}(x)\|_2 = \Big(\sum_{k=1}^{2p} \big(p^k_{E_\alpha}(x) - p^k_{E_\beta}(x)\big)^2 \Big)^{\frac{1}{2}} \tag{2.24}$$

In particular, it is possible to define, in a way similar to Equation (2.14), an energy function ϕ_E which, given a image–segmentation couple $E = (I, S)$ and a multi-atlas set $\mathcal{E} = \{E_i = (I_i, S_i), i = 1 \dots n\}$, expresses the distance between E and a linear combination on $\mathcal{E}$ at a point x of Ω:

$$\phi_E(x) = \Big\| P_E(x) - \sum_{i=1}^{n} \sum_{y \in \mathcal{N}(x)} w_i(x,y) P_{E_i}(y) \Big\| \tag{2.25}$$

As in Equation (2.15), our purpose is to minimize the function $\phi_E(x)$ in order to obtain a vector of optimal weights for computing the segmentation S of I at every voxel x:

$$\hat{\mathbf{w}}(x) = \arg\min_{\mathbf{w} \in W} \phi_E(x) \tag{2.26}$$

with the same notations as in Section 2.2.3. This criterion can be optimized efficiently in the same way as the one of Equation (2.15).

In order to relax the isometry assumption, the computation of the weights $w_i(x,y)$ is based on proximity between patches in the image space, and proximity in the segmentation space. Since the segmentation of the target image is not known, an iterative method is used (Algorithm 1). The successive steps are discussed hereafter.

Initialization

Since there is no estimation of the target segmentation in initial state, the first iteration of the process requires to define beforehand an initial image–segmentation couple $E^{(0)} = (I, S^{(0)})$ associated to I. The initial segmentation $S^{(0)}$ can be chosen arbitrarily (e.g. randomly or null). This initialization is justified hereafter, in the weighting policy description (Section 2.3.4).

Algorithm 1 Iterative Multi-Atlas Patch-Based approach

Require: I: input image,
$\mathcal{E} = \{E_i = (I_i, S_i), i = 1 \dots n\}$: learning dataset,
N: number of iterations, $\{\alpha_0 = 0, \alpha_1, \dots, \alpha_{N-1}\}$: intensity *vs* segmentation trade-off,
$S^{(0)}$: arbitrarily chosen initial segmentation
Ensure: S: segmentation of I
for $j = 1 \dots N$ **do**
  for all $x \in \Omega$ **do**
    Compute $\hat{\mathbf{w}}^{(j)}(x)$ (Equation (2.27))
    Compute $S^{(j)}(x)$ from $\hat{\mathbf{w}}^{(j)}(x)$ (Equation (2.28))
  end for
end for
$S \leftarrow S^{(N)}$

Iterations

During the iterative process, the current energy function $\phi_E^{(j+1)}(x)$ is optimized by considering $P_E^{(j)}(x) = (P_I(x), P_{S^{(j)}}(x))$, in order to define the weights $w_i^{(j+1)}(x, y)$ (Equations (2.25–2.26)):

$$\hat{\mathbf{w}}^{(j+1)}(x) = \arg\min_{\mathbf{w} \in W} \left\| P_E^{(j)}(x) - \sum_{i=1}^{n} \sum_{y \in \mathcal{N}(x)} w_i(x, y) P_{E_i}(y) \right\| \tag{2.27}$$

and then to compute $S^{(j+1)}$ from these weights $w_i^{(j+1)}(x, y)$ of $\hat{\mathbf{w}}^{(j+1)}(x)$:

$$S^{(j+1)}(x) = \sum_{i=1}^{n} \sum_{y \in \mathcal{N}(x)} w_i^{(j+1)}(x, y) S_i(y) \tag{2.28}$$

Weighting

We propose to balance the influence of the terms related to intensity and estimated segmentation, respectively. Here, the underlying idea is to relax progressively the hypothesis of isometry between intensity space and segmentation space. In particular, at each iteration j, we consider a parameter $\alpha_j \in [0, 1]$ such that the terms of $P_{E_\star}$ linked to the patch $P_{S_\star}$ (resp. $P_{I_\star}$) are weighted by α_j (resp. $1 - \alpha_j$).

Practically, this weighting can be performed without altering the formulation of Equations (2.26–2.28). Indeed, it is sufficient that the α_j weights be involved in the definition of $P_{E_\star}$ by applying a scale function onto the value space. In other words, we define a function:

$$\left| \begin{array}{rccc} \Pi_\alpha & : & [0,1]^p \times [0,1]^p & \rightarrow & \mathbb{R}^p \times \mathbb{R}^p \\ & & (P_{I_\star}, P_{S_\star}) & \mapsto & ((1-\alpha)P_{I_\star}, \alpha P_{S_\star}) \end{array} \right. \tag{2.29}$$

It is then sufficient to substitute $\Pi_{\alpha_j} \circ P_{E_\star}$ to $P_{E_\star}$ in the above optimization scheme. In order to guarantee a continuous evolution of the process, we choose an increasing sequence of weights (α_j) depending on j. At the first iteration, α_0 is set to 0. Then any initialization of the segmentation $S^{(0)}$ can be considered.

Experiments

In this section, we present the experiments in two parts. First part relies on an analysis of patch fusion in order to evaluate the isometric assumption. Then, we apply the proposed method for processing 3D neonatal brain MR images. In this work, we focus on the segmentation of cerebral cortex, by taking advantage of a dataset of similar images, endowed with associated segmentation maps.

Data

The considered images are T2-weighted MRI data, made available [Hughes et al., 2017] in the context of the Developing Human Connectome Project (dHCP)[2] [Makropoulos et al., 2018]. Infants were recruited and imaged at the Evelina Neonatal Imaging Centre, London. Informed parental consent was obtained for imaging and data release, and the study was approved by the UK Health Research Authority. All infants were born and imaged at term age (37–44 weeks of age). Imaging was carried out on 3T Philips Achieva using a dedicated neonatal imaging system which included a neonatal 32 channel phased array head coil. The infants were imaged in natural sleep. T2w images were acquired in sagittal and axial slice stacks with in-plane resolution 0.8×0.8 mm^2 and 1.6 mm slices overlapped by 0.8 mm. Other parameters were: $12,000$/156ms TR/TE, SENSE factor 2.11 (axial) and 2.58 (sagittal). In this work, a set of 40 images with a voxel size of $0.5 \times 0.5 \times 0.5$ mm^3 is considered. Among these data, 30 are used for building the learning dataset $\mathcal{E}$, whereas the other 10 are used as testing dataset. For each of these 40 images, the algorithmic pipeline dHCP[3] has been applied. The obtained segmentations, visually validated, are used as reference.

Patch fusion analysis

In order to visualize the effectiveness of the assumption of isometry, we define an experiment focused on relations between optimal weights (presented in Section 2.2.3) trained in intensity space (Equation (2.14)) and in segmentation space (Equation (2.21)).

To do so, we compute and evaluate both weights using two types of plots. First, we plot, for each patch, weights of a patch trained with intensity space and with segmentation space, leading to a graphical relation between relevant weights in each space. Then, the relation between patch similarity and difference of both weights are calculated. If the assumption of isometry is confirmed, we expect to obtain a linear relation in both cases: a line for the first type and a centered triangular-shape for the second plot.

For these experiments, we have selected randomly an example from the atlas dataset (presented above). We have computed weights centered on four arbitrary voxels. These tests do not require an atlas; indeed trained patches come from the neighborhood (delimited by a search area) in order to predict the centered patch. Parameters are the same as the ones used for performing the comparison methods (presented in next paragraphs): the size of patches is $3 \times 3 \times 3$ voxels and the search areas $\mathcal{N}(.)$ are cubes of $7 \times 7 \times 7$ voxels. Experiments are presented in Figure 2.1 and discussed in Section 2.5.1.

[2] `http://www.developingconnectome.org`
[3] `https://github.com/DevelopingHCP/structural-pipeline`

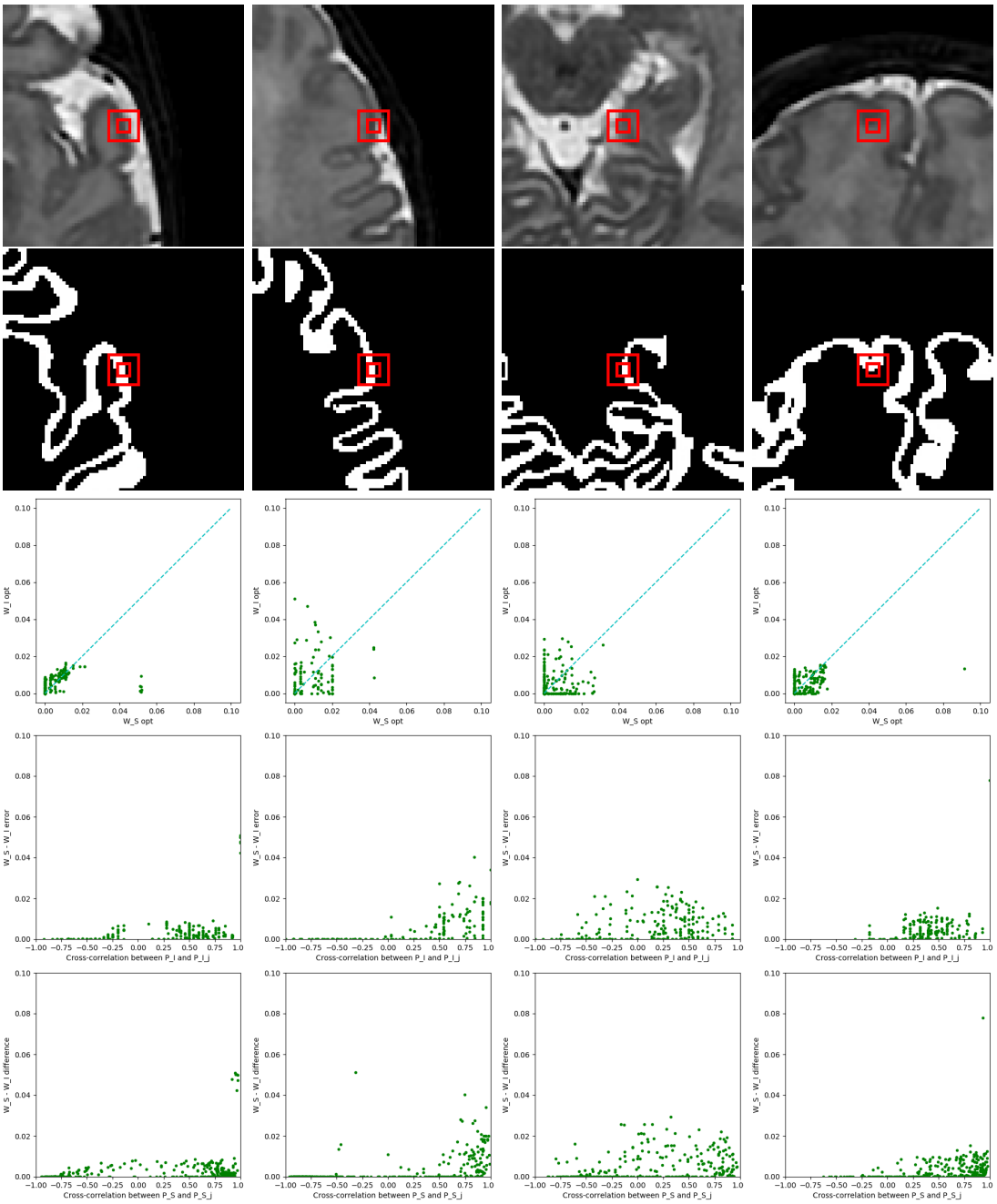

Figure 2.1 – Analysis of weights computed following Equations (2.14) and (2.21) in four different patches. Each column corresponds to a specific patch. In rows: (1) intensity image, (2) segmentation image, (3) diagram with intensity-based weights in y-axis and segmentation-based weights in x-axis, (4) diagram with absolute difference between neighbor patch and centered intensity patch in y-axis and neighbors cross-correlation between in x-axis and (5) idem plot of previous one changing the y-axis by segmentation patches.

Test of new approach

Data preprocessing

The example images were registered in two steps (affine, then non-rigid registration) by using ANTs[4] [Avants et al., 2008]. To improve the robustness with respect to intensity variability, the intensities of example images (I_i) were normalized by histogram matching with the subjects to be segmented (I), using ITK[5]. This is done in order to avoid additive bias effects on inter-patch distances (Equations (2.23)–(2.24)).

Comparison of methods

The proposed method, described in Section 2.3, and denoted by IMAPA (IMAPA stands for "Iterative Multi-Atlas Patch-based Approach" in the sequel, was compared to the following methods:

- Non-Local Means – NLM (Section 2.2.2.1);
- Joint Label Fusion – JLF [Wang et al., 2013a] (Section 2.2.2.2);
- MANTIS [Beare et al., 2016].

As a reminder, the first two methods are patch-based multi-atlas methods, such as IMAPA. By contrast, MANTIS is not multi-atlas; it is based on classification techniques as we explain in Section 2.2.2.4.

Parameters

The MANTIS method presents few parameters. These are regularisation parameters for the initial classification of the unified segmentation [Ashburner and Friston, 2005]. The used values are those defined by default.

The three other methods based on patches all present similar characteristics. In particular, they share various parameters: the number K of nearest patches considered for the calculus of energy functions $\phi(.)$ (Equation (2.14) and next); the size p of the patches $P(.)$; and the size of research areas $\mathcal{N}(.)$.

The use of the K nearest patches (among $n.|\mathcal{N}(x)|$) for the calculus of $\phi(x)$ is aimed to reduce the influence of an excessive amount of patches with a low similarity with the considered patch in each point $x \in \Omega$. The parameter K is set to 15, except for JLF where, by definition, we have $K = n$ (here, 30). The value of p is set to 27; it corresponds to patches of size $3 \times 3 \times 3$ voxels. The search areas $\mathcal{N}(.)$ are cubes of $7 \times 7 \times 7$ voxels. These parameters were set based on preliminary experiments.

Some parameters are specific to some of these methods. In JLF, the supplementary parameters were set at a fixed default value. For the IMAPA method, the inter-patch distance relies on the L_2 norm (Equation (2.24)). The regularization parameter for inversion δ_{reg} is set to 10^{-3}. The number of iterations N was empirically set to 2. The values of α_j (trade-off coefficient) are set to 0 and 0.25 for the first and second iteration, respectively. The 0 value allows us to perform a first iteration based on data-fidelity only. The 0.25 value for the second iteration was determined from preliminary experiments, within a range of values from 10^{-2} to 0.5. The convergence of the algorithm has been assessed by computing the fuzzy DICE index for each value of $\alpha = \{0; 0.25; 0.5; 0.75; 1\}$.

[4] `http://stnava.github.io/ANTs`
[5] `https://itk.org/`

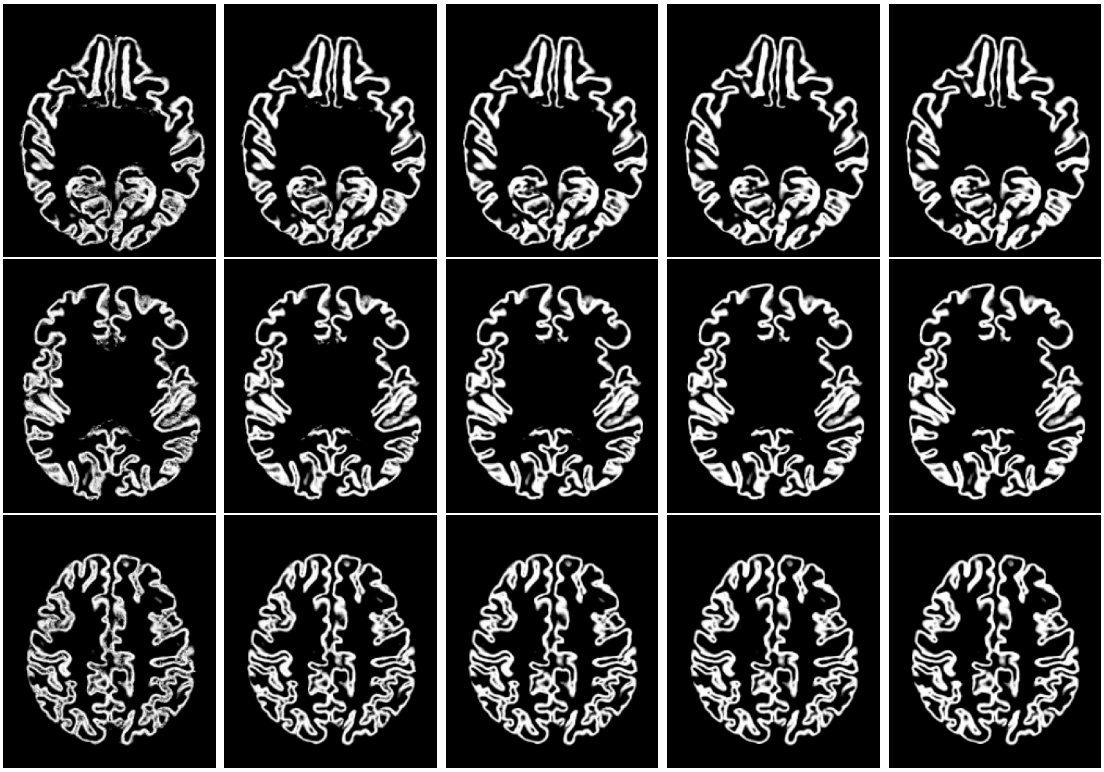

(a) $\alpha = 0$ (b) $\alpha = 0.25$ (c) $\alpha = 0.5$ (d) $\alpha = 0.75$ (e) $\alpha = 1$

Figure 2.2 – Slices of output segmentation maps of the same subject through the iterative process (i.e. $\alpha \in \{0; 0.25; 0.5; 0.75; 1\}$).

Although the fuzzy DICE index increases over iterations, the first two iterations (from $\alpha = 0$ to 0.25) led to the main improvement. Figure 2.2 shows estimated segmentation maps through the iterative process for one subject. To reduce the computation time, we have used in this work only two iterations (i.e. $\alpha \in \{0; 0.25\}$). The K nearest neighbors are updated at each iteration. This allows us to combine examples that are increasingly adapted to estimate the segmentation, according to the evolution of α_j.

Computing time

Experiments were carried out in a computer with a processor Intel Xeon(R), with 16 cores at 3 GHz and 32 GB of RAM. The registration step took 45 minutes per image and histogram matching only a few seconds. For methods, computation times are the following: NLM [Buades et al., 2005]: 10 minutes, JLF [Wang et al., 2013a]: 2 minutes, MANTIS [Beare et al., 2016]: 1 minutes, and IMAPA: 45 minutes.

Results

Quantitative evaluations of the results provided by the four methods are gathered in Table 2.1. In particular, two evaluation measures were considered: the Dice index and the Peak Signal to Noise Ratio (PSNR). The Dice index (that varies between 0 and 1) is an overlapping measure between the estimated segmentation and the ground-truth; the closer to 1, the better the adequacy between the result and the ground-truth both in terms of false positives and false negatives. The PSNR provides another complementary

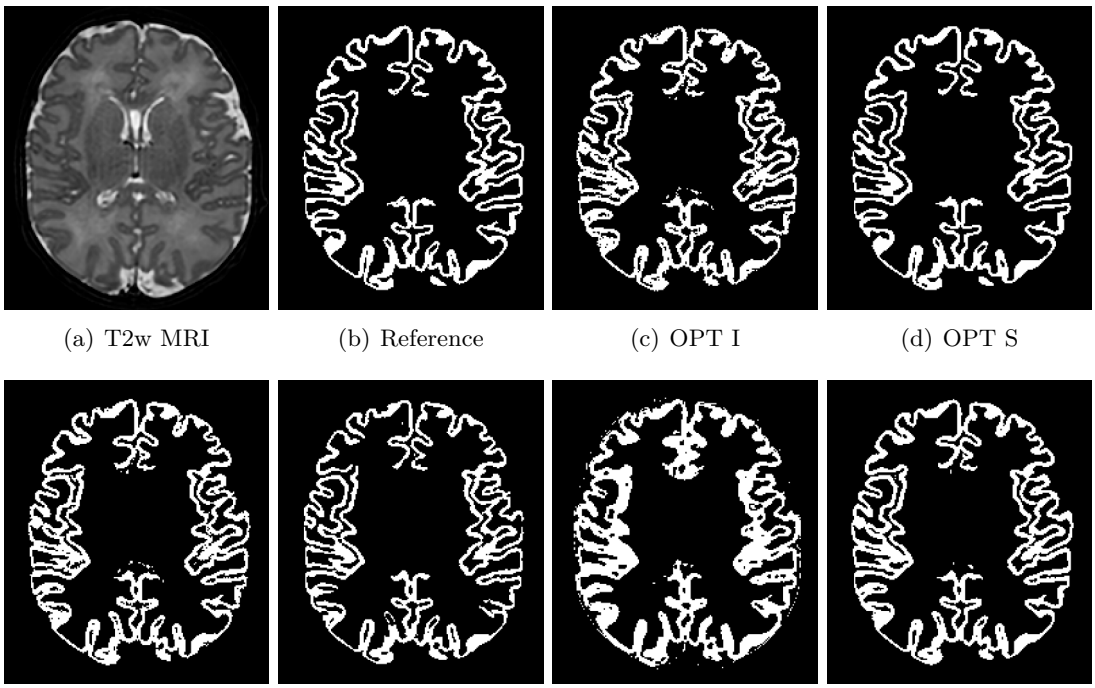

(a) T2w MRI (b) Reference (c) OPT I (d) OPT S

(e) NLM (f) JLF (g) MANTIS (h) IMAPA

Figure 2.3 – Segmentation results on a T2-weighted brain MRI (axial slice). (a) Input image. (b) Reference segmentation obtained from the dHCP pipeline [Schuh et al., 2017]. Segmentation results obtained with: (c) Optimization in intensity space, (d) Optimization in segmentation space, (c) NLM, (d) JLF [Wang et al., 2013a], (e) MANTIS [Beare et al., 2016], (f) IMAPA.

measure of quality (mean quadratic error) of the estimated image; the higher its value (in dB), the better the quality of the obtained result. The PSNR is computed as follows:

$$PSNR = 10 \log_{10} \left(\frac{MAX^2}{MSE} \right) \tag{2.30}$$

where MAX is the maximum value of the reference image and MSE is the mean squared error (between the estimated image and the reference image).

The IMAPA and NLM methods generate results defined as fuzzy maps. In order to compare these results with those of JLF and MANTIS (that generate binary maps), a thresholding of the fuzzy maps is set at value 0.5.

A more qualitative assessment of the results obtained by the four methods is also available via illustrative samples of segmentations, visualized on 2D slices, in Figures 2.3–2.4 (axial slices), and as 3D visualizations of meshed obtained from binary volumes (sagittal view) in Figure 2.5 and using meshing tools from BrainVISA software[6] [Geffroy et al., 2011].

[6] `http://brainvisa.info`

Table 2.1 – Performances of IMAPA, compared to three other segmentation methods (NLM, JLF [Wang et al., 2013a], MANTIS [Beare et al., 2016]) applied on 10 subjects, with a learning dataset of 30 subjects. Best results are highlighted in bold. In addition, we include the optimal weights computed in different spaces. Note that OPT I corresponds to the first iteration of IMAPA (with $\alpha = 0$) and OPT S is not a real method of segmentation: it fulfills its function in evaluating the linear model hypothesis.

	NLM	JLF	MANTIS	OPT I	IMAPA	OPT S
Dice (mean)	0.876	0.845	0.793	0.878	**0.887**	0.987
Dice (std. dev.)	**0.011**	0.018	0.028	**0.011**	**0.011**	0.003
PSNR (mean, dB)	20.758	18.966	16.661	20.815	**21.086**	26.383
PSNR (std. dev., dB)	0.396	0.487	0.533	0.384	**0.392**	0.466

Discussion

Evaluation of hypotheses

In order to evaluate the adjustability of the linear modelling to the multi-atlas patch-based segmentation, we compute weights in the segmentation space. We use patches coming from the segmentation atlas set using the segmentation reference, i.e. the result is used as the input. With this action, we can compute the best weights that the linear modelling can provide. The evaluation of 10 subjects (Table 2.1) reveals a mean of DICE score almost equal to 1. This result ensures the linear combination as a good estimator for our issue.

On the other hand, the second common assumption is the isometry between segmentation space and intensity space, i.e. similarities between intensity images are proportional to segmentation images. This allows us to compute weights in the intensity space in order to linearly estimate the segmentation. Experiments applied in randomly selected points into cortex edges (Figure 2.1) aim to compare optimal weights training in intensity space and segmentation space. In third row of the figure, there is not a linear relation between weights. Moreover, focusing on the cross-correlation between patches and example patches, and the difference between two weights (two last rows of the figure), we can expect to find a relation between them. There is not a clear evidence of linearity; thus we can conclude that the assumption of isometry is not strong enough. Therefore, this ensures the need of introducing the segmentation space in the segmentation process.

Finally, we want to highlight the variance of two optimal weights in Figure 2.1, row 3. There are just a few patches that are high weighted, considered as “good examples”; the others, “bad example”, have the opposite properties: numerous and low weighted. If the number of bad examples is too high, although their weights are close to zero, they can introduce a bias on the result. This motivates the use of methods such as KNN that try to regularize the number of bad examples.

Comparison of methods

From a quantitative point of view (Table 2.1), the results obtained with the proposed IMAPA method are better than those obtained with the other three tested methods, for both Dice and PSNR measures. This improvement is significant compared to the JLF

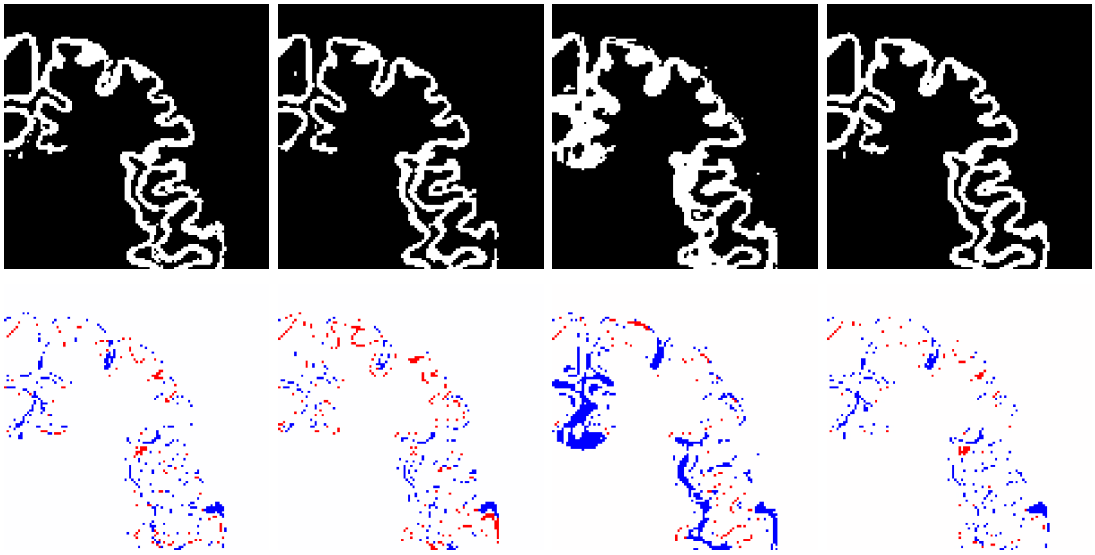

(a) NLM (b) JLF (c) MANTIS (d) IMAPA

Figure 2.4 – First row: zoom on a region of Figure 2.3. Second row: false positives (in blue) and false negatives (in red) provided by the different methods, compared to the reference image (Figure 2.3(b)). (a) NLM, (b) JLF [Wang et al., 2013a], (c) MANTIS [Beare et al., 2016], (d) IMAPA.

and MANTIS methods; it is lower compared to the NLM method (approximately 0.01 gap for Dice and 0.3 dB for PSNR). These results on the dHCP dataset tend to show that the proposed strategy of coupling patch-based and iterative optimization is indeed of interest, as the results are at the level of the state of the art. In addition to this algorithmic approach, the simultaneous use of a data-fidelity term and a regularization term from both the example images and their segmentations in same patches, also seems relevant. Indeed, compared to IMAPA, the NLM weight computation method, although being also patch-based, is neither iterative nor image/segmentation mixing.

Despite slight quantitative differences between IMAPA and the other methods, observation of the visual results confirms the satisfactory behaviour of the IMAPA method from a more qualitative point of view. First, this can be seen on 2D slices in Figures 2.3–2.4. In Figure 2.3, one can observe that MANTIS clearly over-segments the cerebral cortex, compared to the other three methods, while JLF tends to slightly under-segment it. IMAPA and NLM provide visually comparable results, with slightly more noisy results for NLM. These trends are confirmed by Figure 2.4, where we can focus on a zoomed area of the slice, and observe the zones of false positives and false negatives. This illustration emphasizes the over- and under-segmentation behaviours of MANTIS and JLF, respectively. Once again, NLM and IMAPA provide close results, but IMAPA seems to present lower false negatives.

Secondly, the behaviour of the four methods can be qualitatively observed from 3D cortical surfaces computed based on segmentation results. Indeed, in Figure 2.5, one can observe that JLF leads to topologically incorrect surfaces (holes), due to under-segmentation, whereas the over-segmentation of MANTIS leads to noisy patterns on the surface, and disconnected elements. Once again, NLM and IMAPA provide globally correct surfaces (i.e. less isolated small regions, discontinuities and tunnels), with a slightly more regular appearance with IMAPA.

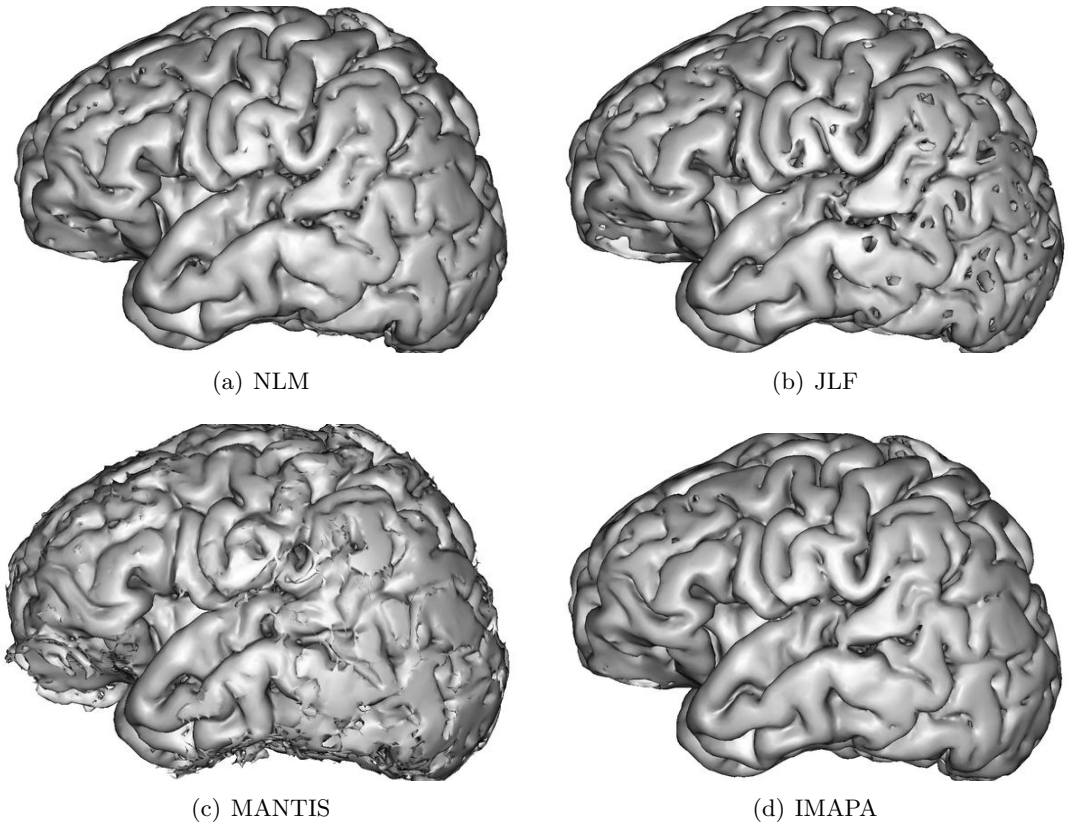

(a) NLM (b) JLF

(c) MANTIS (d) IMAPA

Figure 2.5 – 3D visualization of mesh surfaces computed from the segmentation results obtained with (a) NLM, (b) JLF [Wang et al., 2013a], (c) MANTIS [Beare et al., 2016], (d) IMAPA.

Overall, these experiments argue in favour of considering mixed patches and iterative optimization schemes for patch-based segmentation approaches. This is, in particular, strengthened by the fact that these results were obtained in a complicated applicative context, namely the analysis of cortical surface.

However, these results are yet preliminary. At this stage, they cover a small data set of 40 images. In addition, these data present good contrast quality and signal-to-noise ratio. Consequently, further work will focus on the assessment of the robustness of IMAPA in more challenging contexts, with data of lower quality. In addition, since the method is based on a multi-atlas paradigm, it may be relevant to investigate the impact of example quality, in order to understand the side effects of imperfect segmentation examples, but also heterogeneous data collected in multi-centric studies.

The space of parameters of the IMAPA method has not been fully explored. In particular, the type of distance, the number of closest neighbors, the weighting policies will deserve a wider study. In addition, we have to consider a larger ranges of iterations, in order to observe if smooth evolutions of the trade-off parameter α could enable to improve the overall quality of the segmentation results.

It has also to be mentioned that IMAPA shares similarities with sparse coding-based methods, such as the one described in [Liao et al., 2013, Tong et al., 2015]. More specifically, the representation of the input patch as a linear combination of a set of atoms (called a dictionary in sparse coding) is close to non-local patch-based linear modeling.

Main differences between sparse coding-based methods and the framework used here are: 1) data representation (dictionaries vs. raw patches), 2) sparsity (via a penalty term vs. nearest neighbors in patch space). The estimation of the weights through a reconstruction term brings sparsity-based and non-local approaches closer. The iterative nature of the proposed method is also related to cascading approaches [Viola and Jones, 2001] (also called auto-context [Tu and Bai, 2010]) that make use of previous estimations to refine the segmentation maps. It has to be noticed that the probabilistic framework used in STAPLE is also related to this cascading approach by the alternation between the estimation of weights and the segmentation map during the EM optimization. Future research directions could focus on these methodological aspects to further study the link between IMAPA and sparse coding based methods, cascading frameworks and the STAPLE probabilistic modelling, and to propose a unified framework highlighting the key components of these approaches.

Chapter 3

Application of Segmentation Pipelines on Clinical Datasets

Introduction

In Chapter 2, we have been shown that it is possible to segment the cortex from neonatal MR images with a satisfactory accuracy (with a Dice mean score closes to 89%) in spite of the difficulties discussed in Chapter 1. This accuracy was obtained using a MRI dataset with positive properties for the segmentation such as isotropic high-resolution, low noisy and high contrasted. Nevertheless, 3D neonatal MR images acquired in clinical environments are low-resolution, anisotropic images, making segmentation a challenging task. There is a need in preprocessing and postprocessing steps that add robustness to the segmentation method used; in our case, multi-atlas approaches. All steps together build a set of blocks that is commonly called as pipeline.

Hereafter, we first analyse analyze the main differences between real datasets used in research and in clinical contexts. In addition, we present a brief literature of pipelines for brain segmentation purposes in order to introduce the needs for a specific pipeline adapted to conditions of clinical neonatal datasets.

Clinical datasets

As explained above, we classify the neonatal brain MRI datasets according to their aim. On the one hand, we call research datasets those that are focused on the quality of

Table 3.1 – Details of neonatal and fetal datasets used for testing and validating brain segmentation. Information introduced here is the reference where it was presented, the gestational age of subjects at acquisition, MR image modality, number of available ground truths / segmentation references and the voxel resolution in mm^3.

Paper	GA at MRI (in weeks)	Modality	Number of ref. seg.	Resolution (in mm^3)
Research dataset				
[Xue et al., 2007]	27–45	T1w–T2w	25	0.86 × 0.86 × 2.0
[Leroy et al., 2011]	44–56	T2w	11	1.04 × 1.04 × 2.0
[Gui et al., 2012]	38–44	T1w–T2w	10	0.8 × 0.8 × 1.2
[Makropoulos et al., 2014]	36–44	T1w	20	0.82 × 0.82 × 0.8
	36–44	T2w	20	0.86 × 0.86 × 1.0
[Wang et al., 2014]	39.8–43.2	T2w	20	1.25 × 1.25 × 1.95
	41.5–44.7	T2w	8	1.25 × 1.25 × 1.95
[Liu et al., 2016]	27.3–46.4	T1w	32	1.04 × 1.04 × 1.0
[Beare et al., 2016]	27–41	T2w	36	1.0 × 1.0 × 1.0
[Makropoulos et al., 2018]	37–44	T1w–T2w	40	0.8 × 0.8 × 0.8
[Sanroma et al., 2018]	26–29.3	T1w–T2w	32	0.5 × 0.5 × 2.5
Clinical dataset				
[Song et al., 2007]	40	T2w	10	0.35 × 0.35 × 3.0
[Weisenfeld and Warfield, 2009]	42	T1w	13	0.70 × 0.70 × 1.5
	42	T2w	13	0.86 × 0.86 × 2.0
[Igum et al., 2015]	40	T2w	7	0.35 × 0.35 × 2.0
	40	T2w	5	0.35 × 0.35 × 1.2
	30	T2w	7	0.34 × 0.34 × 2.0
IMAPA (Sec. 2.3)	40	T1w	2	0.27 × 0.27 × 1.2
	40	T2w	-	0.45 × 0.45 × 3.0

the image and geared towards research studies. On the other hand, clinical datasets are those that are acquired with a quality that is sufficient to provide a diagnosis interpreted by a clinical expert.

In Table 3.1 we present some features of different datasets used in the multi-atlas segmentation (MAS) literature. The most relevant feature is the resolution, which is approximately isotropic for research datasets and strongly anisotropic in clinical datasets. Anisotropic resolution makes the application of image processing techniques more difficult, in particular segmentation.

To deal with this issue, additional acquisitions are usually performed on the same subject [Makropoulos et al., 2017, Sanroma et al., 2018, Leroy et al., 2011]. The combination of them leads to a 3D reconstruction [Kuklisova-Murgasova et al., 2012, Rousseau et al., 2006], enhancing the voxel spacing. Some other methods reject or repeat acquisitions that have motion artifacts [Gui et al., 2012, Beare et al., 2016], achieving the best conditions for the image set.

However, these kinds of practice are not well adapt to the clinical environments, where the time acquisition is prioritized against the quality of the MR image in order to find diagnosis. Therefore, some methods use classical interpolation techniques without additional acquisitions for attempting an isotropic resolution [Xue et al., 2007]. The problem of interpolation is that blurry the image, avoiding inter-slice details.

Moreover, another issue to take into consideration is the number of available segmentation references as a consequence of manual expert segmentations. In average, there are a lower number of references in clinical than in research datasets. This fact hampers

the creation of specific approaches for this latter family of images due to the absence of validation.

Another common preprocessing technique is the skull skipping [Xue et al., 2007,Leroy et al., 2011]. The integration of this step is standardized in the brain tissue segmentation for avoiding misclassified errors. The most popular methods are BET [Smith, 2002], a general skull skipping algorithm, or iBEAT [Dai et al., 2013], a specific tool for infant MR images. Both methods are based on deformable models.

Pipeline for cortical segmentation

In the literature, several pipelines are presented that compute the cortex segmentation [Schirner et al., 2015,Daducci et al., 2012,Wright et al., 2015,Tustison et al., 2014]. The authors of [Schirner et al., 2015,Daducci et al., 2012] combined several MRI modalities in order to obtain the map connectome [Daducci et al., 2012] or a synthetic brain model of a human subject [Schirner et al., 2015], where the cortex segmentation is needed. In [Tustison et al., 2014], Tustison et al. used existing tools coming from ANTs[1] and FreeSurfer[2] in order to provide the cortical thickness, segmenting the cortex first. Whereas the previous methods use the segmentation as an intermediate step, Wright et al. [Wright et al., 2015] introduce a semi-automatic pipeline focused on cortical segmentation using T1w images. This pipeline relies on the combination of the watershed algorithm with a threshold level-set.

For neonatal purpose, there is only one remarkable pipeline dedicated to cortical segmentation [Makropoulos et al., 2018]. Even though Makropoulos et al. designed this pipeline for an enhanced mesh generation, the segmentation step still has an important role in the procedure. They use their own multi-atlas method, DrawEM [Makropoulos et al., 2014], with some preprocessing and post-processing steps that only use the T2w images. Then, T1w images are introduced in order to refine the sulcus and gyrus depth to obtain the mesh generation.

However, there is no pipeline available that deals with anisotropic voxel spacing in clinical neonatal MR images. To this end, we evaluate a pipeline mainly consisting of two parts: an upsampling step and a segmentation step. Therefore, the pipeline will segment the target MR image independently of its resolution.

The first step of such a pipeline is the upsampling of the clinical low-resolution (LR) data to $1 \times 1 \times 1$ mm or $0.5 \times 0.5 \times 0.5$ mm. This upsampling step is usually performed using interpolation techniques, leading to blurry edges and loss of details. Single image Super-Resolution (SR) [Greenspan, 2009], whose purpose is to estimate a high-resolution (HR) image from one LR image, constitutes a promising alternative approach [Pham et al., 2017a,Pham et al., 2017b,Rousseau, 2008,Manjón et al., 2010]. However, SR is a challenging inverse problem. In particular the estimation of texture and details remains difficult and SR techniques are not yet applied routinely on clinical data. Indeed, the impact of SR reconstruction on morphometry analysis needs to be accurately investigated.

The second major step is image segmentation. As mentioned in previous chapters, the segmentation of neonatal brain MRI analysis is challenging task due to multiple factors such as the partial volume effect in cortical surface or maturation of the white matter, etc. Various approaches were investigated for neonatal brain data, such as mathematical morphology [Gui et al., 2012], deformable models [Leroy et al., 2011],

[1] `http://stnava.github.io/ANTs`
[2] `https://surfer.nmr.mgh.harvard.edu/`

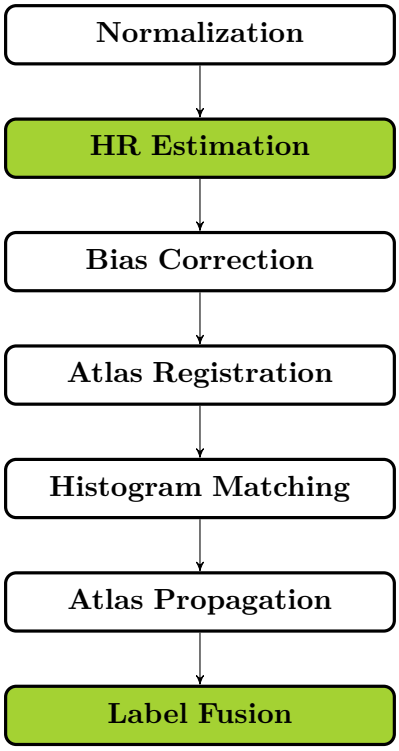

Figure 3.1 – A flowchart of the overall pipeline proposed.

statistical classification [Beare et al., 2016] and multi-atlas methods [Makropoulos et al., 2014]. However, most of these techniques were only evaluated on HR images, typically with slice thickness lower than 1 mm. There is a clear need to evaluate state-of-the-art segmentation algorithms in actual clinical settings. NeoBrainS12 challenge was a first step toward such an evaluation [Igum et al., 2015].

The purpose of these steps is to assess the influence of various upsampling techniques on segmentation map estimation and the robustness of several segmentation pipelines, with a focus on cortical structures. In particular, our aim is to carry out such a study on real neonatal brain MRI data, acquired in a clinical context.

Section 3.2 presents the general approach of a LR neonatal cortex segmentation. We describe three upsampling approaches and four segmentation methods. Our experimental, comparative study is then proposed in Section 3.3, where we evaluate both qualitatively and quantitatively the 12 combinations of SR and segmentation techniques. In Section 3.4, we propose a discussion of these results, leading to concluding remarks on future work in Section 3.5.

Low-Resolution Neonatal Cortex Segmentation Pipeline

In this chapter, we consider multi-atlas segmentation pipelines for clinical LR images consisting of the following steps: image upsampling (Section 3.2.1), bias correction using N4 [Tustison et al., 2010], nonlinear registration of atlases on the input HR image using ANTs [Avants et al., 2008], intensity normalization using histogram matching techniques and image segmentation (Section 3.2.2). In this study, we focus more accurately on two steps: HR estimation and image segmentation. The structure of this pipeline is shown in Figure 3.1.

HR Image Estimation

The resolution of clinical images is generally too low to carry out accurate cortical morphometry studies. Upsampling (to isotropic resolution of $1\times1\times1$ mm or $0.5\times0.5\times0.5$ mm) then appears to be a key step in neonatal brain morphometry pipelines. In this work, we consider three different upsampling techniques:

- spline interpolation;
- non-local MRI upsampling [Rousseau, 2008, Manjón et al., 2010];
- deep learning-based method [Pham et al., 2017b];

Image interpolation is a widely used approach to compute isotropic data. However, interpolation models generally fail in accurately recovering fine details and textures in clinical LR data, leading mostly to blurred results.

Alternatively, the purpose of SR methods is to estimate finer reconstructions of HR images. Non-local MRI upsampling (NMU) [Manjón et al., 2010] iteratively applies the non-local means algorithm to the upsampled LR image. An observation model using a predefined point spread function is used to relate LR observation and HR estimation. The non-local approach provides an adaptive regularization approach and does not need to be trained, thus reducing data resource requirements.

The third method considered in this work is a deep learning-based approach, namely super-resolution residual-learning convolutional neuronal network (SRReCNN) [Pham et al., 2017b]. SRReCNN is a supervised method based on the assumption that the restoration model can be learnt from data. The problem is then expressed as the estimation of a restoration matrix which, combined to the spline interpolation of the LR input, provides its HR version. The restoration matrix is learnt using a CNN with a set of HR images similar to the target image, in terms of modality, observation, etc.

Cortex Segmentation

Popular approaches for brain segmentation rely on multi-atlas strategies. Such methods consist of three steps [Iglesias and Sabuncu, 2015]: (1) registration of the atlas images onto the target image; (2) application of the induced transformations to atlas labels; and (3) fusion of the transformed labels. In this section, we consider four different atlas-based segmentation pipelines, described below.

In atlas-based approaches, registration is carried out in two stages: first, affine and second, non-rigid registration, in order to first avoid local minima and then obtain an accurate matching of fine structures. The obtained registration fields are then used for mapping atlas label images onto the target image. Once the registration step is performed, segmentation maps can be obtained by fusing the deformed atlases. At this point, we consider four atlas-based segmenation methods:

- majority voting (noted MV) of the registered label atlas;
- iterative multi-atlas patch-based approach (Section 2.3);
- Draw-EM segmentation [Makropoulos et al., 2014];
- morphologically adaptive neonatal tissue segmentation [Beare et al., 2016];

A popular approach for label fusion is to average the deformed atlases and to apply the majority voting rule (MV) at voxel-scale. One of the limitations of MV is the strong dependency on registration accuracy.

To improve the robustness of MV, several fusion strategies have been developed. We propose to use the iterative multi-atlas patch-based approach (IMAPA) (Section 2.3), which was introduced in the previous chapter. As explained in Chapter 2, it is an iterative non-local method that computes atlas weights by minimizing a patch-based cost function. Moreover, this iterative approach takes advantage of current segmentation estimates as in cascading classifiers, to add regularization constraints on estimated segmentation maps. This approach has been shown to be very effective on HR neonatal brain MRI data (Section 2.3).

The third approach evaluated in this study is called Draw-EM [Makropoulos et al., 2014]. In this method, the input MR image is first brain-extracted and corrected for field inhomogeneity. Then, atlases are registered to the target image and the atlas labels are propagated to the image. The propagated labels are averaged in a locally-weighted scheme and subdivided with the use of subject-specific tissue priors obtained with k-means clustering. An expectation-maximization (EM) scheme is used for the estimation of the segmentation map.

The last method is MANTiS (Morphologically Adaptive Neonatal Tissue Segmentation) [Beare et al., 2016], which is based on the unified segmentation approach [Ashburner and Friston, 2005] implemented in SPM software. MANTiS makes use of a combination of unified segmentation, template adaptation via morphological segmentation tools and topological filtering, to segment the neonatal brain into eight tissue classes. Although one of its steps is based on the use of an atlas, this method does not require a external atlas set. Therefore, the application of MANTiS in our pipeline skips all the preprocessing steps for multi-atlas methods (atlas registration, atlas propagation and histogram matching).

Experiments and Results

Data

We used two distinct datasets: one for testing the upsampling and segmentation pipelines (called "test dataset"), the other for training the SRReCNN method and designing the multi-atlas set (called "training dataset"). Note that we only worked with T2-weighted (T2w) MR images, which present better contrast properties for cortical segmentation purpose.

Training datasets

Considering the HR image estimation step, SRReCNN is the only supervised approach that requires a set of training data. To learn the restoration matrix, we used the 40 images provided by the Developing Human Connectome Project (dHCP)[3] [Makropoulos et al., 2018]. The age of subjects varies between 37 and 44 weeks. Acquisitions were made with overlapping axial slices with voxel size $0.8 \times 0.8 \times 1.6$ mm every 0.8 mm. The resulting images have an isotropic resolution with voxel size $0.5 \times 0.5 \times 0.5$ mm. TR and TE are 12 000 and 156 ms, respectively. In order to complete the training step, these images were filtered by a Gaussian blur with the full-width-at-half-maximum (FWHM)

[3] `http://www.developingconnectome.org`

and downsampled (as in [Greenspan, 2009]) to obtain the same anisotropic low-resolution as the clinical data ($0.45 \times 0.45 \times 3.0mm$).

The four considered segmentation approaches make use of atlases. For MV and IMAPA, we have used the dHCP data as the multi-atlas set. The open-source implementation of DrawEM uses the ALBERT dataset [Gousias et al., 2012] and MANTiS is provided with a dedicated probabilistic template as an SPM toolbox.

Test dataset

There are currently very few available ground-truth data of cortex segmentation maps in clinical neonatal brain MRI. The NeoBrainS12 study [Igum et al., 2015] provides three different image sets of preterm born infants, in order to perform reliable comparison of the performance of segmentation algorithms. In this study, we have used two subjects from 40 weeks axial set (as mentioned in [Liu et al., 2016], there are significant regions missing in 30 weeks coronal scans that would result in an invalid comparison, see Figure 3.2). These two subjects from the 40 weeks axial set make up the training dataset, thus their segmentations are available. The size of voxels is $0.35 \times 0.35 \times 2.0$ mm. TR and TE are 6 293 ms and 120 ms, respectively.

To further assess the performance of segmentation pipelines on clinical LR images, manual delineation was performed on two MR images acquired at the University Hospital of Reims as part of the ANR MAIA project. Acquisitions were made at the term age (between 38 and 42 weeks), with anisotropic resolution ($0.45 \times 0.45 \times 3.0$ mm). TR and TE are 3 000 ms and 200 ms, respectively.

Manual segmentation protocols

The NeoBrainS12 study [Igum et al., 2015] has all the details of its acquisition and manual segmentation protocols in its web site[4]. In Figure 3.2, we show two different datasets with their corresponding manual segmentation. A surface mesh of the cortex segmentation is presented in Figure 3.3 emphasizing the strong anisotropic resolution.

On the other hand, reference segmentations of the ANR MAIA project were obtained by manually segmenting[5] T1-weighted (T1w) MR images, at a resolution $0.27 \times 0.27 \times 1.2$ mm. This dataset is not yet public to this day, thus manual segmentation protocol followed in order to obtain the reference segmentations is described as follows. Segmentation maps of ANR MAIA dataset (Figure 3.5) have 8 structures of interest: ventricular system, basal nuclei, cerebellum (subdivided in hemispheres and vermis), brainstem, cortical grey matter, myelinated white matter and unmyelinated white matter. The segmentation was performed using ITK Snap software and a tablet with a touch pencil. An implementation of non-local means method was applied to T1w images (Figure 3.4) in order to denoise them. The choice of using this modality for manual segmenting different brain structures instead of the T2w (which generally has a better inter-tissue contrast for this task) is justified by its higher resolution ($0.27 \times 0.27 \times 1.2$ mm). These facts made the task more comfortable to the clinician expert who works with a zoom of 15 px/mm.

[4] `http://neobrains12.isi.uu.nl/`

[5] A medical specialist in neonatology (H. Meunier) carry out these manual segmentations. Brains were labelled into seven classes: cortical grey matter, unmyelinated / myelinated white matter, basal ganglia and thalami, brainstem, cerebellum, and ventricles. The cerebellum was delimited laterally and posteriorly by the cistern of the fossea and anteriorly by the brainstem.

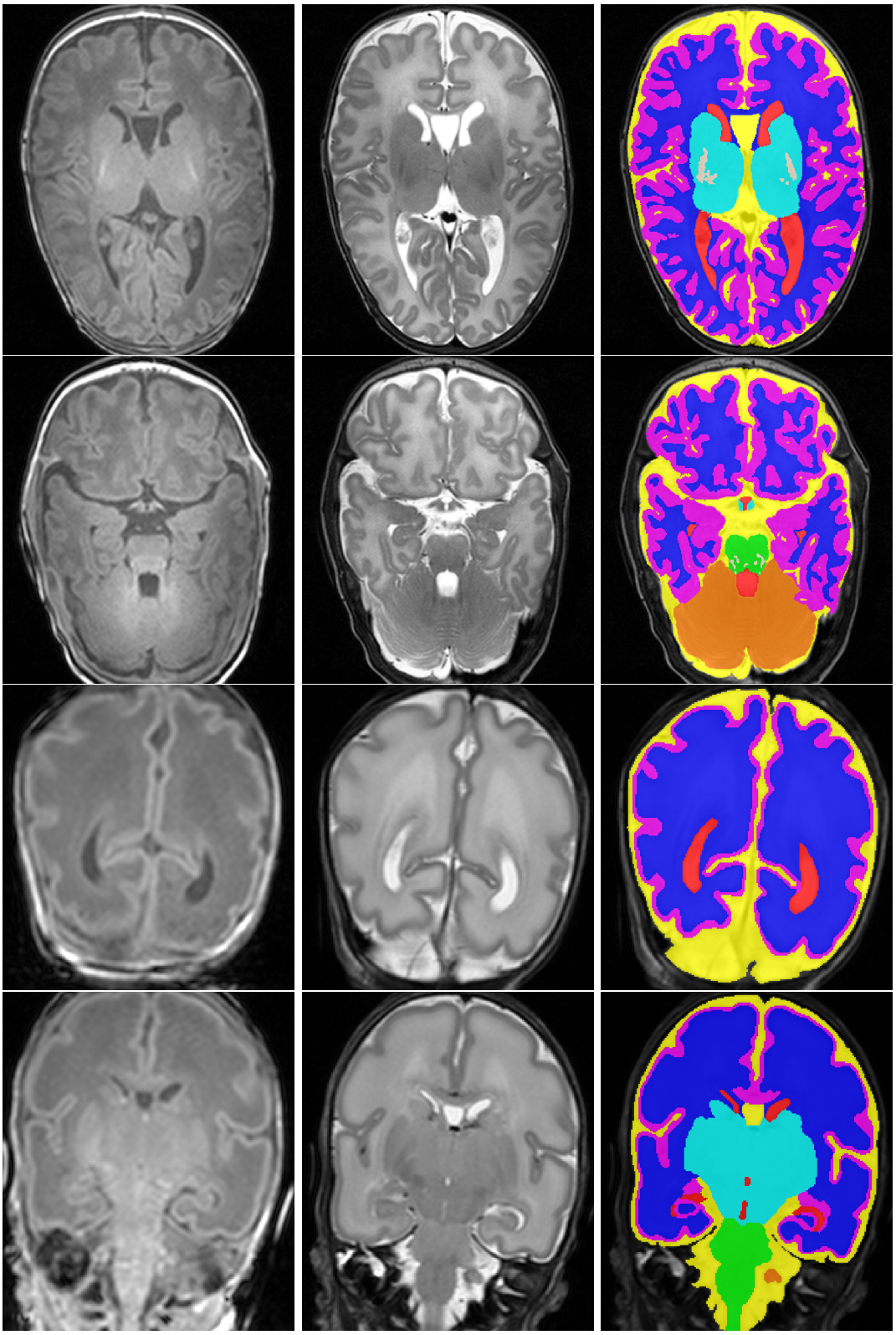

Figure 3.2 – Two examples of different dataset for NeoBrainS12 study. First two rows correspond to the axial 40w dataset and last two to the coronal 30w dataset. From left to right: T1w image, T2w image and their segmentation (ventricular system in red, basal ganglia and thalami in cyan, cerebellum in orange, cerebrospinal fluid in yellow, brainstem in green, cortical grey matter in magenta, myelinated white matter in beige and unmyelinated white matter in blue).

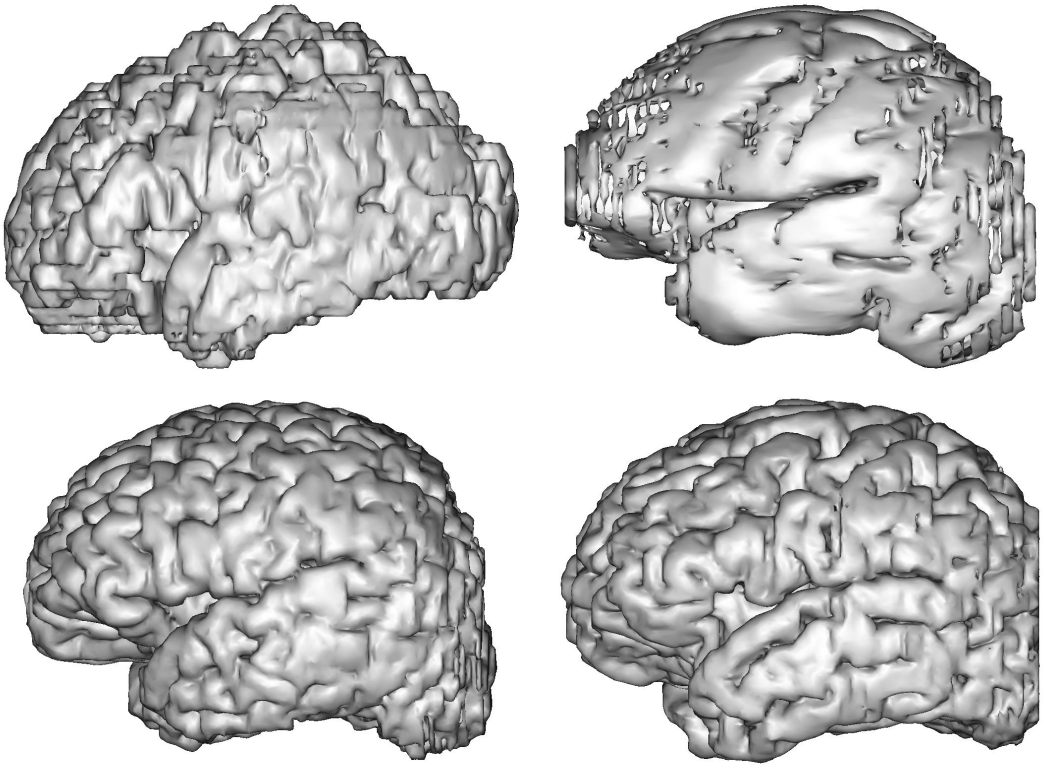

Figure 3.3 – Representation of surface meshes generated by the manual segmentations. The first row corresponds to subjects from NeoBrainS12 study and the second from ANR MAIA project.

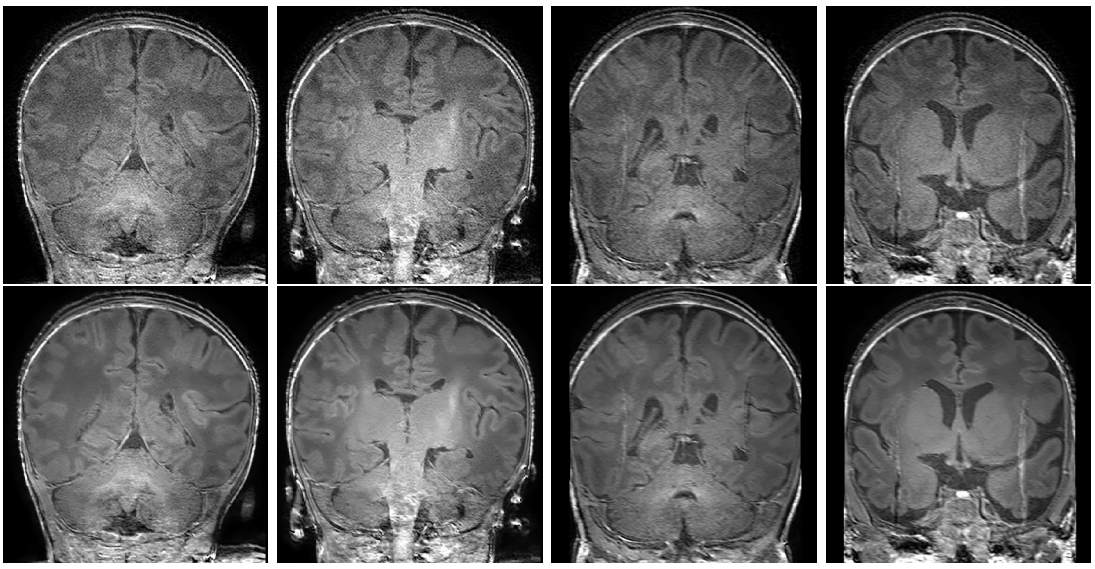

Figure 3.4 – Visualization of the denoised effect on ANR MAIA dataset. The first row shows the raw T1w MR image; the second row presents the application of denoised algorithm.

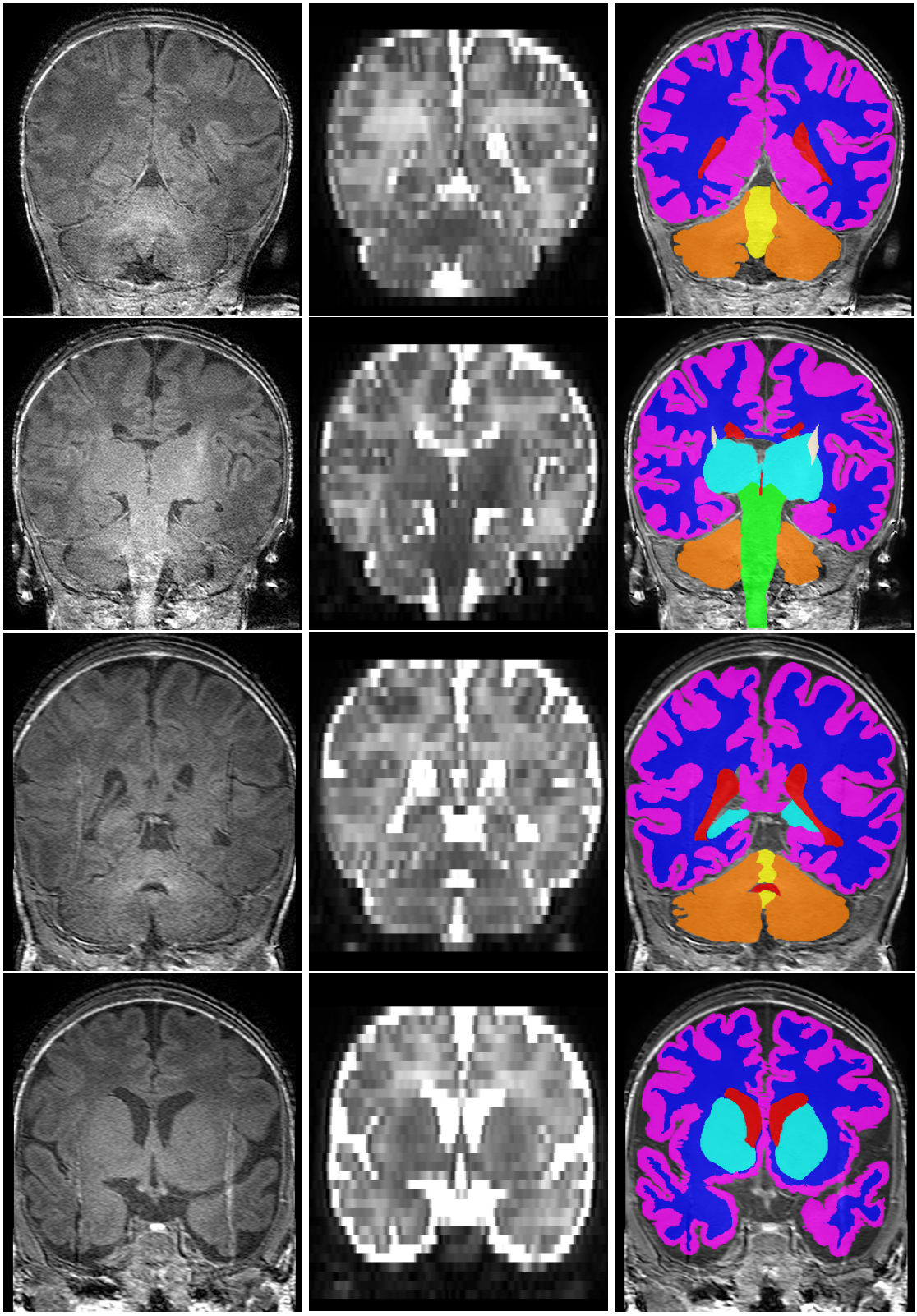

Figure 3.5 – Two subjects from the ANR MAIA dataset. Left to right: T1w MR image, T2w MR image and the manual segmentation (ventricular system in red, basal nuclei in cyan, cerebellar hemispheres in orange, vermis in yellow, brainstem in green, cortical grey matter in magenta, myelinated white matter in beige and unmyelinated white matter in blue).

Ventricular system is defined with the two lateral ventricles: third and fourth ventricles. The edges are characterized by its T1w hypointensity.

Basal nuclei include the bilateral caudate nucleus, lentiform nucleus and thalamus. Their limits are defined laterally with the adjacent WM by their hyperintensity in T1w and at the inferior pole by the brainstem limited by the cerebral peduncles. When there is myelination in the basal nuclei, it is labelled as myelinated WM.

Cerebellum segmentation consists of the cerebellar hemispheres (right and left) and cerebellar vermis. Hemispheres include the cerebellum WM, the deep cerebellar nuclei (i.e. the dentate nuclei, fastigal, globose and emboliform) and the three cerebellar peduncles (i.e. superior, middle and inferior). They are bounded laterally by the cistern of posterior fossa, anteriorly by the brainstem and medially by the vermis. On the other hand, the vermis is delimited laterally by the cerebellar WM and anteriorly by the fourth ventricule.

Brainstem includes the medula oblongata, occipital protuberances and cerebral peduncles. Its boundary is determined laterally by cerebral hemispheres and superiorly by cerebral peduncles by the thalamus. When there are myelination in cerebral peduncles, it is labelled as myelinated WM.

Cortical grey matter consists of the entire cortical band of grey matter inner the brain. It is highlighted in T1w hyperintensity, leading to be differentiated from the WM (inferior limit) and the CSF (exterior limit). When two sulcus are in contact (without CSF in the interior), it is considered as a continuity including it in the GM. In addition, when CSF is in the middle of two sulcus, it is classified as cortex, without CSF.

Myelinated white matter includes the affected regions in basal nuclei and cerebral peduncles. It is characterized by the T1w hyperintensity, which is differentiated from the unmyelinated WM, basal nuclei and brainstem.

Unmyelinated white matter consists of the subset of WM supra-temptory or myelinated WM, including the subplate. It is clearly distinguishable from unmyelinated WM and basal nuclei by the hypointensity in T1w.

As an additional information, this project distinguishes two types of vessels: great vessels and small vessels. Great vessels were determined considering a diameter larger than 2-3 mm (e.g. basilar artery or superior sagittal sinus). This type of vessels were not classified in any labels previously presented. In contrast, small vessels were included in the near tissue class, due to the difficulty for detecting such small structures. T1w images from MAIA dataset and their segmentation are shown in Figure 3.5.

Evaluation

After the HR reconstruction step, all images have a common isotropic voxel size of $0.5 \times 0.5 \times 0.5$ mm. It is important to note that this HR reconstruction does not have the same effect on MAIA and NeoBrainS12 data. Indeed, MAIA MR images have similar resolutions before / after the SR on two dimensions, whereas the third resolution is significantly increased (from 3 mm to 0.5 mm, i.e., a $\times 6$ factor). By contrast, NeoBrainS12 MR images have their resolution slightly decreased in two dimensions, whereas the third resolution is increased (from 2 mm to 0.5 mm, i.e., a $\times 4$ factor, lower than the $\times 6$ factor on MAIA). In other words, this SR step has a more relevant impact on the MAIA images (highly anisotropic) than on the NeoBrainS12 ones.

It is worth mentioning that the MAIA reference maps were natively at a low resolution (1.2 mm) in the anisotropic dimension, whereas the low resolution in the same dimension was obtained by downsampling of a HR reference map, in the case of Neo-

Table 3.2 – Dice scores (%) for the 12 combinations of upsampling (rows) and segmentation methods (columns) on the 4 images of MAIA and NeoBrainS12 (noted here NBS12) testing datasets. Existing used SR methods are NUM [Manjón et al., 2010] and SRReCNN [Pham et al., 2017b] that try the classical interpolation method and for segmentation methods there are MANTiS [Beare et al., 2016], IMAPA (Sec. 2.3) and DrawEM [Makropoulos et al., 2014] that try the majority voting.

Subject	Upsampling	Space	MV	MANTiS	IMAPA	DrawEM
MAIA #1	Interpolation	LR T2w	43.73	72.10	66.34	**73.72**
		HR T2w	43.46	70.37	63.71	71.73
		LR T1w	43.43	70.52	63.94	**71.98**
	NMU	LR T2w	44.73	72.66	67.21	**74.69**
		HR T2w	44.52	71.78	65.3	**73.65**
		LR T1w	44.51	71.90	65.51	**73.84**
	SRReCNN	LR T2w	43.67	73.37	67.33	**73.90**
		HR T2w	43.58	73.05	66.66	**73.26**
		LR T1w	43.68	73.30	66.98	**73.59**
MAIA #2	Interpolation	LR T2w	42.20	**72.08**	66.28	70.99
		HR T2w	42.04	**70.86**	64.25	69.95
		LR T1w	41.93	**71.18**	64.43	70.27
	NMU	LR T2w	42.64	73.34	67.71	**73.70**
		HR T2w	42.37	71.09	64.51	**71.47**
		LR T1w	42.42	71.82	64.97	**72.08**
	SRReCNN	LR T2w	42.04	**72.64**	67.48	71.84
		HR T2w	41.88	**72.65**	67.22	71.94
	LR T1w		41.94	**73.33**	67.63	72.51
NBS12 #1	Interpolation	LR T2w	42.07	77.52	59.72	**78.35**
		HR T2w	44.30	79.91	61.22	**80.96**
	NMU	LR T2w	41.55	**78.64**	65.33	77.25
		HR T2w	44.01	**80.71**	67.35	79.75
	SRReCNN	LR T2w	41.26	77.26	65.42	**78.39**
		HR T2w	43.29	79.61	66.66	**81.13**
NBS12 #2	Interpolation	LR T2w	44.70	80.05	62.02	**81.96**
		HR T2w	46.64	81.20	63.62	**84.12**
	NMU	LR T2w	44.49	80.74	66.17	**82.14**
		HR T2w	46.45	82.14	67.95	**84.55**
	SRReCNN	LR T2w	43.97	79.73	66.18	**81.30**
		HR T2w	45.79	81.13	67.08	**83.57**

BrainS12. In particular, these differences in the initial dimensions of the data and the distinct ways to express the LR reference segmentation for MAIA and NeoBrainS12 will shed light on slight variations observed in the results.

In order to quantitatively assess the segmentation results, they were compared to manual segmentations carried by experts, and used as reference. Since the results and the manual segmentations are in different spaces, we perform this quantification for each space according to the dataset used.

- MAIA: manual segmentation were obtained using the T1w images (which have a higher resolution than T2w images) as explained in Section 3.3.1.3. We differentiate three different spaces for evaluation:
  - LR T2w: the low-resolution T2w is the strongest anisotropic resolution ($0.45\times 0.45 \times 3.0$ mm), which corresponds to a different space for the manual seg-

mentation and the results, thus both images were registered with different deformations.

  - HR T2w: the manual segmentation is warped to the HR result space ($0.5 \times 0.5 \times 0.5$ mm).
  - LR T1w: an evaluation is performed in the manual segmentation space, thus a registration of the HR results ($0.27 \times 0.27 \times 1.2$ mm). This resolution is an intermediate state between the LR T2w input and the HR T2w output spaces.

- NeoBrainS12: manual segmentations were carried out in the T2w space, at high resolution ($0.5 \times 0.5 \times 0.5$ mm) with the protocol presented in [Igum et al., 2015]. Here, the manual segmentation and the LR T2w are in the same space, thus there are two spaces considered:

  - LR T2w: the results were downsampled to the input LR space ($0.35 \times 0.35 \times 2.0$ mm), avoiding the registration.
  - HR T2w: the LR T2w was registered to the HR results space ($0.5 \times 0.5 \times 0.5$ mm).

Since mapping are carried out by using input and reference images from the same subject, all registrations were performed with a rigid approach using the intensity images and propagating to the segmentation maps. In the case of mapping the LR T2w image to the results, a registration was performed per HR reconstruction method.

Parameters of the segmentation methods were set to their default values or following those proposed in the literature.

Results

Table 3.2 provides a quantitative assessment (Dice scores) of the results obtained with the proposed, combined upsampling and segmentation methods. Note that MV, MANTiS and DrawEM provide binary segmentations, by contrast to IMAPA that generates probabilistic segmentation maps. In order to compare all the results, the IMAPA outputs were thresholded at value 0.5. A more qualitative view is available in Figures 3.6, 3.7, 3.8 and 3.9 that illustrates results of these 12 combined methods on a coronal slice of one of the MAIA MR image and one of the NeoBrainS12 MR image though the different spaces.

Discussion

The Dice scores obtained with all methods are globally lower than those stated in the literature [Liu et al., 2016, Beare et al., 2016, Wang et al., 2014, Gui et al., 2012]. This can be explained by the increased difficulty to process clinical images, acquired with more noise, artifacts, anisotropy effects (not fully corrected by oversampling) and a low contrast. This highlights the remaining gap to be filled for making current automated methods dedicated to neonatal brain MRI, fully efficient for actual clinical routine.

In this challenging context, MANTiS and DrawEM present comparable Dice scores (0.7–0.8), with a slight advantage for DrawEM. In particular, they overcome IMAPA and MV. However, this quantitative analysis has to be completed by qualitative elements exemplified in Figures 3.7, 3.8 and 3.9. Indeed, one can observe that MANTiS and

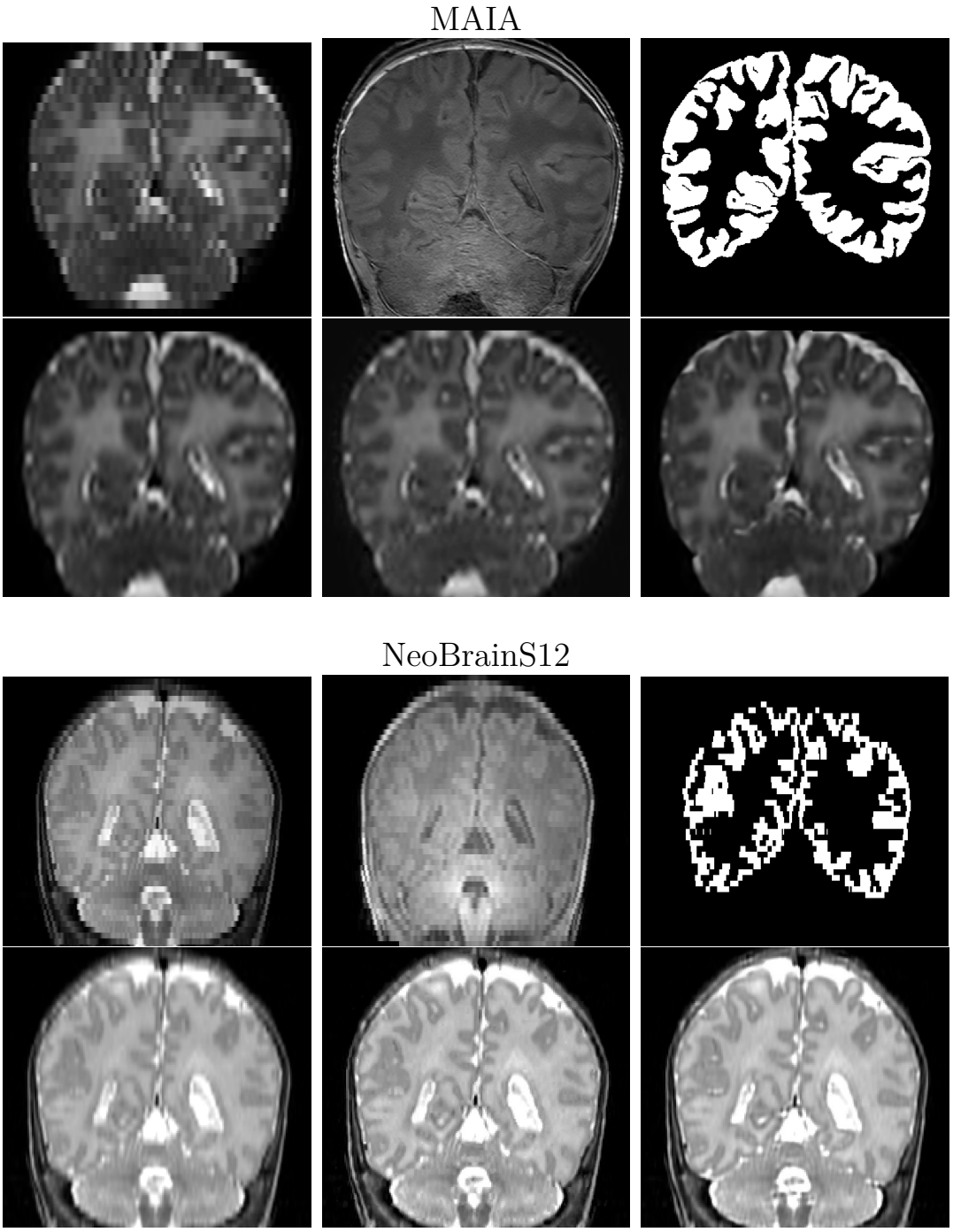

Figure 3.6 – A visual summary of the different estimations of HR input of subject MAIA #1 and subject NeoBrainS12 #1. First row corresponds to image from original dataset (LR T2w, T1w and the reference segmentation). In next row we present the HR T2w reconstruction result (interpolation, NMU and SRReCNN)

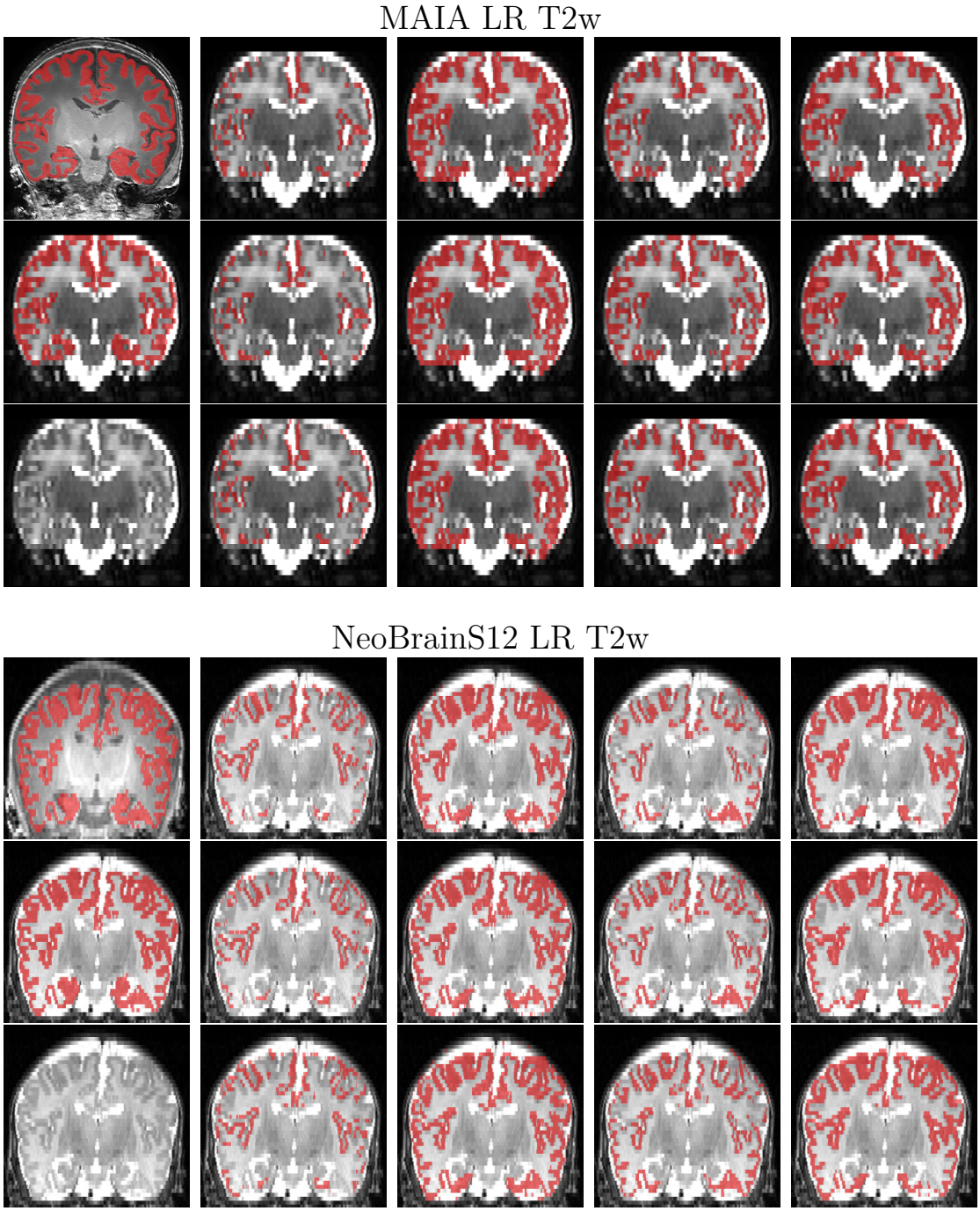

(a) Original data (b) MV (c) MANTiS (d) IMAPA (e) DrawEM

Figure 3.7 – A visual summary of the different estimations of segmentations using different HR reconstruction for subjects MAIA #1 and NeoBrainS12 #1 in the LR T2w space. (a) Original data. For each subject, first row corresponds to the T1w overlapping the manual segmentation, second to the T2w overlapping the warped manual segmentation and third to the T2w image. (b–e) Segmentation results with MV, MANTiS, IMAPA and DrawEM. First row corresponds to interpolation, second to NMU and third to SRReCNN.

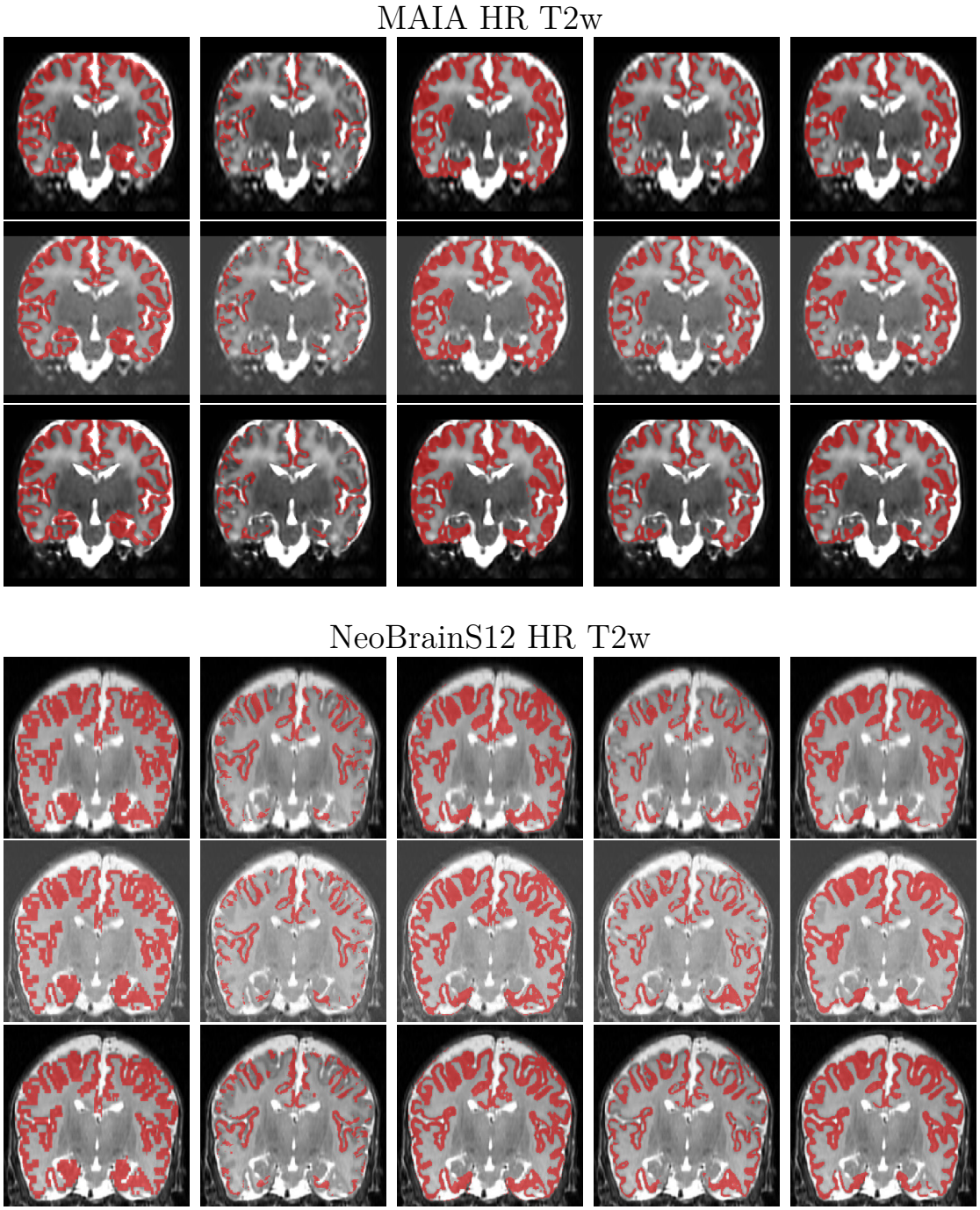

(a) Original data (b) MV (c) MANTiS (d) IMAPA (e) DrawEM

Figure 3.8 – A visual summary of the different estimations of segmentations using different HR reconstruction for subjects MAIA #1 and NeoBrainS12 #1 in the HR T2w space. (a) HR T2w reconstruction overlapping the manual segmentation. (b–e) Segmentation results with MV, MANTiS, IMAPA and DrawEM. (a–e) First row corresponds to interpolation, second to NMU and third to SRReCNN.

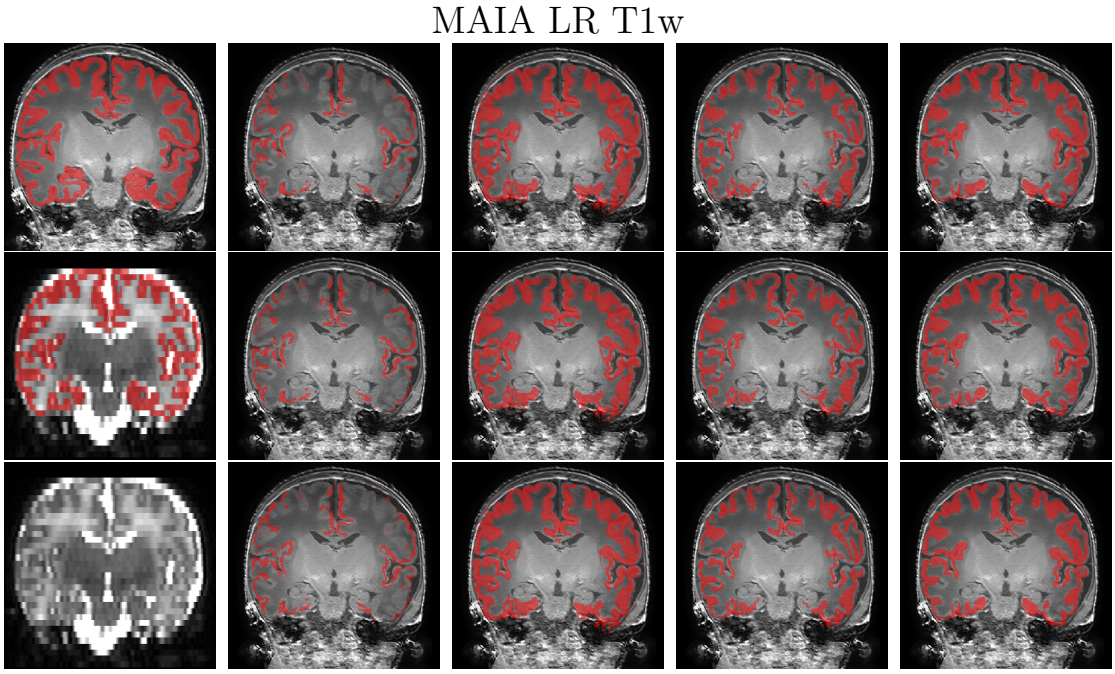

(a) Original data (b) MV (c) MANTiS (d) IMAPA (e) DrawEM

Figure 3.9 – A visual summary of the segmentation results for subjects MAIA #1 and NeoBrainS12 #1 in the LR T1w space. (a) Original data. For each subject, first row corresponds to the T1w overlapping the manual segmentation, second to the T2w overlapping the warped manual segmentation and third to the T2w image. (b–e) Segmentation results with MV, MANTiS, IMAPA and DrawEM. First row corresponds to interpolation, second to NMU and third to SRReCNN.

DrawEM oversegment the cortex, compared to IMAPA and MV, that undersegment this structure. In other words, two classes of segmentations appear, with dual and antagonist specificity / sensitivity properties.

The SR upsampling tends to improve the Dice scores obtained by segmentation methods. However, these improvements are weak, compared to segmentation on interpolated images. They are also method-dependent. For instance, MV has similar results for the three upsampling methods, whereas IMAPA behavior is clearly improved by SR. Such an improvement is also observed for MANTiS and DrawEM for the MAIA dataset, but not for NeoBrainS12.

Despite the fact that there is a slight improvement in the qualitative results by using more sophisticated SR upsampling methods, the quantitative results (Figures 3.7, 3.8 and 3.9) seems to be invariant to that effect. Further experiments have to be performed in order to study this consequence.

The quantitative evaluation through the different spaces shows a variation in Dice scores (Table 3.2). For MAIA dataset, the propagation of the results and the manual segmentation to the LR T2w input gives the best score, followed by the warp of the manual segmentation in the intermediate space to HR T2w reconstruction space and finally the intermediate space LR T1w. This dataset seems to be sensitive to the registration step, in particular to the intermodality one. In Figure 3.8, the manual segmentation has problems to fit with the HR T2w images, thus the quantitative score is weaker than in LR T2w space. On the other hand, NeoBrainS12 evaluation presents the opposite behaviour: the HR T2 space is better scored than the LR. In this case, it seems that reconstructing the HR gives a gain in quality of the segmentation for this data.

In addition, we notice that the strong anisotropic resolution affects the segmentation reference even for clinicians. In Figure 3.10, we present some of them in axial an sagittal plane from a subject of Coronal 30 in NeoBrainS12 dataset. The multi-atlas method is a supervised learning approach that strongly depends on the quality of annotations. Thus making it robust to manual segmentation variability could be integrated in future works on this pipeline.

Conclusion

The main conclusions of this study are the following. First, the current automated, neonatal cortex segmentation methods can hardly provide satisfactory segmentations of real clinical low resolution MR images, even with the assistance of an oversampling preprocessing step. Secondly, the behavior of these methods is not homogeneous, and two families emerge, that tend to oversegment and undersegment the cortex, respectively. Thirdly, oversampling with SR approaches tends to improve the overall quality of the segmented cortex, but this progress remains slight, compared to interpolation.

Future work emphasized by these results will consist in taking advantage of the complementary behaviors of the existing segmentation methods, in order to improve both specificity and sensitivity. To this end, we will consider segmentation fusion strategies. In addition, we will more deeply investigate why the current SR method does not allow us to significantly improve the overall quality of segmentation results on such reconstructed data.

Moreover, estimated segmentation maps are not evaluated on their HR space ($0.5 \times 0.5 \times 0.5$ mm) but in the manual segmentation space (anisotropic LR). This leads to rigidly warp or downsample the result, reducing the details and losing the gain given by

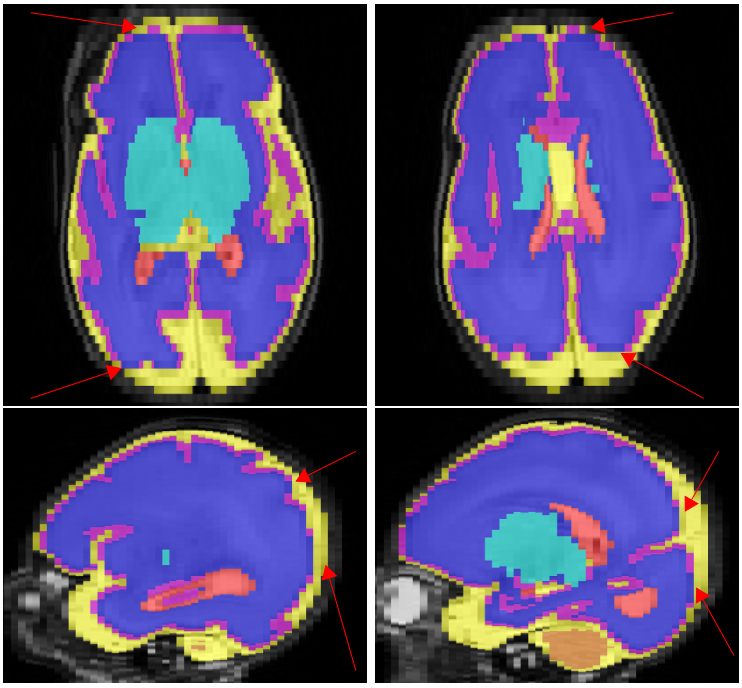

Figure 3.10 – Errors in manual segmentations (indicated by red arrows) in NeoBrainS12 at coronal 30w dataset.

SR methods. Thus, the evaluation on different spaces has to be investigated in order to quantify the SR gain.

Chapter 4

Topology modeling of segmentation maps

Introduction

Topological methods generate an interest in the field of medical image processing and analysis. Indeed, ensuring the coherence of structural properties of organs and tissues in 3D medical data is a cornerstone e.g. for registration, modeling or visualization tasks. In particular, topological concepts developed in the field of discrete imagery, and in particular digital topology, can allow for the development of efficient approaches that take into account not only quantitative and morphometric information carried by anatomical objects of interest, but also more intrinsic properties related to their structure [Saha et al., 2015].

In particular, the brain has received a specific attention. Indeed it exhibits an important interindividual variability from shape and size points of view. In the meantime, it is organized into many distinct subparts and tissues with a strong topological invariance. Taking into account topological priors is then a relevant hypothesis for guiding and/or regularizing image processing procedures [Pham et al., 2010].

Beyond the brain tissues, cortical surface is a thin structure in the brain, in particular for the neonatal brain. Moreover, other factors that hinder the automatic segmentation

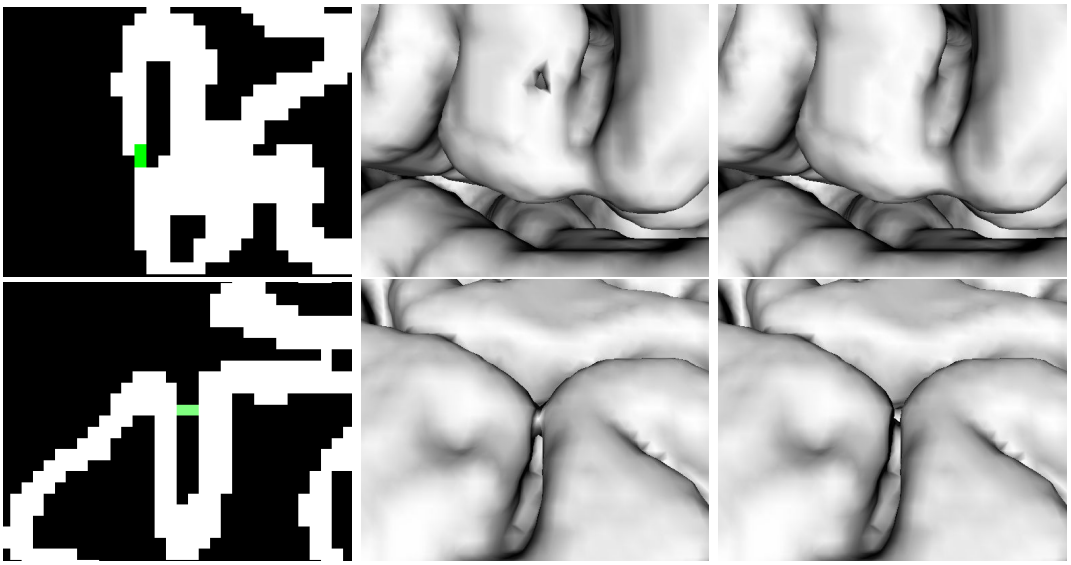

Figure 4.1 – Visualization of topological errors (hole in the first row; handle in the second) in a cortical segmentation (left) and its corresponding mesh with the error (center) and without it (right).

are the cortical folding and low-resolution acquisition in clinical data (study in Chapter 3). As mentioned in [Li et al., 2019], undesired topological patterns are classified as holes or handles. The presence of these topological patterns leads to errors in the segmentation that modify the topology of the structure. Thus, introducing a topological correction to the segmentation is a relevant task.

These topological defects are caused by wrong connections in the cortex segmentation. The so-called hole commonly refers to a discontinuity of the segmented structure. A handle, on the other hand, corresponds to a bridge between non-adjacent regions. Due to the thin thickness of the cortex in neonatal MRI, these errors are often subtle but can set off negative impacts, e.g. in the case of mesh generation. In Figure 4.1 we show an example of each topological defect and their impact in the meshing application.

Topology-based segmentation methods dedicated to brain structures can be mainly divided into two families [Pham et al., 2010]: on the one hand, the methods that consider a topological prior for guidance from the very beginning of the process; on the other hand, the methods that aim at recovering a posteriori topological properties. The first lie in the family of topological deformable models; the second in the family of topological correction methods. In this chapter we focus on the second option.

Topological correction

Most of the approaches based on topological correction of a brain segmentation consider three main classes of tissues, namely grey matter (GM) (mainly, the cortex), white matter (WM), and cerebrospinal fluid (CSF). A majority of the proposed methods [Shattuck and Leahy, 2001,Fischl et al., 2001,Ségonne et al., 2007,Hao et al., 2016,Sun et al., 2019] focus on the cortex, that presents a complex geometry, with strong folding and a low thickness, leading to a high curvature 2D-like thin ribbon. Cortex segmentation is generally presented as a binary segmentation problem (cortex vs. other structures) or a ternary segmentation problem (GM, WM, CSF).

Several types of methods were proposed in order to correct brain segmentation topology. The methodology employed is basically determined by two steps: (1) locate the topological errors on the segmentation image and (2) correct these topological defects. From a technical point of view, the literature presents several solutions based on: graph [Shattuck and Leahy, 2001, Han et al., 2002], surface mapping [Fischl et al., 2001, Ségonne et al., 2007] or topology-preserving deformation [Han et al., 2003, Bazin and Pham, 2007b, Shiee et al., 2010, Cardoso et al., 2011].

Graph-based methods, as [Shattuck and Leahy, 2001], transform the WM segmentation into a graph, where the nodes have to be connected without cycles (so-called a tree). The cycles are considered topological errors and are corrected by performing voxels changes from foreground to background and vice versa. The choice of the operation is done by minimizing a graph criterion, e.g. minimal changes in the volume [Han et al., 2002] or building a maximum sub-graph tree [Han et al., 2002]. This leads to discard a non-relevant part of the putative cortical surface. On the other hand, surface mapping is based on the overlapping of surface meshes from the segmentation and a topologically correct volume (typically a sphere for the WM) after remapping. Nevertheless, the classification of holes and handles based only on geometric information (i.e. a mesh) is a difficult task.

Moreover, most of these methods are specifically dedicated to adult brain, hampering the application to neonatal data [Mangin et al., 1995, Ségonne et al., 2007, Yotter et al., 2011]. For example, in a strategy integrated in FreeSurfer software [Ségonne et al., 2007], a prior is used based on intensity levels from T1w MR images to refine its segmentation. As discussed in the previous chapters, the features of MR images in adults and infants present differences that may require the development of dedicated algorithm for a same task.

Recently, some topological correction algorithms were proposed for neonatal brain segmentation [Makropoulos et al., 2017, Wang et al., 2018, Hao et al., 2016, Sun et al., 2019]. The pipeline presented in [Makropoulos et al., 2018] includes a topological correction for the WM surface by inflating a sphere. Then, a deformation method is applied based on the T2w intensity 1-D profile and its gradient. Wang et al. [Wang et al., 2018] present a topology correction based on the integration of the cortical thickness to the random tree algorithm, that is called anatomical guidance. Finally, in [Hao et al., 2016, Sun et al., 2019] the topology-preserving level set designed in [Han et al., 2003] is leveraged to locate the topology errors. These errors are corrected using a supervised learning approach such as a dictionary [Hao et al., 2016] or a CNN [Sun et al., 2019] previously trained with an atlas set.

However, the first step of the algorithms presented here, i.e. location of topological defects, leads to restrict the search area by relying on hypotheses on their probable location, ignoring the remainder of the segmented structure. For instance in [Cardoso et al., 2011], a topological correction is presented for each iteration of an EM algorithm with Gaussian mixture model (GMM) and a Markov random field (MRF) used for regularization purpose (e.g. avoid isolated points). The Khalimsky cubic complex is considered in order to augment space and to be topologically consistent on the thinnest sulcus. The algorithm assumes the probable location of the topological errors in the sulcus and gyrus; thus, these regions are automatically detected and corrected until a satisfactory Euler characteristic. However, we show in Figure 4.2 that holes can be located out of the sulcus and gyrus.

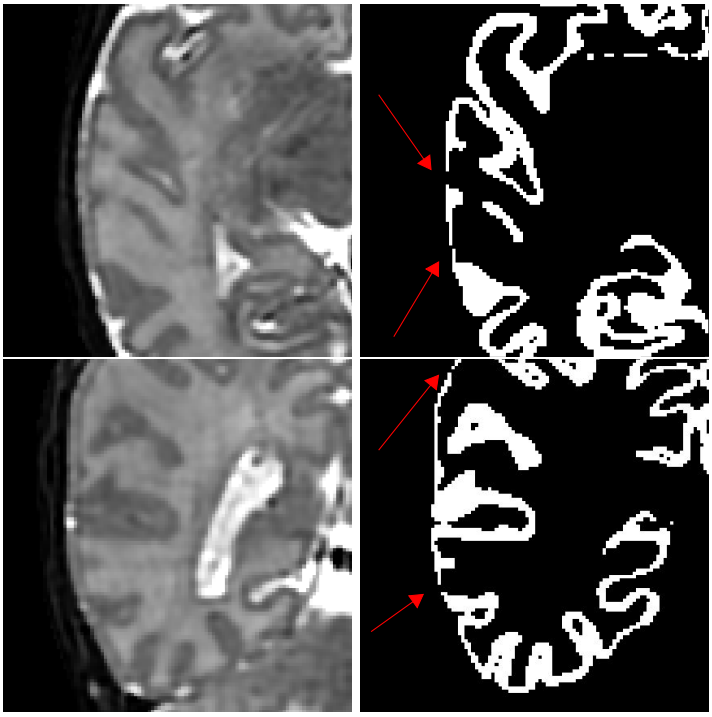

Figure 4.2 – Discontinuities on cortical surface segmentation located out of a sulcus or gyrus (indicated by red arrows).

Topology-preserving methods

Since the pioneering works proposed in [Mangin et al., 1995, Malandain et al., 1993], different variants of global topological deformable models have been proposed. These approaches spread from fully discrete paradigms [Caldairou et al., 2011a] to coupling continuous and digital models [Han et al., 2003]. They require an initial topological assumption to deform the structure preserving this topology.

The associated topological hypotheses are often a simplified version of the anatomical reality, and the different classes of tissues are assumed nested: the central class is simply connected (i.e. a full sphere) with successively nested hollow spheres. Based on these simplified assumptions, it is possible to develop segmentation strategies from binary digital topology [Kong, 1989], and in particular homotopic transformations based on simple points [Couprie and Bertrand, 2009] (less frequently, alternative topological models were proposed, for instance cellular complexes [Cointepas et al., 2001, Damiand et al., 2011]). On the other hand, several methods model each hemisphere independently with a sphere [Shattuck and Leahy, 2001, Ségonne et al., 2007, Fischl et al., 2001, Yotter et al., 2011, Hao et al., 2016, Sun et al., 2019]. However, both models are not completely correct; thus a model that relaxes locally the topology following an anatomical criterion is an interesting track in the domain.

Unfortunately, the hard topological constraints imposed by the model can lead to deadlocks that are then difficult to handle. In [Faisan et al., 2011], a pairwise strategy is proposed in complement with simple points in order to reduce deadlocks. Some deadlocks became the so-called topological monsters, binary structures that cannot be reduced to a unique element using simple points. Passat et al. [Passat et al., 2007] introduced the notion of simple pair to partially tackle this problem.

Based on the same topological hypotheses, many topology correction methods have been proposed for the cortex [Shattuck and Leahy, 2001, Ségonne et al., 2007, Fischl et al., 2001, Yotter et al., 2011, Hao et al., 2016, Sun et al., 2019]. They mainly consist of identifying the tunnels / handles generated on the cortical surface, and removing them based on *ad hoc* strategies [Kriegeskorte and Goebel, 2001, Bazin and Pham, 2007a]. These methods aim at reformulating the topological problem to be solved by considering a binary, simply connected topological model. This has the virtue to be easy to handle, but the drawback of poorly modeling the anatomical structures.

More recently, new ways were explored for tackling the issue of real multilabel segmentation and/or potentially complex topologies. Handling complex topology can be done by relying on less constraining—but also less robust—topological invariants, such as the genus [Ségonne, 2008]. In [Mazo et al., 2012b], Mazo proposed a framework for modelling the topology of multilabel digital images.

Homotopic transformations based on simple points however remain the gold standard for carrying out a topology-preserving deformation. In order to avoid topological deadlocks, non-monotonic transformation processes of complex, multilabel topological models were investigated [Poupon et al., 1998, Bazin and Pham, 2007b]. Although promising, these approaches suffer from various theoretical weaknesses [Shattuck and Leahy, 2001, Poupon et al., 1998, Bazin et al., 2007, Siqueira et al., 2008], which rely on incompletely proved theoretical bases or conjectures, discussed in [Mazo et al., 2012a]. They also work at a unique scale, with induced difficulties to ensure simultaneously spatial / geometrical and topological reliability.

In this chapter, we focus on homotopic deformations using the notion of simple point. These kinds of approaches are, to the best of our knowledge, the most efficient techniques in order to ensure a certain topological configuration to a set of labels [Mazo et al., 2012b]. The main topic is to present a contribution in the field of topology-based brain structure segmentation. In particular, we focus on topological post-processing of multi-label segmentation maps obtained beforehand with efficient, but non-topologically guided, methods. Our purpose is then to build, from such segmentation maps, a corrected output consolidated by topological priors.

However, the embedding of topological priors in segmentation paradigms is a complex task, a fortiori when we consider n-ary segmentation, with $n > 2$, i.e. more than one object vs. its background. In this context, our contributions are the following. First, we rely on a topological framework introduced a few years ago, that allows to correctly model digital images by considering the topology of n labels but also that of the combinations within their power lattice [Mazo, 2012, Mazo et al., 2012b]. Second, we consider a multiscale approach for topological modeling of the cerebral structures. Indeed, we assume that the topological assumptions that should guide a segmentation process actually depend on the level of details of the observed structures. Based on these two, multilabel and multiscale, paradigms, we develop a generic, homotopic deformable model methodology that progressively refines a segmentation map with respect to the data and the associated topological priors.

In Section 4.2, we recall the involved topological framework and how it can be used for multiscale, multilabel topological modeling of anatomical structures. In Section 4.3, we describe the algorithmic scheme that allows us to progressively refine an initial segmentation with respect to this multiscale topological modeling. Experimental results are proposed in Section 4.4. In Section 4.5, we discuss the results and the accuracy of the proposed method. Section 4.6 concludes this chapter by presenting the main perspectives offered by the proposed approach and the remaining challenges to be tackled.

Multilabel, Multiscale Topological Modeling

Theory of multilabel strategy

In [Mazo et al., 2012b], Mazo proposed a framework for modeling the topology of multilabel digital images. The main ideas of this framework are as follows.

1. The multilabel image is split in a collection of binary images such that each binary image represents a region of interest. Each region has been previously labelled or represents a meaningful union of some labeled regions. The unions are labeled thanks to a lattice structure: the label of a union of regions is the supremum of the labels of the regions.

2. Each binary digital image is embedded in a partially ordered set (poset) by adding intervoxel elements (pointels, linels, surfels). Such elements are assigned to the foreground or the background thanks to the minimum (6-adjacency) or maximum (26-adjacency) membership rule. Doing so, the connected components are preserved and the digital fundamental groups, as defined by Kong [Kong, 1989], are mapped, through isomorphisms, to the fundamental groups of the Alexandrov topology [Mazo, 2012].

In this framework, a homotopic relabelling boils down to a collection of simple point moves in binary images with the guarantee to preserve the underlying topological structures of the involved posets, and in particular their homotopy types.

Application of multilabel strategy

In the applicative context of this work, our purpose is to post-process ternary classification maps of MR images defined as

$$\left| \begin{array}{rcccl} F & : & \Omega & \to & [0,1]^3 \\ & & x & \mapsto & (p_{\mathrm{CSF}}, p_{\mathrm{GM}}, p_{\mathrm{WM}}) \end{array} \right. \tag{4.1}$$

where Ω is a part of $\mathbb{Z}^3$ corresponding to the support of an MR image, and for each point x, p_{CSF}, p_{GM} and p_{WM} are the probabilities that x belong to the cerebrospinal fluid (CSF), the grey matter (GM) and the white matter (WM), respectively. In particular, we have $\sum_\ell p_\ell = 1$.

Such maps F are the uncorrected segmentations that will guide the homotopic deformation. This set of segmentations could be obtained automatically by a segmentation algorithm that provides hard segmentations such as [Wang et al., 2013a, Beare et al., 2016] or by a consequence of fuzzy segmentation process, see e.g. [Caldairou et al., 2011b] or our first contibution (Section 2.3). A specificity of those segmentation strategies—and many others—lies in the fact that they are not guided by topological constraints. As a consequence, their outputs need to be post-processed for any further application requiring topological guarantees (for instance mesh generation or differential cortical surface analysis). In addition, checking every topological error manually is a tedious and difficult task, comparable to manually segmenting a structure. As a result, the reference segmentation F can be also provided by a set of manual segmentations in order to correct topology.

Our purpose is then to build, from F, a new crisp segmentation map

$$\left| \begin{array}{rcccl} T & : & \Omega & \to & \{0,1\}^3 \\ & & x & \mapsto & (c_{CSF}, c_{GM}, c_{WM}) \end{array} \right. \tag{4.2}$$

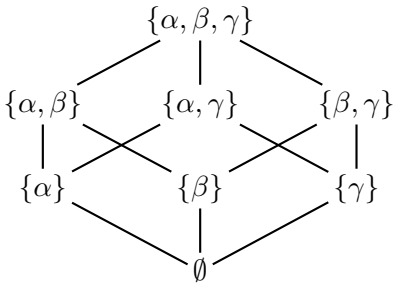

Figure 4.3 – The power lattice $\Lambda = 2^L$ for the set of labels $L = \{\alpha, \beta, \gamma\}$ of the three considered classes of cerebral tissues.

such that for each point x, c_{CSF}, c_{GM} and c_{WM} are equal to either 0 or 1 depending on the (unique) class of x, i.e. with $\sum_\ell c_\ell = 1$.

In addition, T should satisfy—unlike F—some topological priors related to the structure of the different tissues. Indeed, this map will be the image that contains the set of labels (in a binary form) that we will deform whereas preserving their initial topology.

Multiscale topological modeling

The framework proposed in [Mazo et al., 2012b] allows us to model the topological structure of the three classes of cerebral tissues of interest, namely CSF, GM and WM, further noted γ, β and α, respectively, for the sake of concision. It also allows us to model any combinations of these labels, leading to the whole power lattice $\Lambda = 2^L$; see Figure 4.3.

In particular, in [Mazo et al., 2012b], the notion of topology preservation relies on the definition of simple points that preserve the homotopy type of *all* the labels of Λ. However, it is possible to consider the notion of simpleness for only a given (strict) subset of labels of Λ. In such a case, it is sufficient to guarantee that the relabelling of a (simple) point fulfills the required topological conditions for the chosen subset of labels, while the topology of the objects / complexes induced by the other labels are allowed to evolve.

This strategy, that only focuses on specific (combinations of) labels of interest, allows us to define a multiscale topological modeling. Indeed, the notion of topology in discrete imaging is strongly related to the scale of observation of the objects of interest. For instance, fine topological details that are significant at a high resolution, become irrelevant (and sometimes incorrect) at a coarser resolution, due to the loss of precision induced by partial volume effects. In addition, by using a multi-scale strategy, we hope to drive the label deformation toward a desired solution, avoiding local minima.

Based on this assumption, we consider two distinct topological models of the brain tissues, according to their scale (see Figure 4.4):

- **Model 1 – Coarse / intermediate scales ($\mathbf{S}_1$, $\mathbf{S}_2$, $\mathbf{S}_3$)**: At these scales, we assume that the WM, GM and CSF are successively nested, which is the hypothesis currently considered in the literature. In other words, we aim at preserving the homotopy type of three labels: $\{\alpha\}$ (simply connected); $\{\beta\}$ (hollow sphere); and γ (hollow sphere); but also the homotopy type of their four combinations.

- **Model 2 – intermediate / fine scales ($\mathbf{S}_3$ and $\mathbf{S}_4$)**: At these scales, we assume that the cortex (GM) is no longer a hollow sphere. Indeed, on the lower part of

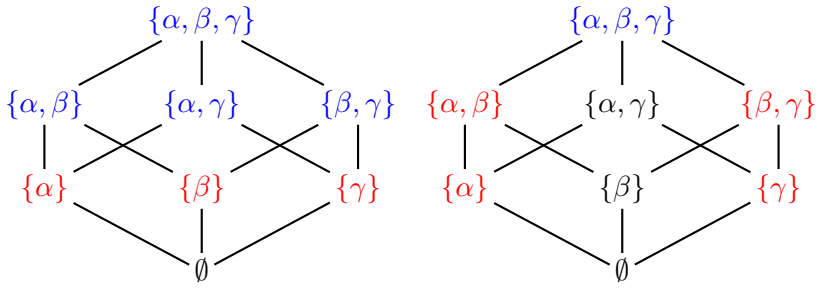

(a) Model 1: scales 1, 2 & 3 (b) Model 2: scales 3 & 4

Figure 4.4 – Topological modeling of the classes of brain tissues, at the coarse / intermediate (a) and intermediate / fine scales (b). The labels coloured in red and purple are those for which the topology has to be preserved. The red labels need to be explicitly handled; the topology of the purple labels is preserved as a corollary of the topological preservation of the red ones. The topology of the black labels is authorized to evolve during the transformation process.

the encephalus, the hypothesis of GM surrounding WM is not satisfied (due to the connection of the encephalus to the brainstem). Based on this hypothesis, we aim at preserving the homotopy type of five labels: $\{\alpha\}$ (simply connected); $\{\alpha, \beta\}$ (simply connected); $\{\beta, \gamma\}$ (hollow sphere); $\{\gamma\}$ (hollow sphere); and $\{\alpha, \beta, \gamma\}$ (simply connected). In particular, this allows to make the topology of the cortex evolve whereas remaining coherent with respect to its neighboring structures (CSF and WM).

This differentiation of models adds flexibility to the framework in order to adapt the initial topological equivalence assumption of brain structures. Moreover, these models can be applied locally in combination of a prior. For instance, if we apply model 2 to the whole image, the deformation algorithm could delete the cortical label where the topological defects of the reference segmentation are located. However, if the model 2 is applied using a spatial prior that ensures the absence of GM, topological errors will be avoided.

Multilabel, Multiscale Topology-Controlled Deformation

We now describe how the topological assumptions modeled above can be considered for designing, at each scale, well-fitted homotopy type preserving deformation processes.

Grid refinement

We work on a space Ω defined as a subset of $\mathbb{Z}^3$. In order to carry out the deformation process at each scale, this space Ω has to be adapted to the current scale. It is important to note that the notions of simple points and homotopy type are compliant with respect to digital grid refinement. In other words, a digital object X defined in $\mathbb{Z}^3$ (and more generally in $\mathbb{Z}^n$) has the same homotopy type as its up-sampled analogue X_2 in $\mathbb{Z}^3$, defined by $x \in X_2 \subset \mathbb{Z}^3 \Leftrightarrow \lfloor x/2 \rfloor \in X$. In addition, x is a simple point for X iff there exists a sequence of successively simple points for X_2 composed from the 8 points of $2x + \{0, 1\}^3$. This topology-preserving octree refinement [Bai et al., 2009] remains trivially valid for up-samplings at any other (discrete) resolution.

In particular, we consider a scale factor $k \in \mathbb{N}$, $k > 1$, between the grids of each scale. The set $\Gamma_1 \subset \mathbb{Z}^3$ is the grid considered at the coarse scale S_1. It is refined, at scale S_2 into a second grid Γ_2 such that $\Gamma_1 = k\Gamma_2$, which means that one point of Γ_1 corresponds to k^3 points of Γ_2. Then, Γ_2 is refined into a third grid Γ_3 such that $\Gamma_2 = k\Gamma_3$; this means that one point of Γ_1 corresponds to k^3 points of Γ_2 and k^6 points of Γ_3. Note that we have $\Omega = \Gamma_3$. It is then convenient to assume (without loss of generality) that Ω is defined as a Cartesian product $\prod_{i=1}^{3} [\![0, N_i - 1]\!] \subset \mathbb{Z}^3$ such that N_i is a multiple of k^2 for any $i = 1, 2, 3$.

Simple points

The proposed deformable algorithm (Algorithm 2) relies on the modification of simple points in order to preserve the initial topological properties. Several contributions proposed different definitions of a simple point in a 3D digital image [Malandain and Bertrand, 1992, Bertrand and Malandain, 1994, Bertrand, 1994, Couprie and Bertrand, 2009].

In order to generalize the definition according to the connectivity configuration, let us defined α-path as a sequence of points $x_0 ... x_k$, with x_i α-adjacent to x_{i-1} for $i = 1, ..., k$. Let $N_\alpha^k(x, X)$ be the geodesic α–neighborhood of order k of x in X that corresponds to the set of points $X \cap N_{26}(x)$ linked to x by an α-path of length at most k. Let $G_\alpha(x, X)$ be the geodesic α–neighborhood of x of order k with $k = 1$ if $\alpha = 26$, $k = 2$ if $\alpha = 18$, $k = 3$ if $\alpha = 6^+$ and $k = 2$ if $\alpha = 6$. Finally, let $T_\alpha(x, X)$ be the number of connected component α-adjacent in $G_\alpha(x, X)$. With these definitions in mind, we present two conditions as follows:

- $T_\alpha(x, X) = 1$
- $T_\beta(x, \bar{X} \cup \{x\}) = 1$

If these previous conditions are fulfilled, we can ensure that x is a simple point in X. Notice that the four possible settings for α–β are 6–26, 26–6, 6^+–18 and 18–6^+. A more intuitive point-of-view of this definition is that a point is simple if and only if there is a unique connected component in the object X and in its geodesic neighborhood $G_\alpha(x, X)$.

Metrics

In order to guide the topology-controlled transformation process, we need to define metrics for assessing the error between the current (evolving) segmentation map and the target segmentation map. In particular, by minimizing a cost function associated to this error, our purpose is to make the segmentation map progressively converge onto the target, whereas correctly handling the topology.

In this context, we consider two metrics. The first is a classification metric, noted M_1, defined by the classification error at each point of the image. The second, noted M_2, is a distance-based metric, defined by the ℓ_1 distance between the misclassified points and the corresponding, correctly classified region in the target image.

In order to build these two metrics, we first need to define fuzzy classification maps F_i from F (see Eq. (4.1)) at each scale i ($i = 1, 2, 3$). This is done with a standard mean policy:

$$F_i(x) = \frac{1}{k^{3.(3-i)}} \sum_{a=0}^{k^{(3-i)}-1} \sum_{b=0}^{k^{(3-i)}-1} \sum_{c=0}^{k^{(3-i)}-1} F(k^{(3-i)}x + (a, b, c)). \tag{4.3}$$

In particular, we have $F_3 = F$.

For a given (crisp) segmentation map C, the first metric M_1 assessing the error between C and F_i is then defined as:

$$M_1(C, F_i) = \sum_x \|C(x) - F_i(x)\|_2. \tag{4.4}$$

For defining the second metric M_2, we build crisp classification maps G_i from the fuzzy maps F_i by a thresholding, instead of a majority voting process. The reason is that majority voting keeps those voxels that are ambiguous in terms of label membership, i.e. when the probability distribution in a voxel is closely uniform (1/3 in a ternary classification). By setting the threshold to 0.5, we attempt to find for each voxel a clear winner. If there is no winner, the voxel is unclassified (i.e. null).

For a given (crisp) map C, the second metric M_2 assessing the error between C and G_i is then defined as:

$$M_2(C, G_i) = \sum_x \Delta(x, G_i^{-1}(C(x))) \tag{4.5}$$

where $\Delta(x, X) = \min_{y \in X} \|x - y\|_2$ is the ℓ_2 distance between the point x and the set X, whereas $G_i^{-1}(v) = \{x \mid G_i(x) = v\}$. In particular, we have $\Delta(x, G_i^{-1}(C(x))) = 0$ iff $C(x) = G_i(x)$. In other words, $\Delta(x, X)$ is the distance transformation of $\bar{X}$.

Since the method uses a multiscale strategy, all maps derived from the reference segmentation F used for a metric, F_i and G_i, have to be downsampled. We apply a Gaussian filter with $\sigma = 1$ and we downsample the map. This is equivalent to applying a low-pass filter, avoiding aliasing issues.

Initialization and optimization process

The process is iterative, and proceeds from the coarse scale S_1 up to the fine scale S_4. For each step, the current input segmentation map is the output of the previous step (possibly up-sampled, if we switch between S_i and S_{i+1}). The only explicit initialization is then required for the very first step of the process. At this stage, we simply consider a three-layer nested sphere model, with a central simply connected full sphere of label α surrounded by a first hollow sphere of label β and finally a second hollow sphere of label γ.

At each step of the optimization process, we consider either the metric (M_1 or M_2). In order to make M_1 decrease, we build a map that defines, for each point x and each possible relabelling $\ell_1 \to \ell_2$ (with ℓ_1 the current label at x), the associated benefit with respect to M_1, namely $\|\ell_2 - F_i(x)\|_2 - \|\ell_1 - F_i(x)\|_2$. Then, we iteratively carry out the relabelling of (simple) points with the maximal (non-negative) benefit, until stability.

In order to make M_2 decrease, we build a map that defines, for each point x and each possible relabelling $\ell_1 \to \ell_2$ (with ℓ_1 the current label at x), the associated benefit with respect to M_2, as $\Delta(x, G_i^{-1}(\ell_2))$ if $2(x, G_i^{-1}(\ell_2)) < \Delta(x, G_i^{-1}(\ell_1))$ and 0 otherwise. Then, we iteratively carry out the relabelling of (simple) points with the maximal benefit, until stability.

Experiments and Results

We present some results computed with the proposed method, for topological correcting both types of inputs:

Algorithm 2 Multilabel, multiscale topology-controlled deformation approach

Require: F: uncorrected segmentation;
T: deformable label image;
N: number of steps;
$\mathcal{P} = \{P_i = (S_i, TM_i, M_i), i = 1 \dots N\}$: parameter set where M_i, S_i and TM_i are the metric and the topological model in i^{th} step respectively
Ensure: T: deformable label image
for $i = 1 \dots N$ **do**
    Find simple points in T regarding S_i and TM_i
    Compute benefits regarding M_i
    while benefits$(x) > 0 \; \forall x \in T$ **do**
        $x \leftarrow$ argmax benefits
        $S(x) \leftarrow$ benefits(x)
        Update simple points regarding S_i and TM_i
        Update benefits regarding M_i
    end while
    if $TM_i \neq TM_{i+1}$ **then**
        Upsample T by a factor 2^3
    end if
end for

- Fuzzy segmentations provided by our proposed multi-atlas segmentation method IMAPA;
- Hard segmentations given by the reference segmentations from dHCP dataset[1] [Makropoulos et al., 2017].

An example of such map F obtained from an MR image is illustrated in Figure 4.5.

Here, we carried out a 5 step iterative procedure with the meta-parameters summarized in Table 4.1. We considered each label (i.e. CSF, WM and GM) 6-adjacent and the rest 26-adjacent. This choice was made for imposing a minimal thickness to the cortex. The other two labels were defined 6-adjacent for algorithm simplicity. As explained in Section 4.2.3, we initially apply the topology TM_1 that corresponds to two concentric spheres. In order to adapt the topological model in finer scales, we introduce the brainstem segmentation as a prior for locally applying the TM_2. Since we know that the brainstem does not come in contact with the cortex, it is a good candidate prior to locally open the sphere of cortex.

In addition, we present a quantitative evaluation of the segmentation with the Dice score (Table 4.2).

In order to check the topology preservation, we compute before and after each step (in particular when the topology model is changed) the Betti numbers of each label (Table 4.3). The three Betti numbers for a specific label are defined as:

- b_0, number of connected components
- b_1, number of tunnels
- b_2, number of holes

[1] `http://www.developingconnectome.org`

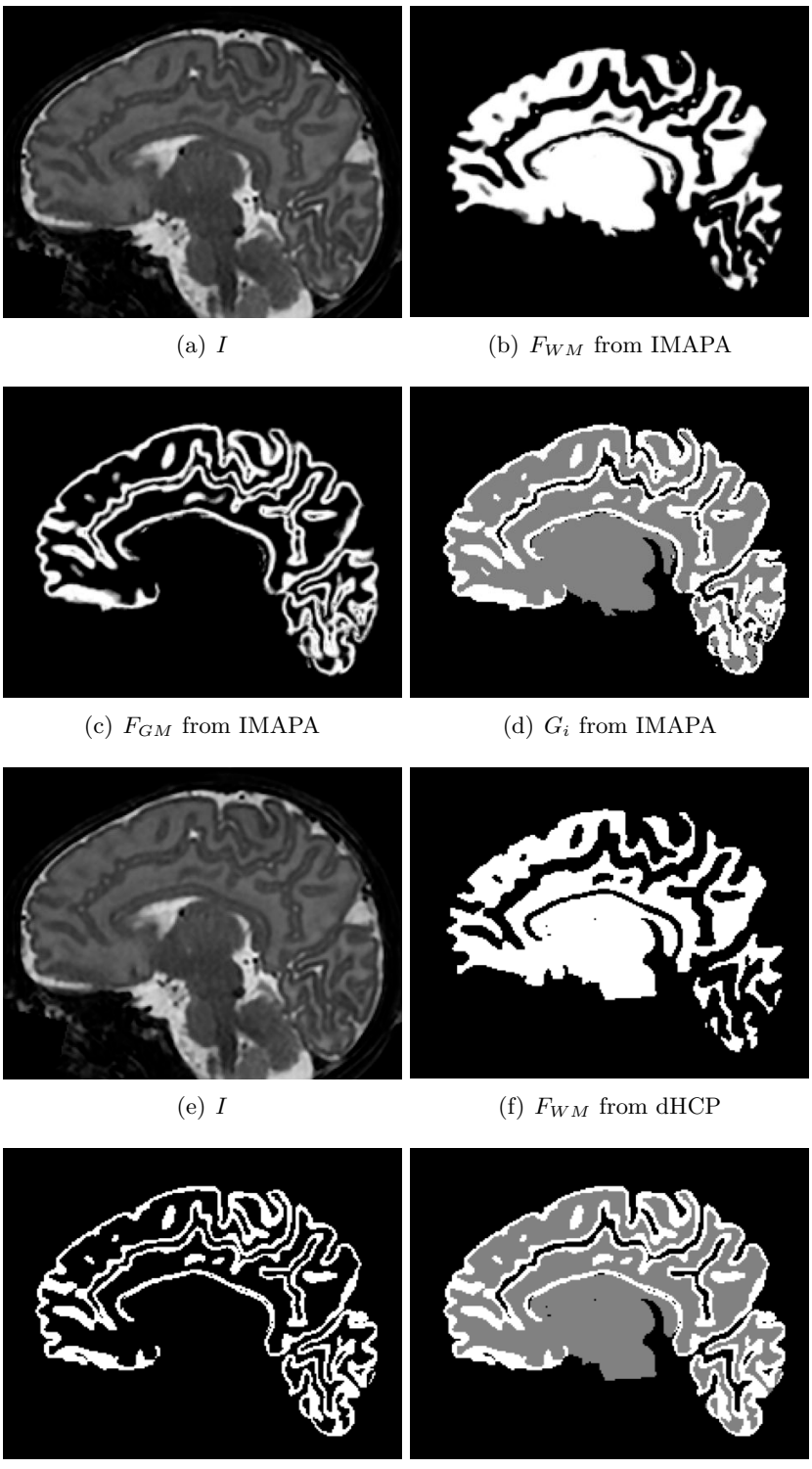

(a) I (b) F_{WM} from IMAPA

(c) F_{GM} from IMAPA (d) G_i from IMAPA

(e) I (f) F_{WM} from dHCP

(g) F_{GM} from dHCP (h) G_i from dHCP

Figure 4.5 – (a) & (e) MR image. (b) & (f) The WM map. (c) & (g) The GM map. (d) & (h) Crisp classification map (WM in grey; GM in white; CSF + background in black). (a–d) Data from fuzzy maps (IMAPA). (e–h) Data from hard maps (dHCP). (a–h) Sagittal slices.

Table 4.1 – Meta-parameters for the successive steps of the process. Four scales are considered where S_i is the upsampled version of S_{i-1} by a factor of 2, being S_4 the scale of the reference image. The topological model TM_1 is applied for coarse and intermediate scales whereas TM_2 is locally introduced to the fine scales in order to open the GM, which is initially a closed surface. The metric M_2 corresponds to the distance-based metric.

Step	Scale	Topology	Metric
1	S_1	TM_1	M_2
2	S_2	TM_1	M_2
3	S_3	TM_1	M_2
4	S_3	TM_1 & TM_2	M_2
5	S_4	TM_1 & TM_2	M_2

Table 4.2 – Dice scores of the reference input reference segmentations F and the result T for each label (GM, WM and CSF).

Subject	F input	Label	Dice of F	Dice of T
#1	IMAPA	CSF	0.996	0.995
		WM	0.979	0.979
		GM	0.894	0.889
	dHCP	CSF	1.0	1.0
		WM	1.0	0.998
		GM	1.0	0.991
#2	IMAPA	CSF	0.995	0.995
		WM	0.974	0.976
		GM	0.903	0.895
	dHCP	CSF	1.0	1.0
		WM	1.0	0.998
		GM	1.0	0.994

From a computational point of view, b_0 and b_2 are determined with a relative simplicity given a label 26-connected. Both numbers, b_0 and b_2, are determined by counting the connected components of the label in 26-adjacency and its complementary in 6-adjacency, respectively. However, the extraction of number of tunnels b_1 has an additional difficulty: it needs the Euler characteristic (notated χ) in order to be rapidly computed. In the context of topology and Khalimsky grid, there are two different approaches in order to obtain the Euler characteristic, namely

$$\chi = \sum_{i=0}^{n} (-1)^i k_i \tag{4.6}$$

where n is the dimension of the image and k_i is number of n-simplices in a Khalimsky's cubic complex, e.g. k_0 corresponds to the number of points (0-dimension), k_1 to the number of lines (1-dimension), and so on. This equation provides the value of Euler characteristic of a 3D image by computing $k_0 - k_1 + k_2 - k_3$. With this in mind, we can use a second definition according to the Betti numbers, i.e.:

$$\chi = \sum_{i=0}^{n-1} (-1)^i b_i \tag{4.7}$$

Table 4.3 – Betti numbers (b_0, b_1 and b_2) at the end of a step depending on the topological model chosen. Topological models are used to preserve the topology of every label (TM_1) or to relax the topological constraints for a particular label (TM_2) depending on the scales (see Section 4.2.3 for more details). In addition, the Betti numbers of the crisp classification map from different reference segmentation are presented (IMAPA and dHCP).

Topological Model	Label	b_0	b_1	b_2
Result with TM_1	CSF	1	1	0
	WM	1	0	0
	GM	1	0	1
Result with $TM_1 + TM_2$	CSF	1	1	0
	WM	1	0	0
	GM	1	0	0
G_i from IMAPA	CSF	6080	1236	8
	WM	263	121	15
	GM	87	1742	158
G_i from dHCP	CSF	1102	537	3
	WM	77	100	28
	GM	64	2433	181

If we reformulate this equation, we can obtain the second Betti number given a 3D image:

$$b_1 = b_0 + b_2 - \chi = b_0 + b_2 - k_0 + k_1 - k_2 + k_3 \tag{4.8}$$

This measurement is valid for a 26-connected label. In the case of 6-connected label, the computation is not valid due to the need of a close surface in the Khalimsky grid in order to compute the Euler characteristic. Fortunately, its complementary is 26-connected, thus we use it for the Betti number acquisition. The equivalence between the 6-connected object and its complementary is:

- b_0, number of holes of the complementary in 6-adjacency
- b_1, number of tunnels of the complementary
- b_2, number of connected components the label in 26-adjacency minus ones

The initial images I are defined on $\Omega = [\![0, 291]\!] \times [\![0, 291]\!] \times [\![0, 203]\!]$. We use as scale factor $k = 2$. The successive segmentation maps (and the associated classification maps F_3, F_2 and F_1) are then defined on $\Gamma_3 = [\![0, 291]\!] \times [\![0, 291]\!] \times [\![0, 203]\!]$, $\Gamma_2 = [\![0, 145]\!] \times [\![0, 145]\!] \times [\![0, 101]\!]$, and $\Gamma_1 = [\![0, 72]\!] \times [\![0, 72]\!] \times [\![0, 50]\!]$, respectively, i.e. with $|\Gamma_3| \simeq 1, 7.10^7$, $|\Gamma_2| \simeq 2, 2.10^6$ and $|\Gamma_1| \simeq 2, 7.10^5$.

An example of the successive steps of the topological transformation process is illustrated in Figure 4.6. One can observe the progressive convergence of the model toward the classification map, whereas controlling the topology of the segmentation, in particular on the cortex (preserved on the upper part of the encephalus), whereas the GM is relevantly removed on the lower part, in accordance with the initial classification map and with the topological model.

A 3D mesh visualization of the resulting map T is illustrated in Figure 4.8, qualitatively emphasizing the topological correctness of the result. These results were obtained using meshing tools from BrainVISA software[2] [Geffroy et al., 2011].

[2] `http://brainvisa.info`

Finally, some examples of multilabel vs. monolabel, and multiscale vs. monoscale strategies for topological correction are proposed in Figure 4.9.

Discussion

Qualitative results (Figure 4.6) show that most of the topological defects were corrected, in particular the discontinuities in cortical surface (i.e. holes). The application of surface mesh generation (Figure 4.8) confirms the enhancement in the topology since the post-processing correction fills holes at gyrus and fits the depth of sulcus. This improvement costs a slight loss in quantification results (Table 4.2), which was expected since the reference segmentation has also topological defects. Even though the Dice score in this context does not have the same purpose as an automatic segmentation algorithm evaluation (such as in Chapter 2), it still remains close.

In addition, the comparison between the multilabel versus the monolabel and the multiscale versus monoscale paradigms ensures the main contributions of our proposed algorithm (Figure 4.9). On the one hand, the monolabel strategy for the cortex presents less fit of the surface to the real cortex. The multilabel approach shows a more complex shape, going deep into the sulcus and gyrus. On the other hand, the monoscale result shows more and thicker handles between the cortex foldings. This fact emphasizes the local minima that could be avoided with the multiscale strategy.

The proposed algorithm present two different metrics (Section 4.3). However, in the results that we show, the metric distance M_2 is the unique used (Table 4.1). The reason is because M_1, the metric that relies on the classification error, does not have the competence of guiding labels toward their reference. On the other hand, M_2 provides exactly the distance of the closest point for each label. M_1 can be applied after a step of M_2 without changing the scale, but there is no significant changes due to the quantity reduction of simple points.

However, we still observe the existence of some thin tunnels (such as "little bridges") that appear in another class (Figures (e)(f)(g) from 4.6 and 4.7). Analysing these structures, they are composed of non-simple points. This dismiss the possibility of a optimization problem from the cost function. It could be related to the fact that the topological model is not well suited due to handles in cortical foldings, which complicates the shape deformation. These errors seem to not affect the surface mesh generation (Figure 4.8). They motivate, however, further experiments in order to understand their genesis, and more efficiently ensure their non-appearance.

Moreover, the topological correction provides an improvement for surface mesh generation. Mesh generator algorithms often require a binary segmentation, forcing to apply a thresholding step that may increase or get worse topological errors. The proposed post-processing correction accepts binary or fuzzy segmentations as input. Therefore, another way to define the proposed approach is a smart binarization of a segmentation, correcting its topology and enhancing its properties in order to generate a mesh.

Conclusion

This preliminary study provides some promising results that prove the relevance of using the multilabel topological framework proposed in [Mazo et al., 2012b] for developing a multiscale, topological modeling of the cerebral structures, allowing one to either

preserve or relax topological constraints over the power lattice of a set of elementary semantic labels.

In particular, this framework can be efficiently used for carrying out multiscale, topology-controlled deformation of label maps based on the concept of simple points, here in the context of topological correction of fuzzy segmentation maps computed beforehand.

Among numerous perspective works, we will further investigate (1) more sophisticated metrics for guiding the deformation process (e.g. adding a regularization metric with geometrical prior such as the cortical thickness); (2) the possibility to carry out deformation processes at a superpixel resolution and/or to use cubical complex models [Mazo et al., 2012a] for topological modeling; and (3) a richer modeling of the brain with more anatomical structures, e.g. for atlas-based segmentation. In addition, we need to investigate more about the bridge errors by applying the three propositions.

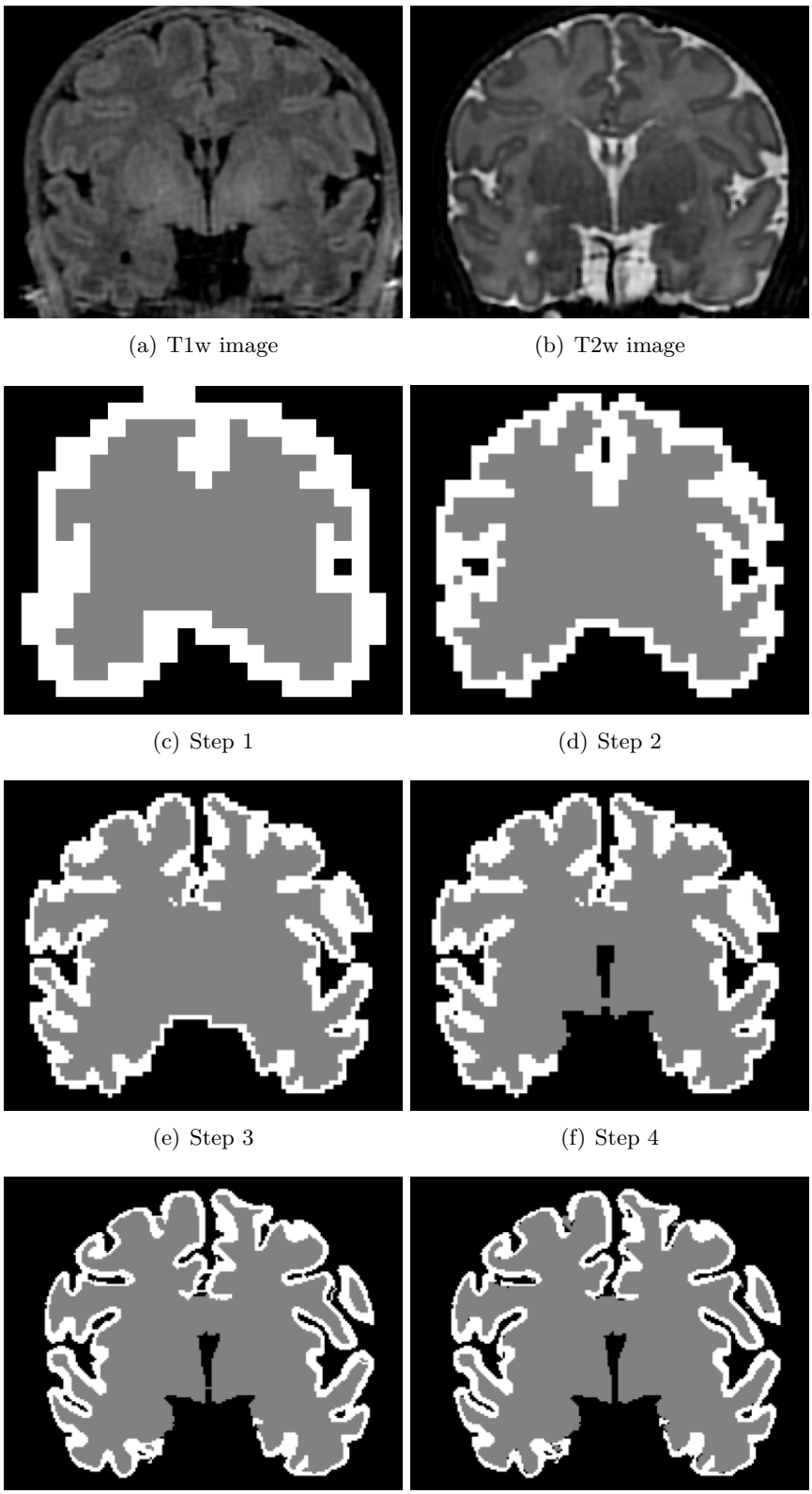

(a) T1w image (b) T2w image

(c) Step 1 (d) Step 2

(e) Step 3 (f) Step 4

(g) Result T (h) G_i

Figure 4.6 – (b–f) Intermediate results obtained by the successive steps of the process (see Table 4.1). (g) Final segmentation map. (h) Crisp classification map (see also Figure 4.5(d)) from fuzzy segmentation maps (IMAPA) used as reference for guiding the process.

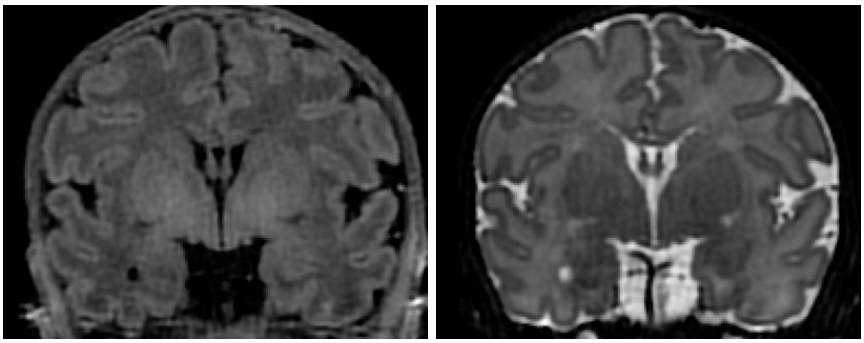

(a) T1w image (b) T2w image

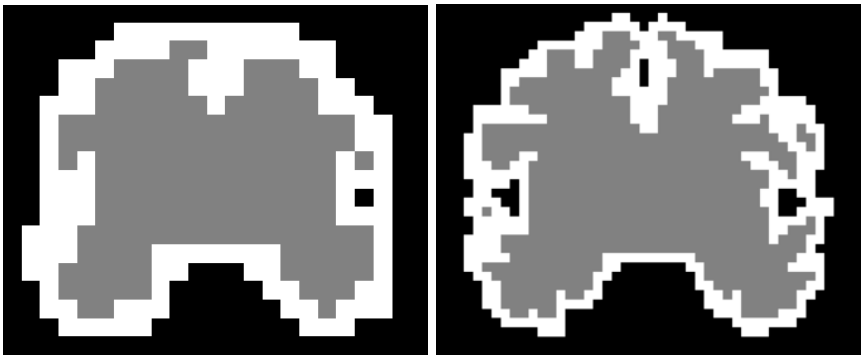

(c) Step 1 (d) Step 2

(e) Step 3 (f) Step 4

(g) Result T (h) G_i

Figure 4.7 – Item to Figure 4.6 with the same subject changing the reference segmentation to the dHCP dataset.

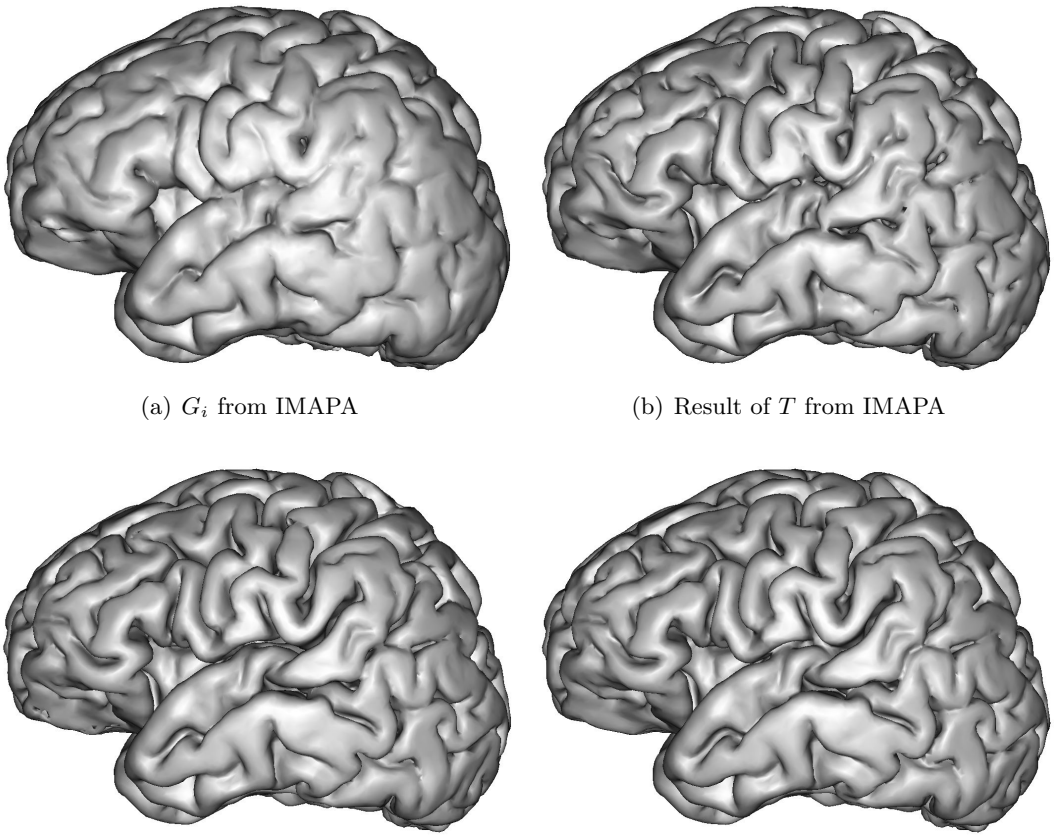

(a) G_i from IMAPA

(b) Result of T from IMAPA

(c) G_i from dHCP

(d) Result of T from dHCP

Figure 4.8 – Surface meshes generated from crisp classification map from reference segmentation G_i (left) and the final topological segmentation map T (right).

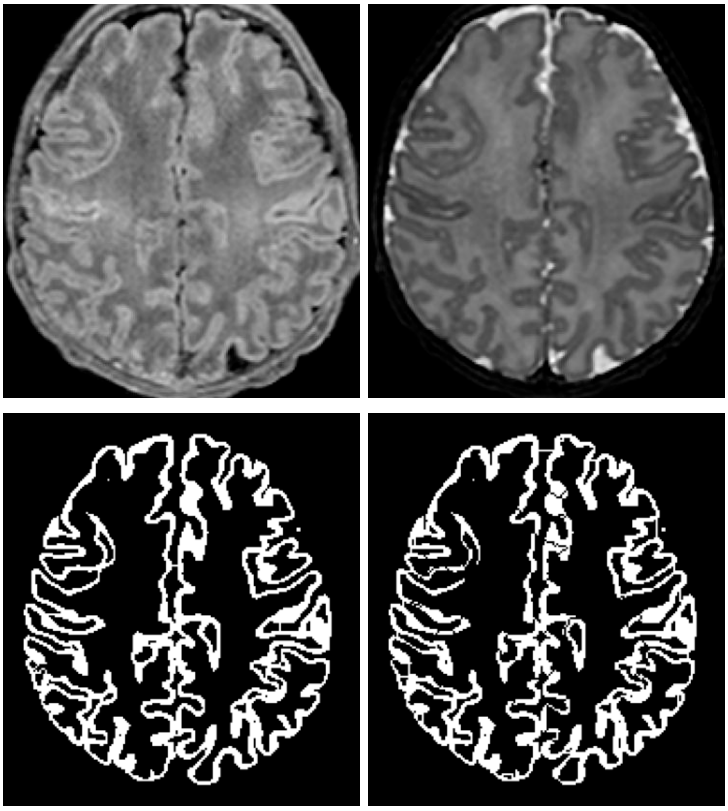

(a) Multilabel strategy (b) Monolabel strategy

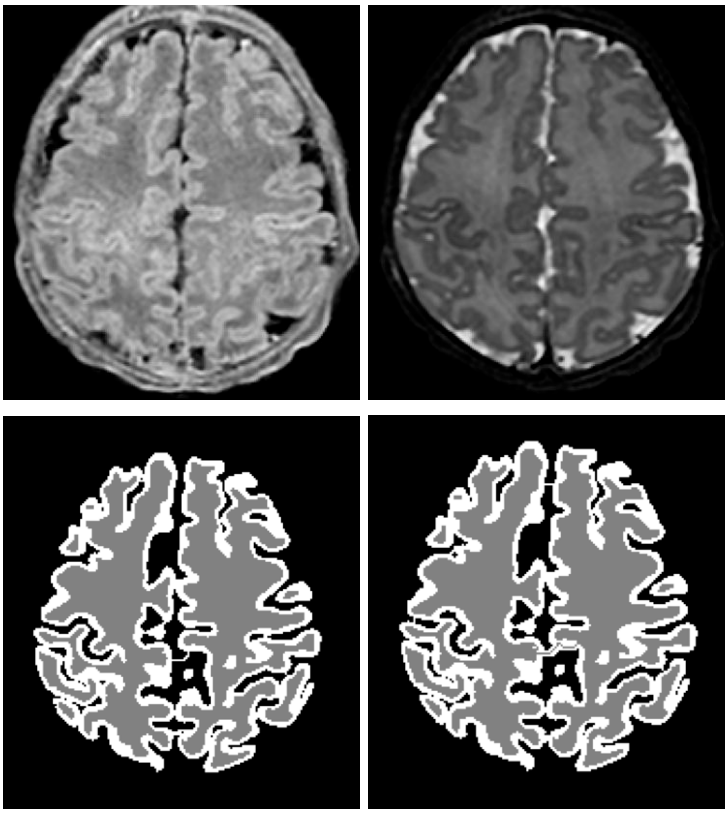

(c) Multiscale strategy (d) Monoscale strategy

Figure 4.9 – A comparison between monolabel vs. multilabel (second row) and monoscale vs. multiscale (fourth row) strategies. The T1w (left) and T2w (right) images are presented in each comparison.

Chapter 5

Conclusion and Perspectives

Conclusion

The aim of this thesis is to provide an efficient fully-automatic method that segments the cortical surface in neonatal brain MR images. Two main contributions are presented: *i)* a multi-atlas patch-based approach for segmenting the cortex and *ii)* a post-processing topology-preserving algorithm for refining the cortical segmentation. These contributions are motivated by the fact that the neonatal brain MR images have a low contrast and a strong partial volume effect. Moreover, most of the existing methods for brain MRI are focused on the adult, hampering their direct applicability due to tissue maturation. In addition, the application of these methods in clinical neonatal datasets is evaluated. This data is commonly characterized by a 3D anisotropic resolution, which adds more difficulty to the challenging segmentation task.

The first contribution of this thesis, presented in Chapter 2, consists of a fully-automatic segmentation method using a supervised learning approach. This method fuses two techniques: the multi-atlas segmentation (MAS) methods, which use an anatomical prior of the structures to be segmented, and the non-local approaches, which provide guarantees of robustness against registration errors and noise. Multi-atlas segmentation approaches follow three steps: registration, label propagation and label fu-

sion. The contribution of our approach lies on the third step, the label fusion, where the combination of labels was optimized. Label fusion is usually performed as a linear regression of the registered examples. At this point, we focus on finding a strategy that optimizes this linear regression by determining the set of weights through a training step. The use of patches in a window of search for this regression contributes to increase the robustness to errors during the registration process. We introduce a framework for optimizing these weights and a regularization term that involves the segmentation space for guiding the result toward a finer structure.

This approach is tested in research-oriented MRI, i.e. images acquired with special emphasis on the quality such as isotropic resolution or high contrast-to-noise ratio. However, this is not the case in clinical datasets, which are acquired with minimal quality conditions in order to certify a diagnosis. This thesis proposes an evaluation of a pipeline for segmenting neonatal cortex in clinical MR images (Chapter 3). This pipeline is based on two main steps: *i)* reconstruction of the high-resolution image and *ii)* segmentation the cortex. Different methods are tested for this purpose based on super-resolution methods and multi-atlas segmentation approaches. The results emphasize the need for developing efficient segmentation methods dedicated to clinical data (e.g. [Pham et al., 2019]), even for manual segmentation carried out by an clinical expert.

The second contribution is oriented toward refining segmentations by correcting a common error in cortical segmentation: topological errors (i.e., holes or handles). The proposed method is based on a topology-preserving label deformation mainly relying on two paradigms: multilabel and multiscale. Multilabel strategy allows various regions of distinct semantics to compete versus the others, for their own growing that helps their deformation to attempt complex shapes. This fact is particularly interesting for the cortex, which presents specificities in terms of finding and thickness that tend to hamper the structural fitting of sulcus and gyrus. In addition, it gives the possibility to relax locally the topological model, which is usually simplified by a sphere. On the other hand, the notion of multiscale gives the opportunity to avoid local minima of the cost function. Moreover, it allows the algorithm to reduce iterations, leading to a gain in terms of time consumption.

Perspectives

Generalization of the contributions

Although contributions were focused on the cortex segmentation in neonatal MR images, the proposed tools are essentially more generic.

The first contribution, IMAPA algorithm, is applied to segment the cortex in a T2w MRI images. This algorithm is a generic multi-atlas segmentation method that only requires that the used atlas set presents similar properties in terms of intensity and labels with respect to the target image to be segmented. Thus it can also segment any other structures by modifying labels of the atlas set, for example white matter (WM) or cerebospinal fluid (CSF). Furthermore, if we replace the labels to another MRI modality, we can achieve to synthesize the new modality of the target image. An example of both approaches are shown in Figure 5.1.

Apart from tissue segmentation, the literature emphasizes efficient applications of multi-atlas based methods for segmenting lesions or pathologies [Bach Cuadra et al., 2004, Cordier et al., 2016]. Therefore, IMAPA algorithm could be reoriented in order

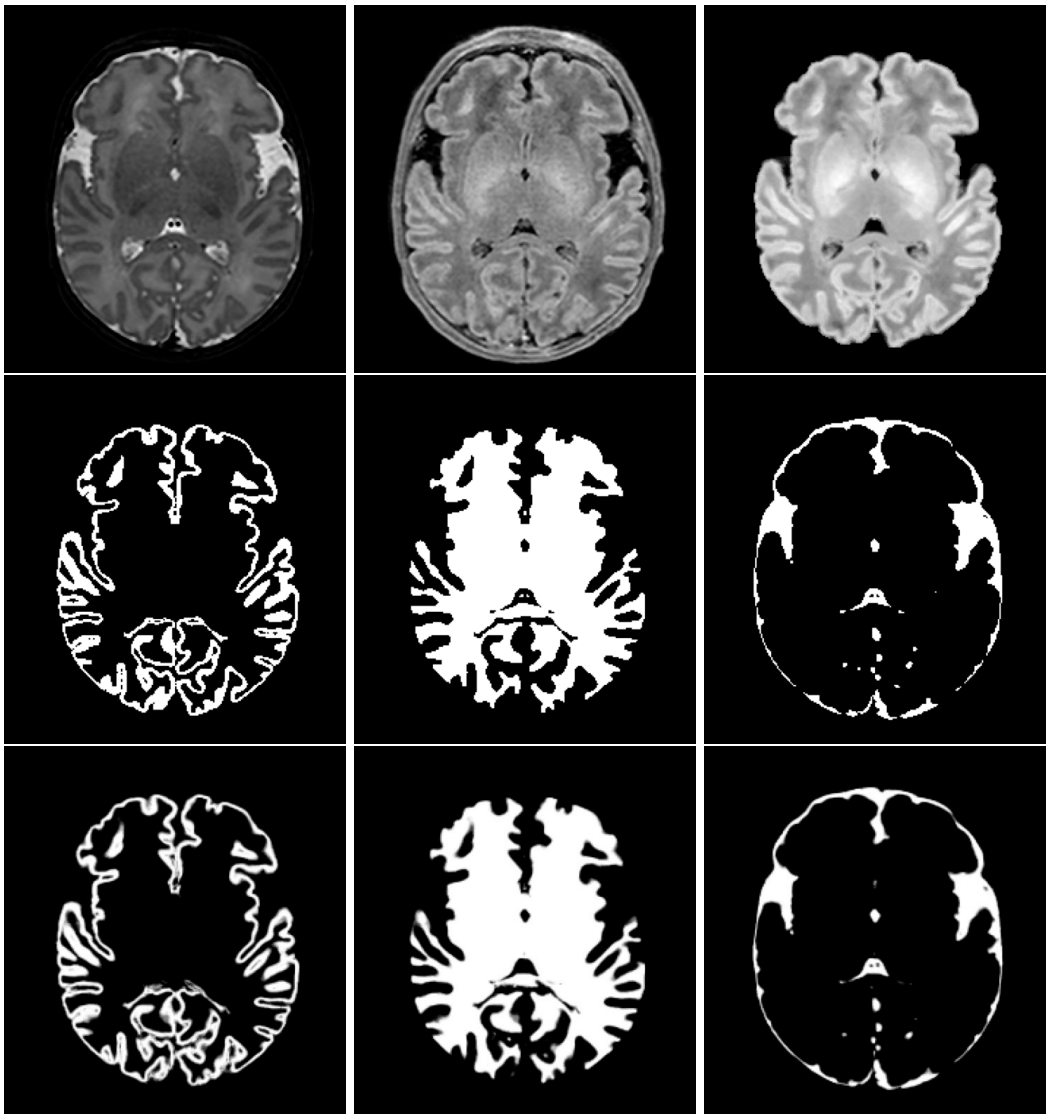

Figure 5.1 – Application of IMAPA in a subject of dHCP dataset for segmenting different brain structures. First row presents the original T2w and T1w MR images with the synthesis of T1w at the right. Second row introduces the reference segmentations of the cortex, WM and CSF, from left to right. In last row, we expose the results of different segmentations performed by IMAPA.

to locate affected regions by fusion of different strategies (e.g. a multiscale approach [Cordier et al., 2016]).

Another challenging task is to apply these methods to fetal datasets, which share most of the problems that the newborn exhibit against the adult, with main differences on the quality of the acquisition such as motion artifacts or 3D reconstruction using several 2D acquisitions [Benkarim et al., 2017b]. In addition, the strong anisotropic resolution makes the reconstruction of the isotropic resolution a mandatory task as a preprocessing step to segmentation. This lets the evaluation of pipelines such in Chapter 3 to be limited to the research-oriented fetal datasets.

Finally, a second contribution could be applied to segment other structures by introducing the appropriate parameter settings (i.e. number of scales, topology model, etc.). Indeed, the main inputs of the post-processing algorithm are a reference segmentation and the initial topological properties of the labels; thus it can be applied in any segmentation. For instance, since it does not require a ground truth to obtain a correction, it could be incorporated to the end of a manual segmentation task so that the results could be supervised by the same expert.

Enhancing label fusion

MAS methods based on non-local approaches, such as IMAPA, are characterized by the search of similar patches in a neighborhood window. The degree of similarity determines the weight value associated to a given patch from the atlas set. Thus "good" examples will have high weight values whereas "bad" examples will have low values. However, in practice there is a huge quantity of bad examples in proportion to good examples, introducing a bias in the estimation [Kervrann and Boulanger, 2008, Duval et al., 2011]. In IMAPA we use a K-nearest neighbors (KNN) strategy in order to reduce bad examples. Alternatively, in order to keep a satisfactory good-bad example rate, we can increase the number of good examples, for instance warping patches in order to increase the matching level. In [Prima and Commowick, 2013], the authors described the interest of leveraging the symmetry of the brain in order to increase the variability of examples. Rotating the patches to a particular orientation will increase the good examples, enhancing the quality of the estimation. However, an evaluation of the interpolation error during the patch warping against the increase of good candidates will be required. In addition, such process would require a much higher computational cost. Another strategy to be studied would be to adapt the patch shape according to their matching in the target image [Faisan et al., 2012].

Deep learning solutions

Pipelines that combine super-resolution and multi-atlas segmentation still have to be improved. There exist promising alternatives similar to these configurations based on deep learning solutions. For instance in [Pham et al., 2019], a generative adversarial network (GAN) is presented, which simultaneously reconstruct the high-resolution image and segment the cortex in neonatal clinical MR images. The results show a qualitative improvement in both modalities (Figure 5.2), attempting a high level of detail for the reconstructed T2w MR image and obtaining finer structural cortex segmentation, qualitatively better than the manual segmentation provided by clinical experts. Moreover, the proposed MAS method (IMAPA) can segment or synthesize depending on the input labels of the atlas set. In this context, if the atlas set consists of pairs with a low-resolution (LR) MR image as intensity image and its corresponding high-resolution as

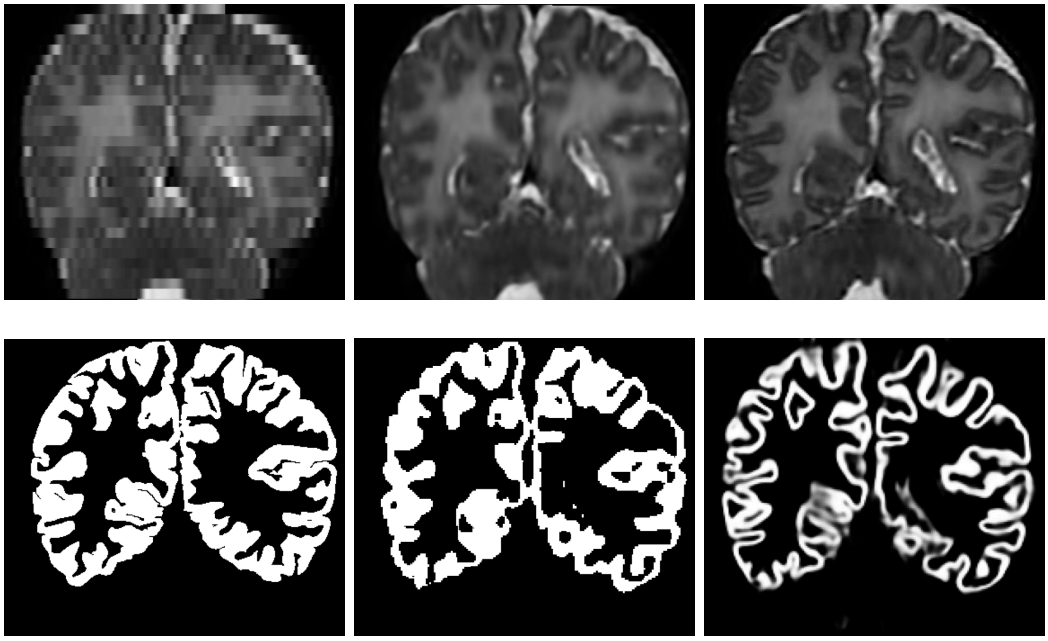

Figure 5.2 – A visual comparison between the best result of our evaluation pipeline in terms of Dice and the GAN results. First column shows the original data of subject #1 from MAIA dataset (T2w and manual segmentation), second column the reconstruct HR T2w image and segmentation as a result of apply SRReCNN and DrawEM algorithms respectively. Last column presents the GAN method [Pham et al., 2019].

a label, we can achieve the HR reconstruction of the target image as a super-resolution method. Furthermore, the notion of mix patch used by IMAPA (a concatenation of patches from intensity and label images) can be extend to a larger structure: a mix of three patches coming from LR image, and two label images: HR image and segmentation map. An evaluation of this application of IMAPA inspired by the simultaneous HR reconstruction and cortex segmentation could be an interesting track.

Beyond the deep learning approaches for brain segmentation purpose, Huo et al. [Huo et al., 2019] present a combination of conventional multi-atlas segmentation (MAS) approaches with 3D convolutional neural network (CNN) methods for segmenting different brain subparts. In this work, their results show a significant improvement using this combination of methods. This encourages to follow this track in future works.

Toward high-resolution segmentation maps

Among the multiple parameters used in the proposed topological correction algorithm, the selection and number of scales parameters need a deeper understanding of their influence on the deformation. In particular, the multiscale strategy stops at the reference segmentation scale, where handles are difficult to correct. Thus, studying the effects of introducing a higher resolution in order to carry out the deformation processes would remain an interest track. A preliminary result is shown in Figure 5.3

Cortical thickness

One of the most relevant factors that make the cortical segmentation a challenging task is its low thickness. As a consequence, discontinuities in the cortex segmentation

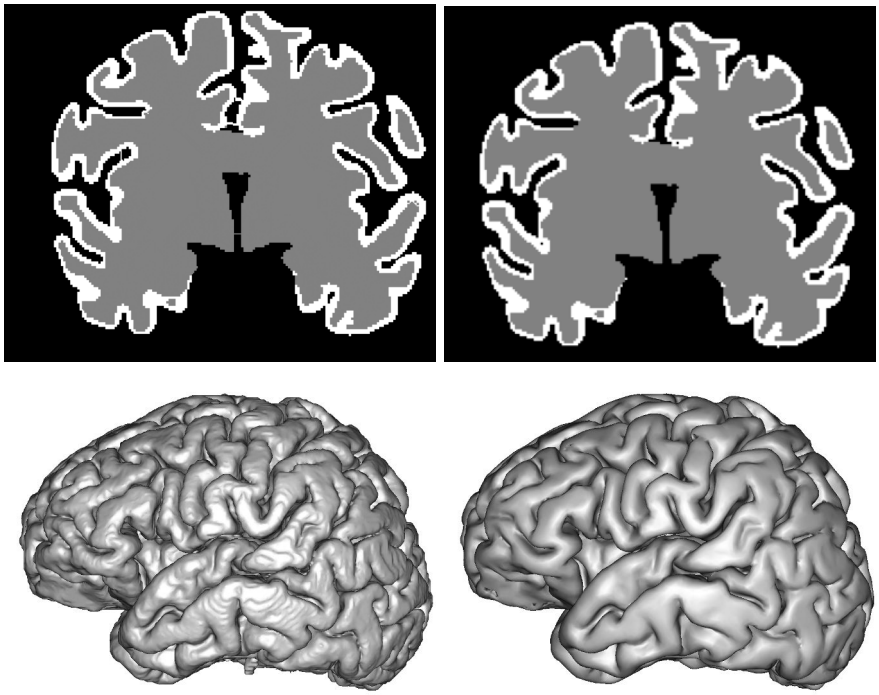

(a) Result at ref scale (b) Reference seg

Figure 5.3 – Preliminary result for a higher scale than the reference segmentation using a subject from dHCP dataset. The result in higher scale (in left) increased the resolution of the reference segmentation (in right) by a factor of 2.

estimation appear, where in Chapter 4 a method is introduced to correct them. This algorithm shows that the topological model can be fitted by the introduction of priors, such as the use of brainstem in order to open the cortex label, initially modeled as close a sphere. Therefore, a future direction could be to leverage the cortical thickness to enrich the metric for guiding the deformation. This integration could be done with a regularization term that depends on this geometrical prior. However, the computation of an accurate thickness map remains an open question in research. In Figure 5.4 we show two existing methods for computing the thickness map. These methods are based on the registration of the WM to the GM segmentation (ANTS[1]) [Das et al., 2009] and on Laplace profiles by using the neighbor segmentation of the GM (i.e. CSF and WM) [Makki et al., 2019].

[1] `http://stnava.github.io/ANTs`

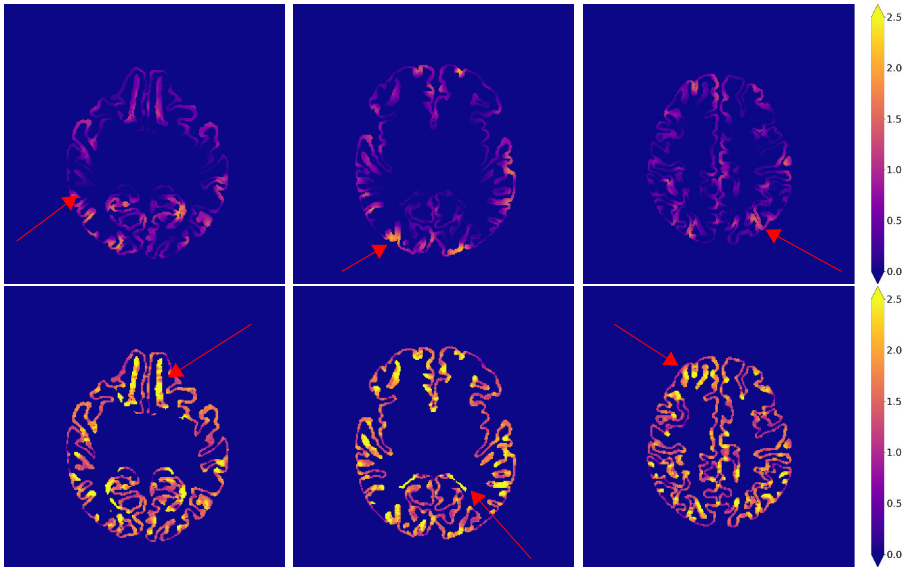

Figure 5.4 – Examples of cortical thickness map computed by two different methods. The first row corresponds to [Das et al., 2009] and the second row to [Makki et al., 2019]. Note that the measures of the thickness are in millimeters and the voxel resolution is 0.5×0.5 mm. Red arrows indicate some areas where the thickness measurement fails.

Appendix A

Correction of intensity irregularities on MAIA dataset

Introduction

The ANR MAIA project provided to this thesis an important amount of MR images coming from a clinical environment at hospital of Reims, focused on the preterm infant. Since this dataset was not processed, the images remain raw. Thus, we observe some irregularities of the intensity levels of the MRI concerning isolated slices. These slices show an added bias in mean intensity, leading to hyperintensity on such slices (Figure A.1).

Correction

In order to correct these intensity errors, we have tested two different methods of intensity normalization:

- intensity normalization, based on the mean and standard deviation;
- approach based on the application of histogram matching (ITK[1]) between the normal and biased slices.

Since the automatic detection was difficult to perform, the uncorrected slices were selected manually.

[1] `https://itk.org/`

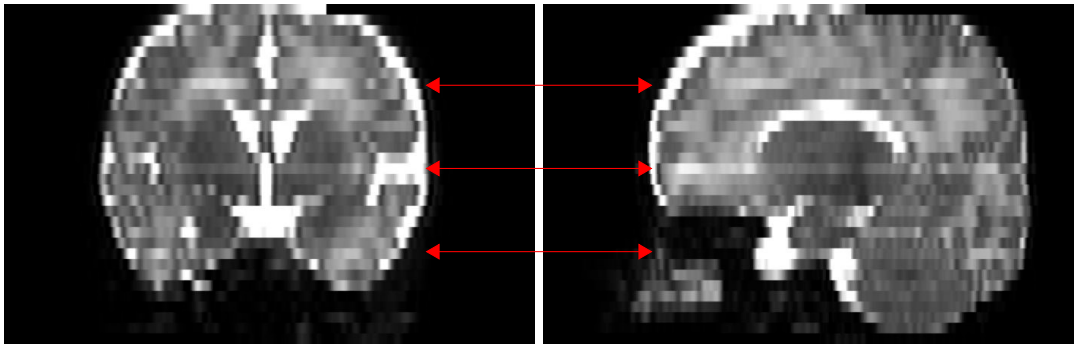

Figure A.1 – Visualization of a subject from MAIA dataset in coronal (left) and sagittal (right) planes. Red arrows indicate the slices affected by the irregularities.

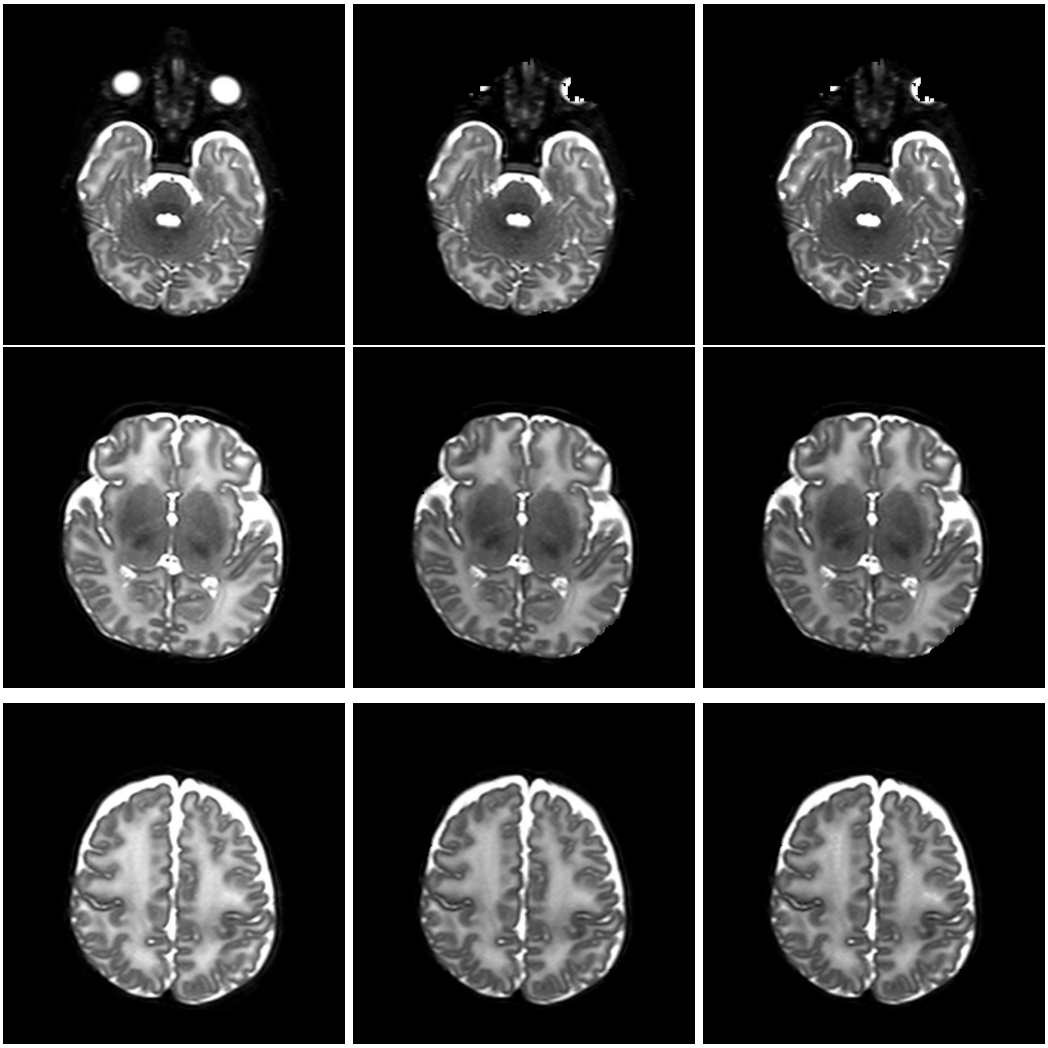

(a) Original (b) Normalization (c) Histogram matching

Figure A.2 – Visualization of the affected slices.

The first method used the mean and the standard deviation of the whole image. Let x be a point belonging to the affected slice, we define its correction $\hat{x}$ as follows

$$\hat{x} = \left(\frac{x - \mu_1}{\sigma_1} \times \sigma_2 \right) + \mu_2$$

where μ_1 and σ_1 are the mean and standard deviation of the affected slice respectively, and μ_2 and σ_2 correspond to the mean and standard deviation of neighbor slices of the affected slice, respectively. The last parameters are computed from the average image of the neighbor slices.

Both correction assume that for a biased slice j, its neighbor slices $j-1$ and $j+1$ are normal.

Results

We present different visualisations of the results in order to emphasize the correction and compare the results:

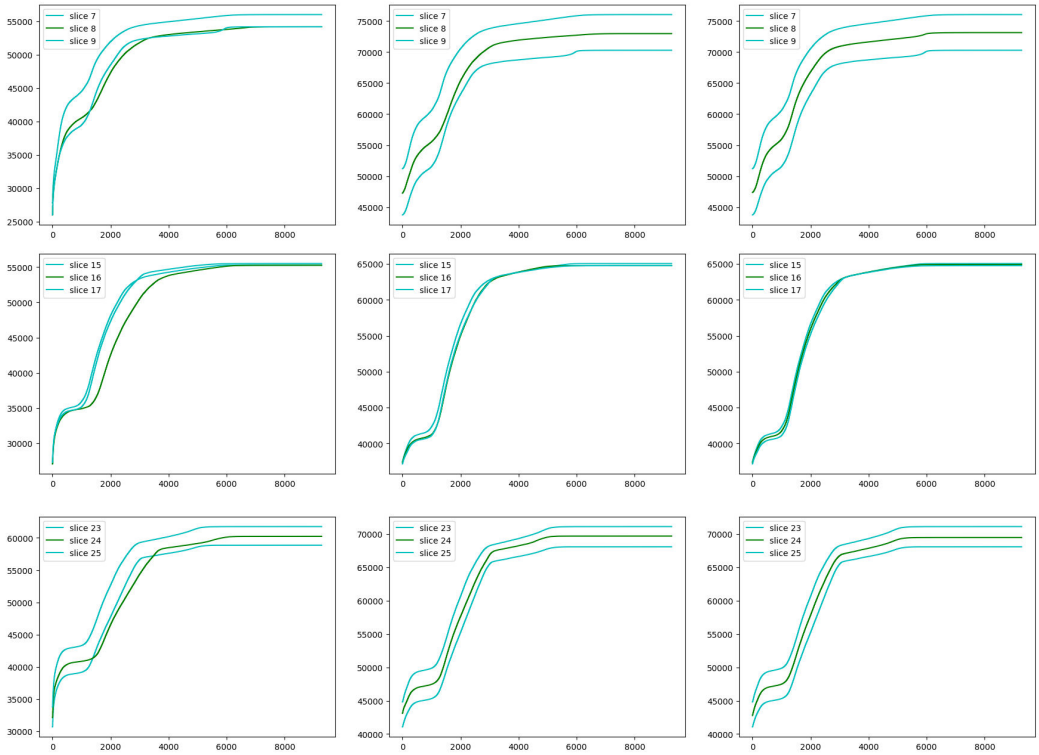

(a) Original (b) Normalization (c) Histogram matching

Figure A.3 – Cumulative histograms of each axial affected slice by the hyperintensities and both neighbor slices.

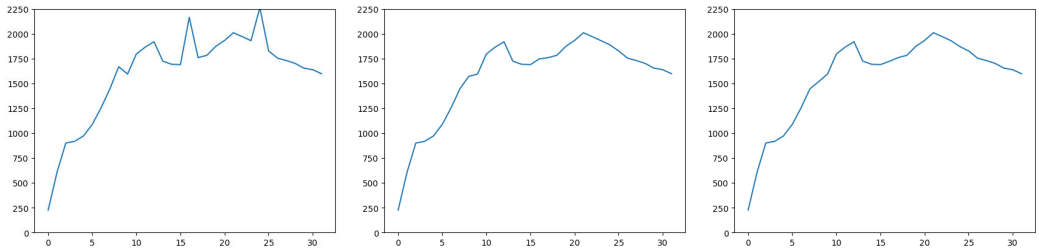

Figure A.4 – The intensity mean (y-axis) per axial slice (x-axis).

- The affected slices with both applied corrections (Figure A.2);
- The profile of cumulative histogram of the affected slice and the neighbours (Figure A.3);
- The intensity mean per slice (Figure A.4);
- Comparative visualization of corrected slice with a local (Figures A.5 and A.6) and with a global point of views (Figures A.7).

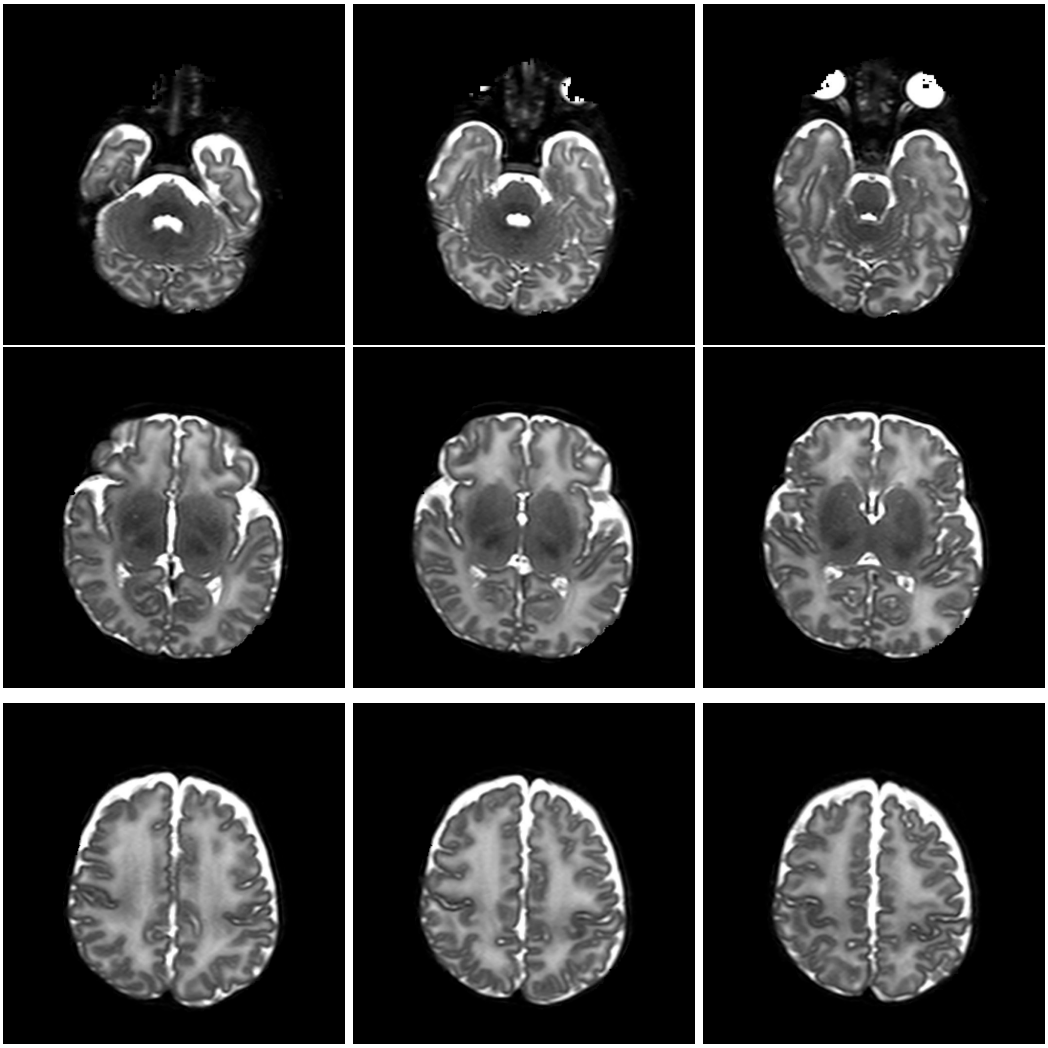

(a) Slice $j-1$ (b) Slice j (c) Slice $j+1$

Figure A.5 – Result of the normalization correction by comparing its neighbor slices.

Conclusion

From a qualitative point-of-view (Figure A.2), both methods can achieve satisfactory results, correcting the bias intensity and leading to a mean that is between its neighbor slices. Observing the cumulative histograms (Figure A.3), the histogram matching method seems to achieve a better performance in terms of intensity profile (i.e. it is located more in the middle of both neighbor slice histograms). However, the normalization intensity method shows a more satisfactory result in terms of visualization (Figures A.5, A.6 and A.7). Thus, this last method was the method chosen for correct the MAIA ANR dataset.

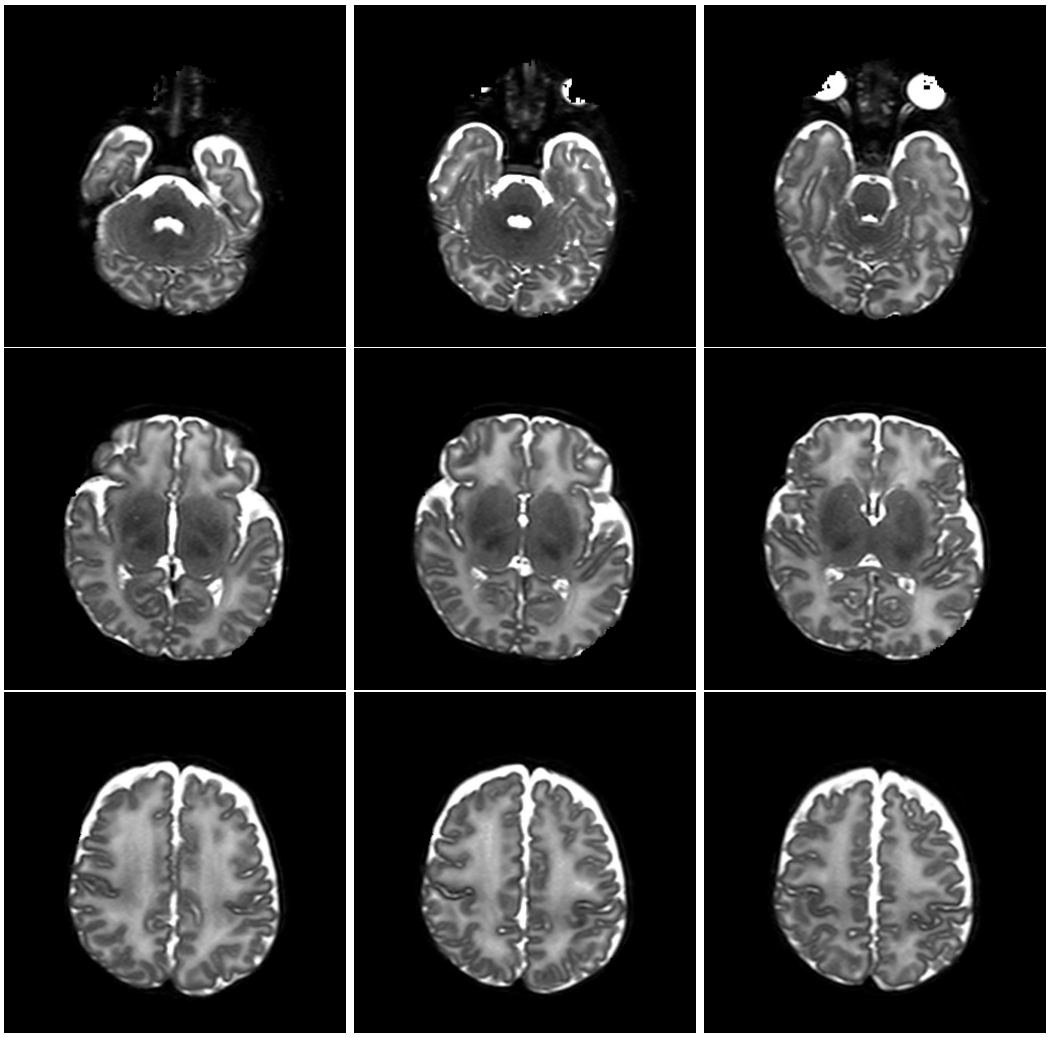

(a) Slice $j-1$ (b) Slice j (c) Slice $j+1$

Figure A.6 – Result of the histogram matching correction by comparing its neighbor slices.

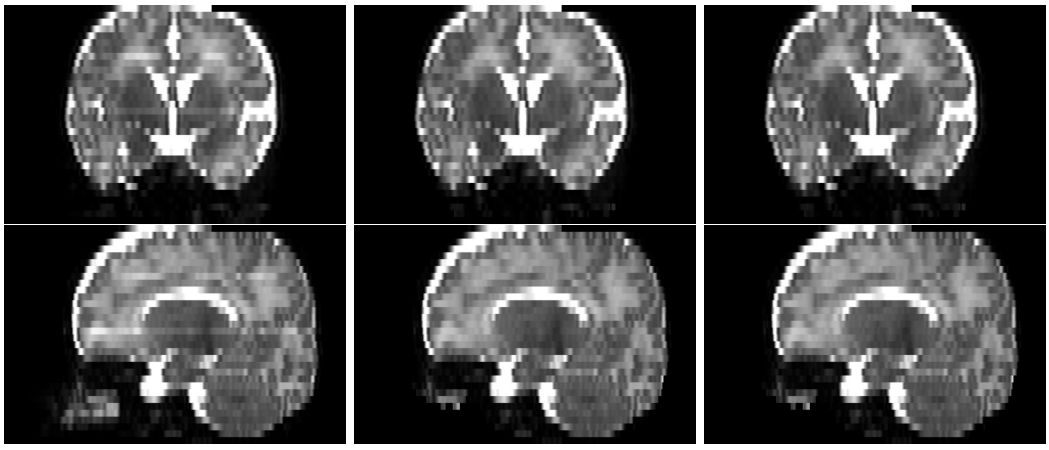

Figure A.7 – Visualization of the original and corrected data in coronal (first row) and sagittal (second row) planes.

Appendix B

Segmentation of brain anatomy: application of IMAPA

Introduction

As discussed in the perspective of this thesis (Chapter 5), the first contribution, IMAPA, can be generalized to segment other structures. The second contribution, the post-processing topological correction, relies on the multilabel paradigm, which results in Chapter 4 show a relevant improvement against a monolabel strategy. This multilabel paradigm requires the segmentation of the CSF and the WM. Thus, IMAPA was applied in order to segment them in the dHCP dataset, as it is presented in Chapter 2.

Results

Similarly to the evaluation of IMAPA in the cortex, we applied it to dHCP dataset. We split the set of 40 subjects to 30 for the atlas and 10 for the test. In Table B.1, we present the mean of Dice score and PSNR from the test set. IMAPA provides a fuzzy segmentation, thus a thresholding of 0.5 was applied in order to compute the Dice score. In Figure B.2, a summary of the segmentation structures and reference segmentation is exposed. In order to perform an evaluation of the behavior of IMAPA through different structures, the previous results from the cortex segmentation are included. Finally, we present the mesh generation of the reference segmentation and the results in Figure B.1.

Conclusion

From a quantitative point-of-view (Table B.1), IMAPA is high-scored (for GM and WM, Dice exceeds 0.9). Qualitatively, the map estimation of the structures are satisfactory. If we observe the CSF, we note that, in this particular dataset, the CSF is especially thin.

Since the WM is a more homogeneous and larger structure, we expected to obtain the highest score. However, this fact is not applied to the cortex, which is larger than the CSF in terms of volume (in this particular dataset) and it obtains the lowest performance in terms of Dice (slight difference) and PSNR (huge difference). Therefore, although the CSF is a finer structure than the cortex, it is better estimated . This highlights the difficulty of segmenting the cortical surface, which does not only rely on the low thickness but also on the complex shape of the cortex folding.

The reference segmentation maps of CSF were very thin with several huge discontinuities in the surface. Thus, their application to the topological correction algorithm

Table B.1 – Dice scores of the reference input segmentations F and the result T for each label (GM, WM and CSF).

Label	Dice Mean	Dice Std	PSNR Mean	PSNR Std
CSF	0.915	0.019	24.12	1.68
WM	0.974	0.006	24.90	0.66
GM	0.887	0.011	21.09	0.39

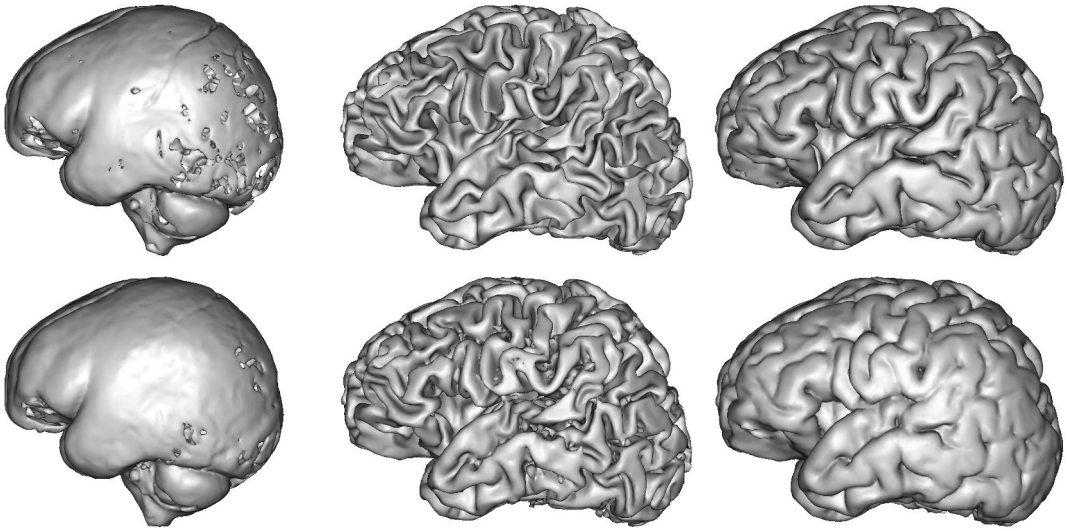

Figure B.1 – Representation of surface meshes generated using reference segmentation (in the first row) and IMAPA results (in the second row). From left to right: the CSF, the WM and the cortex.

was difficult. Finally, we decided to use the background instead of the CSF map from dHCP as the third label in order to leverage the multilabel paradigm.

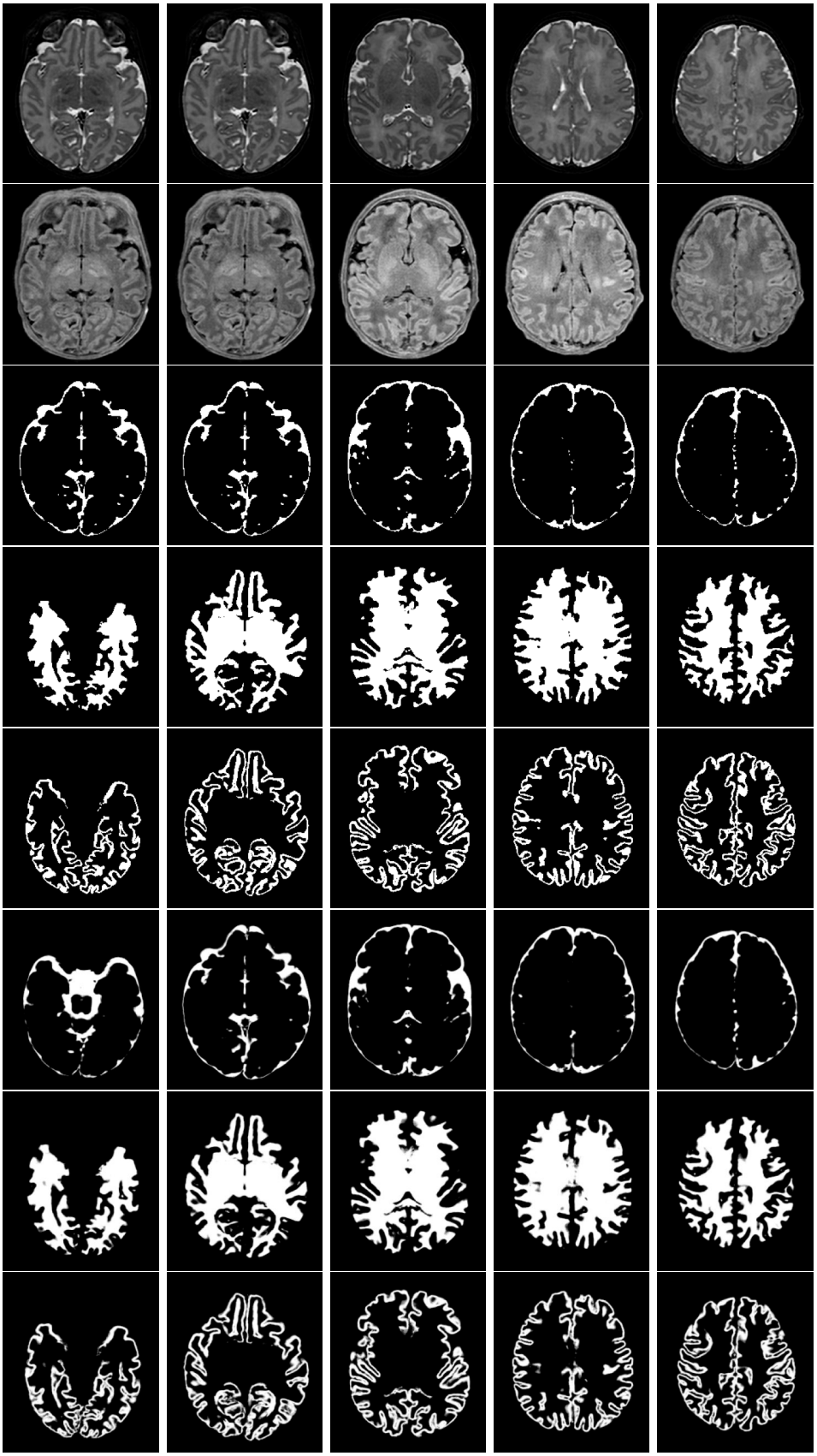

Figure B.2 – Overall application of IMAPA to a subject from dHCP dataset. The first row corresponds to T2w image; the second to T1w; from third to fifth to reference segmentation of CSF, WM and cortex and the three last rows to IMAPA results.

Appendix C

Publications

Articles in international journals

1. Carlos Tor-Díez, Nicolas Passat, Isabelle Bloch, Sylvain Faisan, Nathalie Bednarek, and François Rousseau. **An iterative multi-atlas patch-based approach for cortex segmentation from neonatal MRI.** Computerized Medical Imaging and Graphics, 70:73–82, 2018, hal-01761063.

Articles in international conferences proceedings

1. Carlos Tor-Díez, Chi-Hieu Pham, Hélène Meunier, Sylvain Faisan, Isabelle Bloch, Nathalie Bednarek, Nicolas Passat, and François Rousseau. **Evaluation of cortical segmentation pipelines on clinical neonatal MRI data.** In 41th IEEE Engineering in Medicine and Biology (EMBC 2019), 2019, hal-01896545.

2. Carlos Tor-Díez, Sylvain Faisan, Loïc Mazo, Nathalie Bednarek, Hélène Meunier, Isabelle Bloch, Nicolas Passat, and François Rousseau. **Multilabel, multiscale topological transformation for cerebral MRI segmentation post-processing.** In 14th International Symposium on Mathematical Morphology (ISMM 2019), pp. 471–482, 2019, hal-01982972.

3. Chi-Hieu Pham, Carlos Tor-Díez, Hélène Meunier, Nathalie Bednarek, Ronan Fablet, Nicolas Passat, and François Rousseau. **Simultaneous super-resolution and segmentation using a generative adversarial network: Application to neonatal brain MRI.** In 16th IEEE International Symposium on Biomedical Imaging (ISBI 2019), pp. 991–994, 2019, hal-01895163.

Communication in national conference

1. Carlos Tor-Díez, Nicolas Passat, Isabelle Bloch, Sylvain Faisan, Nathalie Bednarek, and François Rousseau. **Une approche par patchs, multi-atlas, itérative pour la segmentation du cortex cérébral en IRM néonatale.** In Congrès Reconnaissance des Formes, Image, Apprentissage et Perception (RFIAP), 2018, hal-01978970.

Bibliography

[Achanta et al., 2012] Achanta, R., Shaji, A., Smith, K., Lucchi, A., Fua, P., and Süsstrunk, S. (2012). SLIC superpixels compared to state-of-the-art superpixel methods. *IEEE Transactions on Pattern Analysis and Machine Intelligence*, 34(11):2274–2282.

[Akkus et al., 2017] Akkus, Z., Galimzianova, A., Hoogi, A., Rubin, D. L., and Erickson, B. J. (2017). Deep Learning for Brain MRI Segmentation: State of the Art and Future Directions. *Journal of Digital Imaging*, 30(4):449–459.

[Anbeek et al., 2013] Anbeek, P., Igum, I., Kooij, B. J. M. v., Mol, C. P., Kersbergen, K. J., Groenendaal, F., Viergever, M. A., Vries, L. S. d., and Benders, M. J. N. L. (2013). Automatic Segmentation of Eight Tissue Classes in Neonatal Brain MRI. *PLOS ONE*, 8(12):e81895.

[Ancel et al., 2014] Ancel, P.-Y., Goffinet, F., and EPIPAGE 2 Writing Group (2014). EPIPAGE 2: a preterm birth cohort in France in 2011. *BMC Pediatrics*, 14(1):97.

[Ashburner and Friston, 2005] Ashburner, J. and Friston, K. J. (2005). Unified segmentation. *NeuroImage*, 26(3):839–851.

[Asman and Landman, 2012] Asman, A. J. and Landman, B. A. (2012). Non-Local STAPLE: An Intensity-Driven Multi-Atlas Rater Model. *Medical Image Computing and Computer-Assisted Intervention (MICCAI)*, 15(Pt 3):426–434.

[Avants et al., 2008] Avants, B. B., Epstein, C. L., Grossman, M., and Gee, J. C. (2008). Symmetric diffeomorphic image registration with cross-correlation: Evaluating automated labeling of elderly and neurodegenerative brain. *Medical Image Analysis*, 12(1):26–41.

[Awate and Whitaker, 2014] Awate, S. P. and Whitaker, R. T. (2014). Multiatlas segmentation as nonparametric regression. *IEEE Transactions on Medical Imaging*, 33(9):1803–1817.

[Bach Cuadra et al., 2004] Bach Cuadra, M., Pollo, C., Bardera, A., Cuisenaire, O., Villemure, J., and Thiran, J. (2004). Atlas-based segmentation of pathological MR brain images using a model of lesion growth.

[Bai et al., 2009] Bai, Y., Han, X., and Prince, J. L. (2009). Digital topology on adaptive octree grids. *Journal of Mathematical Imaging and Vision*, 34(2):165–184.

[Ball et al., 2013a] Ball, G., Boardman, J. P., Aljabar, P., Pandit, A., Arichi, T., Merchant, N., Rueckert, D., Edwards, A. D., and Counsell, S. J. (2013a). The influence of preterm birth on the developing thalamocortical connectome. *Cortex*, 49(6):1711–1721.

[Ball et al., 2013b] Ball, G., Srinivasan, L., Aljabar, P., Counsell, S. J., Durighel, G., Hajnal, J. V., Rutherford, M. A., and Edwards, A. D. (2013b). Development of cortical microstructure in the preterm human brain. *Proceedings of the National Academy of Sciences*, 110(23):9541–9546.

[Barkovich, 2005] Barkovich, A. J. (2005). Magnetic resonance techniques in the assessment of myelin and myelination. *Journal of Inherited Metabolic Disease*, 28(3):311–343.

[Bazin et al., 2007] Bazin, P.-L., Ellingsen, L. M., and Pham, D. L. (2007). Digital homeomorphisms in deformable registration. In *Information Processing in Medical Imaging (IPMI), Proceedings*, pages 211–222.

[Bazin and Pham, 2007a] Bazin, P.-L. and Pham, D. L. (2007a). Topology correction of segmented medical images using a fast marching algorithm. *Computer Methods and Programs in Biomedicine*, 88(2):182–190.

[Bazin and Pham, 2007b] Bazin, P.-L. and Pham, D. L. (2007b). Topology-preserving tissue classification of magnetic resonance brain images. *IEEE Transactions on Medical Imaging*, 26(4):487–496.

[Beare et al., 2016] Beare, R. J., Chen, J., Kelly, C. E., Alexopoulos, D., Smyser, C. D., Rogers, C. E., Loh, W. Y., Matthews, L. G., Cheong, J. L. Y., Spittle, A. J., Anderson, P. J., Doyle, L. W., Inder, T. E., Seal, M. L., and Thompson, D. K. (2016). Neonatal brain tissue classification with morphological adaptation and unified segmentation. *Frontiers in Neuroinformatics*, 10:12.

[Benkarim et al., 2017a] Benkarim, O. M., Piella, G., González Ballester, M. A., and Sanroma, G. (2017a). Discriminative confidence estimation for probabilistic multi-atlas label fusion. *Medical Image Analysis*, 42:274–287.

[Benkarim et al., 2019] Benkarim, O. M., Piella, G., Hahner, N., Eixarch, E., González Ballester, M. A., and Sanroma, G. (2019). Patch spaces and fusion strategies in patch-based label fusion. *Computerized Medical Imaging and Graphics*, 71:79–89.

[Benkarim et al., 2017b] Benkarim, O. M., Sanroma, G., Zimmer, V. A., Muñoz-Moreno, E., Hahner, N., Eixarch, E., Camara, O., González Ballester, M. A., and Piella, G. (2017b). Toward the automatic quantification of in utero brain development in 3D structural MRI: A review. *Human Brain Mapping*, 38(5):2772–2787.

[Bertrand, 1994] Bertrand, G. (1994). Simple points, topological numbers and geodesic neighborhoods in cubic grids. *Pattern Recognition Letters*, 15(10):1003–1011.

[Bertrand and Malandain, 1994] Bertrand, G. and Malandain, G. (1994). A new characterization of three-dimensional simple points. *Pattern Recognition Letters*, 15(2):169–175.

[Buades et al., 2005] Buades, A., Coll, B., and Morel, J. (2005). A Review of Image Denoising Algorithms, with a New One. *Multiscale Modeling & Simulation*, 4(2):490–530.

[Cabezas et al., 2011] Cabezas, M., Oliver, A., Lladó, X., Freixenet, J., and Bach Cuadra, M. (2011). A review of atlas-based segmentation for magnetic resonance brain images. *Computer Methods and Programs in Biomedicine*, 104(3):e158–e177.

[Caldairou et al., 2011a] Caldairou, B., Passat, N., Habas, P. A., Studholme, C., Koob, M., Dietemann, J.-L., and Rousseau, F. (2011a). Segmentation of the cortex in fetal MRI using a topological model. In *International Symposium on Biomedical Imaging (ISBI), Proceedings*, pages 2045–2048.

[Caldairou et al., 2011b] Caldairou, B., Passat, N., Habas, P. A., Studholme, C., and Rousseau, F. (2011b). A non-local fuzzy segmentation method: Application to brain MRI. *Pattern Recognition*, 44(9):1916–1927.

[Cardoso et al., 2011] Cardoso, M. J., Clarkson, M. J., Modat, M., Talbot, H., Couprie, M., and Ourselin, S. (2011). Topologically correct cortical segmentation using Khalimsky's cubic complex framework. In *Medical Imaging 2011: Image Processing*, volume 7962, page 79620P.

[Cardoso et al., 2013] Cardoso, M. J., Melbourne, A., Kendall, G. S., Modat, M., Robertson, N. J., Marlow, N., and Ourselin, S. (2013). AdaPT: An adaptive preterm segmentation algorithm for neonatal brain MRI. *NeuroImage*, 65:97–108.

[Christensen et al., 1997] Christensen, G. E., Joshi, S. C., and Miller, M. I. (1997). Volumetric transformation of brain anatomy. *IEEE Transactions on Medical Imaging*, 16(6):864–877.

[Cointepas et al., 2001] Cointepas, Y., Bloch, I., and Garnero, L. (2001). A cellular model for multi-objects multi-dimensional homotopic deformations. *Pattern Recognition*, 34(9):1785–1798.

[Collins et al., 1995] Collins, D. L., Holmes, C. J., Peters, T. M., and Evans, A. C. (1995). Automatic 3-D model-based neuroanatomical segmentation. *Human Brain Mapping*, 3(3):190–208.

[Cordier et al., 2016] Cordier, N., Delingette, H., and Ayache, N. (2016). A patch-based approach for the segmentation of pathologies: Application to glioma labelling. *IEEE Transactions on Medical Imaging*, 35(4):1066–1076.

[Couprie and Bertrand, 2009] Couprie, M. and Bertrand, G. (2009). New characterizations of simple points in 2d, 3d, and 4D discrete spaces. *IEEE Transactions on Pattern Analysis Machine Intelligence*, 31(4):637–648.

[Coupé et al., 2010] Coupé, P., Manjón, J. V., Fonov, V., Pruessner, J., Robles, M., and Collins, D. L. (2010). Nonlocal Patch-Based Label Fusion for Hippocampus Segmentation. In *Medical Image Computing and Computer-Assisted Intervention (MICCAI)*, Lecture Notes in Computer Science, pages 129–136.

[Coupé et al., 2011] Coupé, P., Manjón, J. V., Fonov, V., Pruessner, J., Robles, M., and Collins, D. L. (2011). Patch-based segmentation using expert priors: Application to hippocampus and ventricle segmentation. *NeuroImage*, 54(2):940–954.

[Coupé et al., 2008] Coupé, P., Yger, P., Prima, S., Hellier, P., Kervrann, C., and Barillot, C. (2008). An Optimized Blockwise Nonlocal Means Denoising Filter for 3-D Magnetic Resonance Images. *IEEE Transactions on Medical Imaging*, 27(4):425–441.

[Csernansky et al., 1998] Csernansky, J. G., Joshi, S., Wang, L., Haller, J. W., Gado, M., Miller, J. P., Grenander, U., and Miller, M. I. (1998). Hippocampal morphometry in schizophrenia by high dimensional brain mapping. *Proceedings of the National Academy of Sciences*, 95(19):11406–11411.

[Daducci et al., 2012] Daducci, A., Gerhard, S., Griffa, A., Lemkaddem, A., Cammoun, L., Gigandet, X., Meuli, R., Hagmann, P., and Thiran, J.-P. (2012). The Connectome Mapper: An Open-Source Processing Pipeline to Map Connectomes with MRI. *PLOS ONE*, 7(12):e48121.

[Dai et al., 2013] Dai, Y., Shi, F., Wang, L., Wu, G., and Shen, D. (2013). iBEAT: A Toolbox for Infant Brain Magnetic Resonance Image Processing. *Neuroinformatics*, 11(2):211–225.

[Damiand et al., 2011] Damiand, G., Dupas, A., and Lachaud, J.-O. (2011). Fully deformable 3D digital partition model with topological control. *Pattern Recognition Letters*, 32(9):1374–1383.

[Das et al., 2009] Das, S. R., Avants, B. B., Grossman, M., and Gee, J. C. (2009). Registration based cortical thickness measurement. *Neuroimage*, 45(3):867–879.

[Deledalle et al., 2012] Deledalle, C.-A., Duval, V., and Salmon, J. (2012). Non-local Methods with Shape-Adaptive Patches (NLM-SAP). *Journal of Mathematical Imaging and Vision*, 43(2):103–120.

[Devi et al., 2015] Devi, C. N., Chandrasekharan, A., Sundararaman, V. K., and Alex, Z. C. (2015). Neonatal brain MRI segmentation: A review. *Computers in Biology and Medicine*, 64:163–178.

[Doan et al., 2010] Doan, N. T., Xivry, J. O. d., and Macq, B. (2010). Effect of inter-subject variation on the accuracy of atlas-based segmentation applied to human brain structures.

[Dolz et al., 2018] Dolz, J., Ayed, I. B., Yuan, J., and Desrosiers, C. (2018). Isointense infant brain segmentation with a hyper-dense connected convolutional neural network. pages 616–620.

[Doshi et al., 2013] Doshi, J., Erus, G., Ou, Y., Gaonkar, B., and Davatzikos, C. (2013). Multi-Atlas Skull-Stripping. *Academic Radiology*, 20(12):1566–1576.

[Dubois et al., 2008] Dubois, J., Benders, M., Borradori-Tolsa, C., Cachia, A., Lazeyras, F., Ha-Vinh Leuchter, R., Sizonenko, S. V., Warfield, S. K., Mangin, J. F., and Hüppi, P. S. (2008). Primary cortical folding in the human newborn: an early marker of later functional development. *Brain*, 131(8):2028–2041.

[Duval et al., 2011] Duval, V., Aujol, J.-F., and Gousseau, Y. (2011). A bias-variance approach for the nonlocal means. *SIAM Journal on Imaging Sciences*, 4(2):760–788.

[Eskildsen et al., 2012] Eskildsen, S. F., Coupé, P., Fonov, V., Manjón, J. V., Leung, K. K., Guizard, N., Wassef, S. N., Østergaard, L. R., and Collins, D. L. (2012). BEaST: Brain extraction based on nonlocal segmentation technique. *NeuroImage*, 59(3):2362–2373.

[Faisan et al., 2012] Faisan, S., Heinrich, C., Rousseau, F., Lallement, A., and Zallat, J. (2012). Joint filtering estimation of Stokes vector images based on a nonlocal means approach. *JOSA A*, 29(9):2028–2037.

[Faisan et al., 2011] Faisan, S., Passat, N., Noblet, V., Chabrier, R., and Meyer, C. (2011). Topology preserving warping of 3-D binary images according to continuous one-to-one mappings. *IEEE Transactions on Image Processing*, 20(8):2135–2145.

[Fearing et al., 2008] Fearing, M. A., Bigler, E. D., Wilde, E. A., Johnson, J. L., Hunter, J. V., Li, X., Hanten, G., and Levin, H. S. (2008). Morphometric MRI Findings in the Thalamus and Brainstem in Children After Moderate to Severe Traumatic Brain Injury. *Journal of Child Neurology*, 23(7):729–737.

[Filipek et al., 1994] Filipek, P. A., Richelme, C., Kennedy, D. N., and Caviness, V. S. (1994). The Young Adult Human Brain: An MRI-based Morphometric Analysis. *Cerebral Cortex*, 4(4):344–360.

[Fischl et al., 2001] Fischl, B., Liu, A., and Dale, A. M. (2001). Automated manifold surgery: Constructing geometrically accurate and topologically correct models of the human cerebral cortex. *IEEE Transactions on Medical Imaging*, 20(1):70–80.

[Geffroy et al., 2011] Geffroy, D., Rivière, D., Denghien, I., Souedet, N., Laguitton, S., and Cointepas, Y. (2011). BrainVISA: A complete software platform for neuroimaging. In *Python in Neuroscience workshop*.

[González Ballester et al., 2002] González Ballester, M. ., Zisserman, A. P., and Brady, M. (2002). Estimation of the partial volume effect in MRI. *Medical Image Analysis*, 6(4):389–405.

[Gousias et al., 2012] Gousias, I. S., Edwards, A. D., Rutherford, M. A., Counsell, S. J., Hajnal, J. V., Rueckert, D., and Hammers, A. (2012). Magnetic resonance imaging of the newborn brain: Manual segmentation of labelled atlases in term-born and preterm infants. *NeuroImage*, 62(3):1499–1509.

[Gousias et al., 2013] Gousias, I. S., Hammers, A., Counsell, S. J., Srinivasan, L., Rutherford, M. A., Heckemann, R. A., Hajnal, J. V., Rueckert, D., and Edwards, A. D. (2013). Magnetic Resonance Imaging of the Newborn Brain: Automatic Segmentation of Brain Images into 50 Anatomical Regions. *PLOS ONE*, 8(4):e59990.

[Greenspan, 2009] Greenspan, H. (2009). Super-Resolution in Medical Imaging. *The Computer Journal*, 52(1):43–63.

[Gui et al., 2012] Gui, L., Lisowski, R., Faundez, T., Hüppi, P. S., Lazeyras, F., and Kocher, M. (2012). Morphology-driven automatic segmentation of MR images of the neonatal brain. *Medical Image Analysis*, 16(8):1565–1579.

[Han et al., 2002] Han, X., Xu, C., Braga-Neto, U., and Prince, J. L. (2002). Topology correction in brain cortex segmentation using a multiscale, graph-based algorithm. *IEEE Transactions on Medical Imaging*, 21(2):109–121.

[Han et al., 2003] Han, X., Xu, C., and Prince, J. L. (2003). A Topology Preserving Level Set Method for Geometric Deformable Models. *IEEE Transactions on Pattern Analysis Machine Intelligence*, 25(6):755–768.

[Hao et al., 2016] Hao, S., Li, G., Wang, L., Meng, Y., and Shen, D. (2016). Learning-based topological correction for infant cortical surfaces. In *Medical Image Computing and Computer-Assisted Intervention (MICCAI)*, Lecture Notes in Computer Science, pages 219–227.

[Hao et al., 2014] Hao, Y., Wang, T., Zhang, X., Duan, Y., Yu, C., Jiang, T., and Fan, Y. (2014). Local label learning (LLL) for subcortical structure segmentation: application to hippocampus segmentation. *Human Brain Mapping*.

[Heinrich et al., 2012] Heinrich, M. P., Jenkinson, M., Bhushan, M., Matin, T., Gleeson, F. V., Brady, S. M., and Schnabel, J. A. (2012). MIND: Modality independent neighbourhood descriptor for multi-modal deformable registration. *Medical Image Analysis*, 16(7):1423–1435.

[Hughes et al., 2017] Hughes, E., Cordero-Grande, L., Murgasova, M., Hutter, J., Price, A., Santos Gomes, A., Allsop, J., Steinweg, J., Tusor, N., Wurie, J., Bueno-Conde, J., Tournier, J.-D., Abaei, M., Counsell, S., Rutherford, M., Pietsch, M., Edwards, D., Hajnal, J., Fitzgibbon, S., Duff, E., Bastiani, M., Andersson, J., Jbabdi, S., Sotiropoulos, S., Jenkinson, M., Smith, S., Harrison, S., Griffanti, L., Wright, R., Bozek, J., Beckmann, C., Makropoulos, A., Robinson, E., Schuh, A., Passerat Palmbach, J., Lenz, G., Mortari, F., Tenev, T., and Rueckert, D. (2017). The Developing Human Connectome: Announcing the first release of open access neonatal brain imaging. In *23rd Annual Meeting of the Organization for Human Brain Mapping*.

[Huo et al., 2018] Huo, J., Wu, J., Cao, J., and Wang, G. (2018). Supervoxel based method for multi-atlas segmentation of brain MR images. *NeuroImage*, 175:201–214.

[Huo et al., 2019] Huo, Y., Xu, Z., Xiong, Y., Aboud, K., Parvathaneni, P., Bao, S., Bermudez, C., Resnick, S. M., Cutting, L. E., and Landman, B. A. (2019). 3{D} whole brain segmentation using spatially localized atlas network tiles. *NeuroImage*, 194:105–119.

[Hüppi et al., 1998] Hüppi, P. S., Warfield, S., Kikinis, R., Barnes, P. D., Zientara, G. P., Jolesz, F. A., Tsuji, M. K., and Volpe, J. J. (1998). Quantitative magnetic resonance imaging of brain development in premature and mature newborns. *Annals of Neurology*, 43(2):224–235.

[Iglesias and Sabuncu, 2015] Iglesias, J. E. and Sabuncu, M. R. (2015). Multi-atlas segmentation of biomedical images: A survey. *Medical Image Analysis*, 24(1):205–219.

[Igum et al., 2015] Igum, I., Benders, M. J. N. L., Avants, B., Cardoso, M. J., Counsell, S. J., Gomez, E. F., Gui, L., Hüppi, P. S., Kersbergen, K. J., Makropoulos, A., Melbourne, A., Moeskops, P., Mol, C. P., Kuklisova-Murgasova, M., Rueckert, D., Schnabel, J. A., Srhoj-Egekher, V., Wu, J., Wang, S., de Vries, L. S., and Viergever, M. A. (2015). Evaluation of automatic neonatal brain segmentation algorithms: The NeoBrainS12 challenge. *Medical Image Analysis*, 20(1):135–151.

[Kervrann and Boulanger, 2008] Kervrann, C. and Boulanger, J. (2008). Local adaptivity to variable smoothness for exemplar-based image regularization and representation. *International Journal of Computer Vision*, 79(1):45–69.

[Kim et al., 2016] Kim, H., Lepage, C., Maheshwary, R., Jeon, S., Evans, A. C., Hess, C. P., Barkovich, A. J., and Xu, D. (2016). NEOCIVET: Towards accurate morphometry of neonatal gyrification and clinical applications in preterm newborns. *NeuroImage*, 138:28–42.

[Kleesiek et al., 2016] Kleesiek, J., Urban, G., Hubert, A., Schwarz, D., Maier-Hein, K., Bendszus, M., and Biller, A. (2016). Deep MRI brain extraction: A 3D convolutional neural network for skull stripping. *NeuroImage*, 129:460–469.

[Klein et al., 2010] Klein, A., Ghosh, S. S., Avants, B., Yeo, B. T. T., Fischl, B., Ardekani, B., Gee, J. C., Mann, J. J., and Parsey, R. V. (2010). Evaluation of volume-based and surface-based brain image registration methods. *NeuroImage*, 51(1):214–220.

[Kong, 1989] Kong, T. Y. (1989). A digital fundamental group. *Computers & Graphics*, 13(2):159–166.

[Kriegeskorte and Goebel, 2001] Kriegeskorte, N. and Goebel, N. (2001). An efficient algorithm for topologically correct segmentation of the cortical sheet in anatomical MR volumes. *NeuroImage*, 14(2):329–346.

[Krizhevsky et al., 2012] Krizhevsky, A., Sutskever, I., and Hinton, G. E. (2012). ImageNet Classification with Deep Convolutional Neural Networks. In *Advances in Neural Information Processing Systems 25*, pages 1097–1105.

[Kuklisova-Murgasova et al., 2012] Kuklisova-Murgasova, M., Quaghebeur, G., Rutherford, M. A., Hajnal, J. V., and Schnabel, J. A. (2012). Reconstruction of fetal brain MRI with intensity matching and complete outlier removal. *Medical Image Analysis*, 16(8):1550–1564.

[Lancaster et al., 1997] Lancaster, J. L., Rainey, L. H., Summerlin, J. L., Freitas, C. S., Fox, P. T., Evans, A. C., Toga, A. W., and Mazziotta, J. C. (1997). Automated labeling of the human brain: A preliminary report on the development and evaluation of a forward-transform method. *Human Brain Mapping*, 5(4):238–242.

[LeCun et al., 1998] LeCun, Y., Bottou, L., Bengio, Y., and Haffner, P. (1998). Gradient-based learning applied to document recognition. *Proceedings of the IEEE*, 86(11):2278–2324.

[Lefèvre et al., 2016] Lefèvre, J., Germanaud, D., Dubois, J., Rousseau, F., de Macedo Santos, I., Angleys, H., Mangin, J.-F., Hüppi, P. S., Girard, N., and De Guio, F. (2016). Are Developmental Trajectories of Cortical Folding Comparable Between Cross-sectional Datasets of Fetuses and Preterm Newborns? *Cerebral Cortex*, 26(7):3023–3035.

[Leroy et al., 2011] Leroy, F., Mangin, J.-F., Rousseau, F., Glasel, H., Hertz-Pannier, L., Dubois, J., and Dehaene-Lambertz, G. (2011). Atlas-free surface reconstruction of the cortical grey-white interface in infants. *PLOS ONE*, 6(11):e27128.

[Li et al., 2019] Li, G., Wang, L., Yap, P.-T., Wang, F., Wu, Z., Meng, Y., Dong, P., Kim, J., Shi, F., Rekik, I., Lin, W., and Shen, D. (2019). Computational neuroanatomy of baby brains: A review. *Neuroimage*, 185:906–925.

[Liao et al., 2013] Liao, S., Gao, Y., Lian, J., and Shen, D. (2013). Sparse Patch-Based Label Propagation for Accurate Prostate Localization in CT Images. *IEEE Transactions on Medical Imaging*, 32(2).

[Liu et al., 2016] Liu, M., Kitsch, A., Miller, S., Chau, V., Poskitt, K., Rousseau, F., Shaw, D., and Studholme, C. (2016). Patch-based augmentation of Expectation-Maximization for brain MRI tissue segmentation at arbitrary age after premature birth. *NeuroImage*, 127:387–408.

[Lorenz et al., 1998] Lorenz, J. M., Wooliever, D. E., Jetton, J. R., and Paneth, N. (1998). A Quantitative Review of Mortality and Developmental Disability in Extremely Premature Newborns. *Archives of Pediatrics & Adolescent Medicine*, 152(5):425–435.

[Makki et al., 2019] Makki, K., Borotikar, B., Garetier, M., Acosta, O., Brochard, S., Ben Salem, D., and Rousseau, F. (2019). 4D in vivo quantification of ankle joint space width using dynamic MRI. In *41th IEEE Engineering in Medicine and Biology (EMBC 2019)*.

[Makris et al., 1997] Makris, N., Worth, A. J., Papadimitriou, G. M., Stakes, J. W., Caviness, V. S., Kennedy, D. N., Pandya, D. N., Kaplan, E., Sorensen, A. G., Wu, O., Reese, T. G., Wedeen, V. J., Rosen, B. R., Kennedy, D. N., and Davis, T. L. (1997). Morphometry of in vivo human white matter association pathways with diffusion-weighted magnetic resonance imaging. *Annals of Neurology*, 42(6):951–962.

[Makropoulos et al., 2016] Makropoulos, A., Aljabar, P., Wright, R., Hüning, B., Merchant, N., Arichi, T., Tusor, N., Hajnal, J. V., Edwards, A. D., Counsell, S. J., and Rueckert, D. (2016). Regional growth and atlasing of the developing human brain. *NeuroImage*, 125:456–478.

[Makropoulos et al., 2017] Makropoulos, A., Counsell, S. J., and Rueckert, D. (2017). A review on automatic fetal and neonatal brain MRI segmentation. *NeuroImage*, 170:231–248.

[Makropoulos et al., 2014] Makropoulos, A., Gousias, I. S., Ledig, C., Aljabar, P., Serag, A., Hajnal, J. V., Edwards, A. D., Counsell, S. J., and Rueckert, D. (2014). Automatic Whole Brain MRI Segmentation of the Developing Neonatal Brain. *IEEE Transactions on Medical Imaging*, 33(9):1818–1831.

[Makropoulos et al., 2018] Makropoulos, A., Robinson, E. C., Schuh, A., Wright, R., Fitzgibbon, S., Bozek, J., Counsell, S. J., Steinweg, J., Passerat-Palmbach, J., Lenz, G., Mortari, F., Tenev, T., Duff, E. P., Bastiani, M., Cordero-Grande, L., Hughes, E., Tusor, N., Tournier, J.-D., Hutter, J., Price, A. N., Murgasova, M., Kelly, C., Rutherford, M. A., Smith, S. M., Edwards, A. D., Hajnal, J. V., Jenkinson, M., and Rueckert, D. (2018). The Developing Human Connectome Project: A minimal processing pipeline for neonatal cortical surface reconstruction. *NeuroImage*, 173:88–112.

[Malandain and Bertrand, 1992] Malandain, G. and Bertrand, G. (1992). Fast characterization of 3D simple points. In *Proceedings., 11th IAPR International Conference on Pattern Recognition. Vol. III. Conference C: Image, Speech and Signal Analysis,*, pages 232–235.

[Malandain et al., 1993] Malandain, G., Bertrand, G., and Ayache, N. (1993). Topological segmentation of discrete surfaces. *International Journal of Computer Vision*, 10(2):183–197.

[Mangin, 2000] Mangin, J.-F. (2000). Entropy minimization for automatic correction of intensity nonuniformity. In *Proceedings IEEE Workshop on Mathematical Methods in Biomedical Image Analysis. MMBIA-2000 (Cat. No.PR00737)*, pages 162–169.

[Mangin et al., 1995] Mangin, J.-F., Frouin, V., Bloch, I., Régis, J., and López-Krahe, J. (1995). From 3D magnetic resonance images to structural representations of the cortex topography using topology preserving deformations. *Journal of Mathematical Imaging and Vision*, 5(4):297–318.

[Manjón et al., 2010] Manjón, J. V., Coupé, P., Buades, A., Fonov, V., Louis Collins, D., and Robles, M. (2010). Non-local MRI upsampling. *Medical Image Analysis*, 14(6):784–792.

[Markestad et al., 2005] Markestad, T., Kaaresen, P. I., Ronnestad, A., Reigstad, H., Lossius, K., Medbo, S., Zanussi, G., Engelund, I. E., Skjaerven, R., and Irgens, L. M. (2005). Early death, morbidity, and need of treatment among extremely premature infants. *Pediatrics*, 115(5):1289–1298.

[Mazo, 2012] Mazo, L. (2012). A Framework for Label Images. In *Computational Topology in Image Context (CTIC), Proceedings*, pages 1–10.

[Mazo et al., 2012a] Mazo, L., Passat, N., Couprie, M., and Ronse, C. (2012a). Digital Imaging: A Unified Topological Framework. *Journal of Mathematical Imaging and Vision*, 44(1):19–37.

[Mazo et al., 2012b] Mazo, L., Passat, N., Couprie, M., and Ronse, C. (2012b). Topology on Digital Label Images. *Journal of Mathematical Imaging and Vision*, 44(3):254–281.

[Miller et al., 1993] Miller, M. I., Christensen, G. E., Amit, Y., and Grenander, U. (1993). Mathematical textbook of deformable neuroanatomies. *Proceedings of the National Academy of Sciences of the United States of America*, 90(24):11944–11948.

[Moeskops et al., 2015] Moeskops, P., Benders, M. J. N. L., Chi, S. M., Kersbergen, K. J., Groenendaal, F., de Vries, L. S., Viergever, M. A., and Igum, I. (2015). Automatic segmentation of MR brain images of preterm infants using supervised classification. *NeuroImage*, 118:628–641.

[Moeskops et al., 2016] Moeskops, P., Viergever, M. A., Mendrik, A. M., Vries, L. S. d., Benders, M. J. N. L., and Igum, I. (2016). Automatic Segmentation of MR Brain Images With a Convolutional Neural Network. *IEEE Transactions on Medical Imaging*, 35(5):1252–1261.

[Morel et al., 2016] Morel, B., Xu, Y., Virzi, A., Géraud, T., Adamsbaum, C., and Bloch, I. (2016). A challenging issue: Detection of white matter hyperintensities in neonatal brain MRI. In *2016 38th Annual International Conference of the IEEE Engineering in Medicine and Biology Society (EMBC)*, pages 93–96.

[Orasanu et al., 2016] Orasanu, E., Melbourne, A., Cardoso, M. J., Lomabert, H., Kendall, G. S., Robertson, N. J., Marlow, N., and Ourselin, S. (2016). Cortical folding of the preterm brain: a longitudinal analysis of extremely preterm born neonates using spectral matching. *Brain and Behavior*, 6(8):e00488.

[Passat et al., 2007] Passat, N., Couprie, M., and Bertrand, G. (2007). Topological monsters in $\mathcal{F}^3$: A non-exhaustive bestiary. In *International Symposium on Mathematical Morphology (ISMM)*, volume 2, pages 11–12. INPE.

[Pham et al., 2017a] Pham, C.-H., Ducournau, A., Fablet, R., and Rousseau, F. (2017a). Brain MRI super-resolution using deep 3D convolutional networks. In *IEEE 14th International Symposium on Biomedical Imaging (ISBI 2017)*, pages 197–200. IEEE.

[Pham et al., 2017b] Pham, C.-H., Fablet, R., and Rousseau, F. (2017b). Multi-scale brain MRI super-resolution using deep 3D convolutional networks.

[Pham et al., 2019] Pham, C.-H., Tor-Díez, C., Meunier, H., Bednarek, N., Fablet, R., Passat, N., and Rousseau, F. (2019). Simultaneous super-resolution and segmentation using a generative adversarial network: Application to neonatal brain MRI. In *International Symposium on Biomedical Imaging (ISBI)*, pages 991–994.

[Pham et al., 2010] Pham, D. L., Bazin, P.-L., and Prince, J. L. (2010). Digital Topology in Brain Imaging. *IEEE Signal Processing Magazine*, 27(4):51–59.

[Poupon et al., 1998] Poupon, F., Mangin, J.-F., Hasboun, D., Poupon, C., Magnin, I. E., and Frouin, V. (1998). Multi-object Deformable Templates Dedicated to the Segmentation of Brain Deep Structures. In *Medical Image Computing and Computer-Assisted Intervention (MICCAI)*, pages 1134–1143.

[Prima and Commowick, 2013] Prima, S. and Commowick, O. (2013). Using bilateral symmetry to improve non-local means denoising of MR brain images. pages 1231–1234. IEEE. WOS:000326900100308.

[Purves and Lichtman, 1985] Purves, D. and Lichtman, J. W. (1985). *Principles of neural development*. Sinauer Associates, Sunderland, Mass. OCLC: 10798963.

[Ronneberger et al., 2015] Ronneberger, O., Fischer, P., and Brox, T. (2015). U-Net: Convolutional Networks for Biomedical Image Segmentation. In Navab, N., Hornegger, J., Wells, W. M., and Frangi, A. F., editors, *Medical Image Computing and Computer-Assisted Intervention (MICCAI)*, Lecture Notes in Computer Science, pages 234–241. Springer International Publishing.

[Rousseau, 2008] Rousseau, F. (2008). Brain hallucination. In *ECCV*, pages 497–508.

[Rousseau et al., 2006] Rousseau, F., Glenn, O. A., Iordanova, B., Rodriguez-Carranza, C., Vigneron, D. B., Barkovich, J. A., and Studholme, C. (2006). Registration-Based Approach for Reconstruction of High-Resolution In Utero Fetal MR Brain Images. *Academic Radiology*, 13(9):1072–1081.

[Rousseau et al., 2011] Rousseau, F., Habas, P. A., and Studholme, C. (2011). A supervised patch-based approach for human brain labeling. *IEEE Transactions on Medical Imaging*, 30(10):1852–1862.

[Roweis and Saul, 2000] Roweis, S. T. and Saul, L. K. (2000). Nonlinear dimensionality reduction by locally linear embedding. *Science*, 290(5500):2323–2326.

[Roy et al., 2015] Roy, S., He, Q., Sweeney, E., Carass, A., Reich, D. S., Prince, J. L., and Pham, D. L. (2015). Subject-Specific Sparse Dictionary Learning for Atlas-Based Brain MRI Segmentation. *IEEE Journal of Biomedical and Health Informatics*, 19(5):1598–1609.

[Sabuncu et al., 2010] Sabuncu, M. R., Yeo, B. T. T., Van Leemput, K., Fischl, B., and Golland, P. (2010). A generative model for image segmentation based on label fusion. *IEEE Transactions on Medical Imaging*, 29(10):1714–1729.

[Saha et al., 2015] Saha, P. K., Strand, R., and Borgefors, G. (2015). Digital topology and geometry in medical imaging: A survey. *IEEE Transactions on Medical Imaging*, 34(9):1940–1964.

[Sanroma et al., 2018] Sanroma, G., Benkarim, O. M., Piella, G., Lekadir, K., Hahner, N., Eixarch, E., and González Ballester, M. A. (2018). Learning to combine complementary segmentation methods for fetal and 6-month infant brain MRI segmentation. *Medical Image Computing and Computer-Assisted Intervention (MICCAI)*, 69:52–59.

[Schirner et al., 2015] Schirner, M., Rothmeier, S., Jirsa, V. K., McIntosh, A. R., and Ritter, P. (2015). An automated pipeline for constructing personalized virtual brains from multimodal neuroimaging data. *NeuroImage*, 117:343–357.

[Schuh et al., 2017] Schuh, A., Makropoulos, A., Wright, R., Robinson, E. C., Tusor, N., Steinweg, J., Hughes, E., Grande, L. C., Price, A., Hutter, J., Hajnal, J. V., and Rueckert, D. (2017). A deformable model for the reconstruction of the neonatal cortex. In *2017 IEEE 14th International Symposium on Biomedical Imaging (ISBI 2017)*, pages 800–803.

[Schuh et al., 2015] Schuh, A., Murgasova, M., Makropoulos, A., Ledig, C., Counsell, S. J., Hajnal, J. V., Aljabar, P., and Rueckert, D. (2015). Construction of a 4D Brain Atlas and Growth Model Using Diffeomorphic Registration. In *Spatio-temporal Image Analysis for Longitudinal and Time-Series Image Data*, Lecture Notes in Computer Science, pages 27–37.

[Serag et al., 2012] Serag, A., Aljabar, P., Ball, G., Counsell, S. J., Boardman, J. P., Rutherford, M. A., Edwards, A. D., Hajnal, J. V., and Rueckert, D. (2012). Construction of a consistent high-definition spatio-temporal atlas of the developing brain using adaptive kernel regression. *NeuroImage*, 59(3):2255–2265.

[Serag et al., 2016] Serag, A., Blesa, M., Moore, E. J., Pataky, R., Sparrow, S. A., Wilkinson, A. G., Macnaught, G., Semple, S. I., and Boardman, J. P. (2016). Accurate Learning with Few Atlases (ALFA): An algorithm for MRI neonatal brain extraction and comparison with 11 publicly available methods. *Scientific Reports*, 6:23470.

[Shattuck and Leahy, 2001] Shattuck, D. W. and Leahy, R. M. (2001). Automated graph-based analysis and correction of cortical volume topology. *IEEE Transactions on Medical Imaging*, 20(11):1167–1177.

[Shen et al., 2017] Shen, D., Wu, G., and Suk, H.-I. (2017). Deep Learning in Medical Image Analysis. *Annual Review of Biomedical Engineering*, 19(1):221–248.

[Shi et al., 2012] Shi, F., Wang, L., Dai, Y., Gilmore, J. H., Lin, W., and Shen, D. (2012). LABEL: Pediatric brain extraction using learning-based meta-algorithm. *NeuroImage*, 62(3):1975–1986.

[Shiee et al., 2010] Shiee, N., Bazin, P.-L., Ozturk, A., Reich, D. S., Calabresi, P. A., and Pham, D. L. (2010). A topology-preserving approach to the segmentation of brain images with multiple sclerosis lesions. *NeuroImage*, 49(2):1524–1535.

[Siqueira et al., 2008] Siqueira, M., Latecki, L. J., Tustison, N. J., Gallier, J. H., and Gee, J. C. (2008). Topological Repairing of 3D Digital Images. *Journal of Mathematical Imaging and Vision*, 30(3):249–274.

[Sled et al., 1998] Sled, J. G., Zijdenbos, A. P., and Evans, A. C. (1998). A nonparametric method for automatic correction of intensity nonuniformity in MRI data. *IEEE Transactions on Medical Imaging*, 17(1):87–97.

[Smith, 2002] Smith, S. M. (2002). Fast robust automated brain extraction. *Human Brain Mapping*, 17(3):143–155.

[Song et al., 2007] Song, Z., Awate, S. P., Licht, D. J., and Gee, J. C. (2007). Clinical Neonatal Brain MRI Segmentation Using Adaptive Nonparametric Data Models and Intensity-Based Markov Priors. In Ayache, N., Ourselin, S., and Maeder, A., editors, *Medical Image Computing and Computer-Assisted Intervention (MICCAI)*, pages 883–890, Berlin, Heidelberg. Springer Berlin Heidelberg.

[Sun et al., 2019] Sun, L., Zhang, D., Lian, C., Wang, L., Wu, Z., Shao, W., Lin, W., Shen, D., Li, G., and Consortium, U. B. C. P. (2019). Topological correction of infant white matter surfaces using anatomically constrained convolutional neural network. *NeuroImage*.

[Ségonne, 2008] Ségonne, F. (2008). Active Contours Under Topology Control Genus Preserving Level Sets. *International Journal of Computer Vision*, 79(2):107–117.

[Ségonne et al., 2007] Ségonne, F., Pacheco, J., and Fischl, B. (2007). Geometrically accurate topology-correction of cortical surfaces using nonseparating loops. *IEEE Transactions on Medical Imaging*, 26(4):518–529.

[Timofte et al., 2013] Timofte, R., De, V., and Gool, L. V. (2013). Anchored Neighborhood Regression for Fast Example-Based Super-Resolution. In *2013 IEEE International Conference on Computer Vision*, pages 1920–1927.

[Tong et al., 2014] Tong, T., Wolz, R., Gao, Q., Guerrero, R., Hajnal, J. V., and Rueckert, D. (2014). Multiple instance learning for classification of dementia in brain MRI. *Medical Image Analysis*, 18(5):808–818.

[Tong et al., 2015] Tong, T., Wolz, R., Wang, Z., Gao, Q., Misawa, K., Fujiwara, M., Mori, K., Hajnal, J. V., and Rueckert, D. (2015). Discriminative dictionary learning for abdominal multi-organ segmentation. *Medical Image Analysis*, 23(1):92–104.

[Tu and Bai, 2010] Tu, Z. and Bai, X. (2010). Auto-Context and Its Application to High-Level Vision Tasks and 3D Brain Image Segmentation. *IEEE Transactions on Pattern Analysis and Machine Intelligence*, 32(10):1744–1757.

[Tustison et al., 2010] Tustison, N. J., Avants, B. B., Cook, P. A., Zheng, Y., Egan, A., Yushkevich, P. A., and Gee, J. C. (2010). N4ITK: Improved N3 Bias Correction. *IEEE Transactions on Medical Imaging*, 29(6):1310–1320.

[Tustison et al., 2014] Tustison, N. J., Cook, P. A., Klein, A., Song, G., Das, S. R., Duda, J. T., Kandel, B. M., Strien, N. v., Stone, J. R., Gee, J. C., and Avants, B. B. (2014). Large-scale evaluation of ANTs and FreeSurfer cortical thickness measurements. *NeuroImage*, 99:166–179.

[Verma et al., 2005] Verma, R., Mori, S., Shen, D., Yarowsky, P., Zhang, J., and Davatzikos, C. (2005). Spatiotemporal maturation patterns of murine brain quantified by diffusion tensor MRI and deformation-based morphometry. *Proceedings of the National Academy of Sciences*, 102(19):6978–6983.

[Viola and Jones, 2001] Viola, P. and Jones, M. (2001). Rapid object detection using a boosted cascade of simple features. In *CVPR (1)*, volume 1, pages 511–518.

[Wang et al., 2013a] Wang, H., Suh, J. W., Das, S. R., Pluta, J. B., Craige, C., and Yushkevich, P. A. (2013a). Multi-Atlas Segmentation with Joint Label Fusion. *IEEE Transactions on Pattern Analysis and Machine Intelligence*, 35(3):611–623.

[Wang et al., 2018] Wang, L., Li, G., Adeli, E., Liu, M., Wu, Z., Meng, Y., Lin, W., and Shen, D. (2018). Anatomy-guided joint tissue segmentation and topological correction for 6-month infant brain MRI with risk of autism. *Human Brain Mapping*, 39(6):2609–2623.

[Wang et al., 2014] Wang, L., Shi, F., Li, G., Gao, Y., Lin, W., Gilmore, J. H., and Shen, D. (2014). Segmentation of Neonatal Brain MR Images using Patch-Driven Level Sets. *NeuroImage*, 84:141–158.

[Wang et al., 2013b] Wang, Z., Donoghue, C., and Rueckert, D. (2013b). Patch-Based Segmentation without Registration: Application to Knee MRI. In Wu, G., Zhang, D., Shen, D., Yan, P., Suzuki, K., and Wang, F., editors, *Machine Learning in Medical Imaging*, Lecture Notes in Computer Science, pages 98–105.

[Warfield et al., 2004] Warfield, S. K., Zou, K. H., and Wells, W. M. (2004). Simultaneous truth and performance level estimation (STAPLE): An algorithm for the validation of image segmentation. *IEEE Transactions on Medical Imaging*, 23(7):903–921.

[Weisenfeld and Warfield, 2009] Weisenfeld, N. I. and Warfield, S. K. (2009). Automatic segmentation of newborn brain MRI. *NeuroImage*, 47(2):564–572.

[Whitfield et al., 1997] Whitfield, M. F., Grunau, R. V. E., and Holsti, L. (1997). Extremely premature (800 g) schoolchildren: multiple areas of hidden disability. *Archives of Disease in Childhood - Fetal and Neonatal Edition*, 77(2):F85–F90.

[Wright et al., 2015] Wright, R., Makropoulos, A., Kyriakopoulou, V., Patkee, P. A., Koch, L. M., Rutherford, M. A., Hajnal, J. V., Rueckert, D., and Aljabar, P. (2015). Construction of a fetal spatio-temporal cortical surface atlas from in utero MRI: Application of spectral surface matching. *NeuroImage*, 120:467–480.

[Xu et al., 2018] Xu, Y., Morel, B., Dahdouh, S., Puybareau, ., Virzì, A., Urien, H., Géraud, T., Adamsbaum, C., and Bloch, I. (2018). The challenge of cerebral magnetic resonance imaging in neonates: A new method using mathematical morphology for the segmentation of structures including diffuse excessive high signal intensities. *Medical Image Analysis*, 48:75–94.

[Xue et al., 2007] Xue, H., Srinivasan, L., Jiang, S., Rutherford, M., Edwards, A. D., Rueckert, D., and Hajnal, J. V. (2007). Automatic segmentation and reconstruction of the cortex from neonatal MRI. *NeuroImage*, 38(3):461–477.

[Yotter et al., 2011] Yotter, R. A., Dahnke, R., Thompson, P. M., and Gaser, C. (2011). Topological correction of brain surface meshes using spherical harmonics. *Human Brain Mapping*, 32(7):1109–1124.

[Yu et al., 2016] Yu, Q., Ouyang, A., Chalak, L., Jeon, T., Chia, J., Mishra, V., Sivarajan, M., Jackson, G., Rollins, N., Liu, S., and Huang, H. (2016). Structural development of human fetal and preterm brain cortical plate based on population-averaged templates. *Cerebral Cortex*, 26(11):4381–4391.

[Zhang et al., 2015] Zhang, W., Li, R., Deng, H., Wang, L., Lin, W., Ji, S., and Shen, D. (2015). Deep convolutional neural networks for multi-modality isointense infant brain image segmentation. *NeuroImage*, 108:214–224.

[Zhang et al., 2019] Zhang, Y., Yap, P.-T., Chen, G., Lin, W., Wang, L., and Shen, D. (2019). Super-Resolution Reconstruction of Neonatal Brain Magnetic Resonance Images via Residual Structured Sparse Representation. *Medical Image Analysis*.

UNIVERSITE BRETAGNE LOIRE / MATHSTIC

IMT Atlantique
Bretagne-Pays de la Loire
École Mines-Télécom

Titre : Segmentation automatique de la surface corticale dans des IRM cérébrales de nouveau-nés

Mots clés : Segmentation, IRM néonatale, Multi-atlas, Approche non-locale, Préservation topologique

Résumé : Des études cliniques sur les nouveau-nés prématurés montrent qu'une large proportion des grands prématurés (moins de 32 semaines d'aménorrhée) présentera des troubles cognitifs, moteurs ou comportementaux. Un objectif clinique est donc d'approfondir les études du développement cérébral et de détecter les anomalies chez les patients néonataux. Parmi les modalités d'imagerie, l'IRM peut fournir une information 3D morphologique, non-invasive, non-ionisante et avec une résolution spatiale de l'ordre du millimètre, propriétés qui sont bien adaptées à cette problématique. En outre, la segmentation de ces images permet de fournir des informations quantitatives de l'anatomie, comme le volume ou la forme. Il existe de nombreuses méthodes pour l'IRM chez l'adulte. Néanmoins, la plupart d'entre elles ne peuvent pas s'appliquer directement chez le nouveau-né, où la maturation des tissus cérébraux induit des modifications de contraste dans l'image (dues, par exemple, à la non-myélinisation de la substance blanche). De plus, des détériorations visuelles, telles que les effets de volume partiels, se produisent par l'effet conjugué de la résolution des images et de la finesse des structures (par exemple, le cortex). Cette thèse se focalise sur la segmentation de la surface corticale des nouveau-nés en utilisant des images IRM, avec une précision satisfaisante pour des applications subséquentes (comme la génération de maillages surfaciques). Dans cette thèse, nous nous sommes intéressés dans un premier temps aux approches par atlas ou multi-atlas. Cette famille de méthodes est connue pour son efficacité en termes de segmentation cérébrale grâce à des a priori spatiaux intégrés au modèle, qui permettent de guider la segmentation. Néanmoins, le cortex étant une structure très fine, des erreurs topologiques peuvent se produire. Afin de résoudre ce problème, une étape de correction topologique multiéchelle est mise en œuvre. Les résultats montrent le potentiel de ces deux types d'approches pour l'analyse des données considérées.

Title: Automatic segmentation of the cortical surface in neonatal brain MRI

Keywords: Segmentation, Neonatal MRI, Multi-atlas, Non-local approach, Topology preservation

Abstract: Clinical studies for preterm infants (less than 32 weeks of gestation) emphasize the fact that an important part of the very or extreme preterm infants will present cognitive, motor or behavioral disorders. The clinical aim is to improve brain development studies and be able to detect and predict abnormalities in neonatal subjects. Among the medical imaging, MRI can provide non-invasive non-ionizing morphological 3D images with a spatial resolution of the order of a millimeter, properties that are well adapted to this issue. In addition, the segmentation of these images provides quantitative anatomical information, such as volume or shape. There are many existing methods for adult MRI that successfully segment brain subparts. However, these methods cannot be directly applied to the newborn, where the maturation of brain tissue modifies the contrasts in the image (for example, the non-myelination of the white matter). Moreover, factors related to the resolution together with structural fineness, especially in the cortex, induce partial volume effects in tissue boundaries. This thesis focuses on the segmentation of the cortical surface in neonatal infants using MR images, with satisfactory accuracy for further applications (such as the generation of surface meshes). In this thesis, we first focused on the so-called atlas or multi-atlas approaches. This family of methods is known for its effectiveness in brain segmentation, thanks to spatial priors that can be embedded in the model for guiding the segmentation. However, since the neonatal cortex is very thin, there are often discontinuities or wrong connections. In order to tackle this issue, a topological correction step is proposed to fill gaps and separate erroneous connections. The results emphasize the potential of these two types of approaches for this purpose.